

A PROTON POLARIMETER FOR PION PHYSICS AT TRIUMF

By

Marcello Maurizio Pavan

B.A.Sc., University of British Columbia, 1986

**A THESIS SUBMITTED IN PARTIAL FULFILLMENT OF
THE REQUIREMENTS FOR THE DEGREE OF
MASTER OF APPLIED SCIENCE**

in

THE FACULTY OF GRADUATE STUDIES

Department of Physics

We accept this thesis as conforming
to the required standard

THE UNIVERSITY OF BRITISH COLUMBIA

APRIL 1990

© Marcello Maurizio Pavan, 1990

In presenting this thesis in partial fulfilment of the requirements for an advanced degree at the University of British Columbia, I agree that the Library shall make it freely available for reference and study. I further agree that permission for extensive copying of this thesis for scholarly purposes may be granted by the head of my department or by his or her representatives. It is understood that copying or publication of this thesis for financial gain shall not be allowed without my written permission.

Department of PHYSICS

The University of British Columbia
Vancouver, Canada

Date APRIL 23/1990

Abstract

A proton polarimeter employing multi-wire delay-line drift chambers (MWDDCs) has been built for ongoing pion absorption studies in the meson area at TRIUMF. A brief introduction of the theoretical basis of polarimeter and MWDDC operation is offered. An in-depth study of our own system is presented including an account of the data acquisition readout electronics and the procedures used for wire chamber position calibration. Detailed performance specifications of all aspects of our chamber are given, notably for the method used to solve the drift chamber left/right ambiguity. The chambers are found to operate reliably and efficiently with very good spatial resolution, $\sigma = \sim 200\mu\text{m}$. The systematic artificial asymmetry in the polarimeter is also studied. Finally, scattering-efficiency and figure-of-merit (\mathcal{F}) results are presented for 230 MeV protons scattering off a 7cm carbon analyzer in the three cases of $\phi + \pi$ and 2π azimuthal scattering acceptance symmetry, and full polarimeter acceptance. In particular, it is found that when employing the Bessel weighted-sums polarization extraction technique, imposition of $\phi + \pi$ azimuthal scattering symmetry results in only a small increase in measured statistical error compared to results obtainable from a full Fourier spectrum analysis with no applied acceptance symmetry.

Suggestions for improvements to established practices are offered throughout.

Table of Contents

| | |
|---|------------|
| Abstract | ii |
| List of Tables | vi |
| List of Figures | vii |
| Acknowledgements | ix |
| | |
| I Thesis Overview | 1 |
| | |
| II Polarizations, Analyzing Powers, and all that | 5 |
| II.1 Coordinate System Convention | 5 |
| II.2 Polarization and Analyzing Power | 7 |
| | |
| III Polarimeter Fundamentals | 9 |
| III.1 Design Considerations | 9 |
| III.1.1 Wire Chambers | 10 |
| III.1.2 Small-Angle Scattering Rejection | 12 |
| III.2 Extraction of Asymmetries from Scattering Data | 15 |
| III.2.1 Inclusive Analyzing Powers | 15 |
| III.2.2 Asymmetry Extraction and Acceptance Functions | 18 |
| III.2.3 Artificial Asymmetries | 20 |
| III.3 Scattering Efficiency and the Figure-of-Merit | 24 |
| | |
| IV Multi-Wire Delay-Line Drift Chambers | 30 |
| IV.1 Basic Drift Chamber Principles | 30 |

| | | |
|-----------|---|-----------|
| IV.1.1 | Pulse Formation | 30 |
| IV.1.2 | Drift Information | 32 |
| IV.1.3 | Left/Right Ambiguity | 34 |
| IV.1.4 | Fill Gases | 35 |
| IV.1.5 | Chamber Operating Voltage | 36 |
| IV.1.6 | Chamber Aging and Cleaning | 37 |
| IV.2 | Delay-Line Chambers and Position Extraction | 38 |
| IV.2.1 | Chamber Geometry | 39 |
| IV.2.2 | Fundamental Chamber Signals | 40 |
| IV.2.3 | Position Determination | 41 |
| IV.2.4 | CHECKSUM and Chamber Efficiency | 44 |
| V | The E331 Polarimeter System | 49 |
| V.1 | Construction Details | 49 |
| V.1.1 | System Layout and Cart Construction | 49 |
| V.1.2 | Drift Chamber Construction | 55 |
| V.2 | Data Acquisition | 61 |
| V.2.1 | Event Trigger | 62 |
| V.2.2 | Wire Chamber Electronics | 65 |
| V.2.3 | Small-Angle Scattering Event Preprocessing | 71 |
| V.2.4 | Online Diagnostics | 72 |
| VI | Polarimeter Calibration | 76 |
| VI.1 | Particle Identification | 76 |
| VI.2 | Wire Chamber Position Calibration | 77 |
| VI.2.1 | SUMTIME and drift distance | 78 |
| VI.2.2 | CHECKSUMs | 79 |
| VI.2.3 | COMBs | 79 |

| | |
|---|------------|
| VI.2.4 Resolving Left/Right Ambiguity | 80 |
| VI.3 Chamber Alignment | 83 |
| VII Polarimeter Performance: Results and Conclusions | 95 |
| VII.1 Detection Efficiency and Resolution | 95 |
| VII.1.1 Chamber Efficiencies | 95 |
| VII.1.2 ODD-EVEN Resolution | 100 |
| VII.1.3 Trajectory Resolution | 101 |
| VII.1.4 J11 Small-Angle Rejection Efficiency | 102 |
| VII.2 Artificial Asymmetry Results | 103 |
| VII.2.1 Asymmetry Corrections from Angular Displacements | 105 |
| VII.3 Scattering Efficiency and Figure-of-Merit for 200 MeV Protons | 106 |
| VII.4 Conclusions and Recommendations | 109 |
| Bibliography | 118 |
| A Schematic Diagram of Anode Signal Preamplifier | 121 |

List of Tables

- I Summary of some important wire chamber characteristics 59
- II Global scattering efficiency and figure-of-merit results for 200 MeV
 protons 108

List of Figures

| | | |
|----|---|----|
| 1 | Photograph of Polarimeter and Second Arm | 2 |
| 2 | Coordinate System Convention | 6 |
| 3 | Inclusive, elastic, and quasi-elastic proton-carbon analyzing powers around 800 Mev. | 16 |
| 4 | Comparison of the McNaughton and Aprile-Giboni inclusive p-C analyzing power fits at 215 MeV | 17 |
| 5 | Azimuthal distribution for a particular carbon theta scattering bin | 27 |
| 6 | Normalized standard deviations for three asymmetry extraction techniques as a function of asymmetry | 27 |
| 7 | The 'cone', ' $\phi + \pi$ ', and full acceptance tests | 28 |
| 8 | Angular distribution for the three different acceptance requirements | 28 |
| 9 | Angle-averaged inclusive p-C analyzing power versus proton kinetic energy | 29 |
| 10 | A typical drift chamber unit cell geometry | 31 |
| 11 | Typical SUMTIME distribution | 46 |
| 12 | Typical wire chamber COMB distribution | 46 |
| 13 | Typical cathode ADC spectrum | 47 |
| 14 | Typical ODD - EVEN distribution | 47 |
| 15 | Typical CHECKSUM distribution | 48 |
| 16 | Polarimeter cart side and top views with dimensions | 50 |
| 17 | Second arm cart top and side views with dimensions | 51 |
| 18 | Wire chamber schematic diagrams showing external dimensions | 57 |
| 19 | Labelling scheme for the wire chamber signals | 57 |
| 20 | Schematic diagram of our delay-line drift chamber wire plane | 58 |
| 21 | ODD-EVEN versus COMB plot ('Henderson Effect') | 60 |
| 22 | Schematic diagram of event trigger logic | 63 |
| 23 | Effect of START timing jitter on DRIFT timing | 64 |
| 24 | Schematic Diagram of Data Acquisition Electronics | 66 |
| 25 | Small chamber COMB and CHECKSUM for different CFD delays | 69 |
| 26 | Large chamber COMB and CHECKSUM for different CFD delays | 69 |
| 27 | COMB and CHECKSUM distributions for improper and proper CFD walk adjustments | 70 |

| | | |
|----|---|-----|
| 28 | ODD-EVEN versus SUMTIME showing pronounced dip due to signal truncation | 74 |
| 29 | Circular small-angle rejection implemented with the J11 preprocessor | 75 |
| 30 | Scintillator ADC spectrum showing proton peak | 85 |
| 31 | Position jitter correction of second arm scintillator TOF | 86 |
| 32 | TOF versus S3B ADC plots with/without scintillator position correction | 86 |
| 33 | Differences in SUMTIME timing due to different particle velocities . | 87 |
| 34 | Calibrated SUMTIME distribution | 88 |
| 35 | Drift-distance versus SUMTIME relationship | 88 |
| 36 | ODDIME versus SUMTIME plot used to calibrate a CHECKSUM | 89 |
| 37 | Typical calibrated CHECKSUM distribution showing good event cut | 89 |
| 38 | Discrete COMB spectrum overlap with continuous COMB spectrum | 90 |
| 39 | Linear fit of COMB peak positions to DIFFTIME | 90 |
| 40 | Illustration of an ODD-EVEN calibration method | 91 |
| 41 | Illustration of the three interchamber ODD/EVEN phase relationships | 92 |
| 42 | Plots used to align the chamber coordinates | 93 |
| 43 | Example of resolution plot used check wire chamber alignment . . . | 94 |
| 44 | CHECKSUM efficiency as a function of chamber high voltage and beam rate | 96 |
| 45 | ODD/EVEN resolution for various chamber voltages | 98 |
| 46 | ODD/EVEN resolution at 2150 volts for a few attenuation settings . | 99 |
| 47 | Plots comparing extents of 2249A and 2249W ADC overflows at 2150 volts | 112 |
| 48 | Resolution plot for a small wire chamber | 112 |
| 49 | Sideways asymmetry and polarization extracted with Fourier fitting | 113 |
| 50 | Sideways asymmetry and polarization extracted with the weighted-sums technique | 114 |
| 51 | Projected angular displacements and logarithmic derivative of cross-section | 115 |
| 52 | Differential and integral figure-of-merit angular distributions for all three acceptance requirements | 116 |
| 53 | Differential and integral scattering efficiency angular distributions for all three acceptance requirements | 117 |

Acknowledgements

Behold, I tell you a mystery;

we shall not all sleep,

but we shall all be changed.

Not another word should be written until I most gratefully acknowledge the support of my supervisor, Garth Jones, whose boundless good will and wisdom has guided me throughout my work. My deepest appreciation for his help cannot be overstated. Of course, I would also like to thank my colleagues, Andrew Feltham, Peter Weber, and Peter Trelle (wherever he is), for all the help and encouragement they have given me. In particular, Andrew's help in the last days of writing this tome is greatly appreciated. Then there are the legions of soul-mates and VAX-mates who have kept me company in 222 and on the cluster at night: John, Chris, Fraser, Reena, Mark, Vesna, Raul, Steve, Qiang, Niall, Jean, Jim, Grant, and of course, *mio amico*, Rinaldo. Thanx for making it all a little more bearable. Anyone who can't have fun with this bunch around is either dead, or a theorist. (No offense, Jim.) I would also like to thank Jean Holt for her help with the diagrams.

Finally, I would like to convey my deepest thanks to Mama and Papa, Colleen, and Juan Valdez, without whom none of this would have been possible.

Chapter I

Thesis Overview

Some of the most stringent tests for modern theories in nuclear physics come from the comparisons of experimentally-determined spin-dependent quantities with the corresponding theoretical predictions. Advances in polarized beam and polarized target technologies have allowed an extensive number of spin-related measurements to be made in recent years. Many of these measurements require that the polarization of one or more final state particles be determined, frequently protons. Carbon analyzer polarimeters provide a simple and economic means to determine proton polarizations ($P(E, \theta)$) for intermediate kinetic energies ranging between 0.1 and 1.2 GeV. Measurement of the azimuthal asymmetry of protons scattering off a carbon analyzer enables one to determine the proton polarizations using previously determined analyzing powers ($A_c(E, \theta)$) for the inclusive \vec{p} -C reaction (for example, see McNaughton [1]). This carbon scattering technique for determining proton polarizations has proven itself to be effective at a number of ‘meson factories’ worldwide.

Our pion absorption group at TRIUMF has constructed a proton polarimeter for use primarily in ongoing nuclear pion absorption studies in the meson hall area, the first time a polarimeter of this type has been used in a pion channel. The polarimeter is similar to earlier designs [2,3,4] consisting of two sets



Figure 1: The E331 Polarimeter cart and second tracking arm.

of three x-y particle tracking chambers on either side of a variable-thickness carbon analyzer stack (see figure 1). Two scintillator counter assemblies before and after the second group of chambers define candidate events. A second arm with three chambers and event defining scintillators was also constructed for use in those experiments which require a second final state charged particle to be tracked. Our system resembles the TRIUMF Medium Resolution Spectrometer Focal Plane Polarimeter (MRS FPP) [4] and the LAMPF JANUS polarimeter [3] in that both these systems utilize multi-wire delay-line drift chambers (MWDDC) rather than the amplifier-per-wire multi-wire proportional chambers (MWPC) used in some other polarimeter systems [2,5,6]. The various techniques used

among these systems for particle detection and analysis will be outlined throughout chapters II and III.

To date our polarimeter has successfully operated in two different experiments, both of which ran on the M11 high-intensity pion channel at TRIUMF. The polarimeter was originally constructed for Experiment 331 [7], an experiment designed to measure the spin transfer parameters K_{LS} , K_{SS} , and K_{NN} in the fundamental pion absorption reaction $\pi^+ \vec{d} \rightarrow \vec{p} p$. Forward protons emanating from the TRIUMF polarized deuteron target [8] were analyzed by the polarimeter while the backward protons were detected in coincidence using our second wire chamber tracking arm. The kinetic energies for the protons incident on the polarimeter spanned the range 130 MeV to 290 MeV (for a more complete description of Expt. 331, refer to [9,10]). The other experiment employing the polarimeter was also a pion absorption measurement. Experiment 445 [11] was designed to determine the angular dependence of the polarization of a final state proton in each of the $\pi^+ d \rightarrow \vec{p} p$ and $\pi^+ {}^3\text{He} \rightarrow \vec{p} p p$ reactions for a variety of incident pion energies, where the polarimeter analyzed protons with kinetic energies ranging from 130 MeV to 240 MeV.

Clearly, with the polarimeter being the key ingredient in these experiments, a rigorous analysis of the experimental results could not be undertaken until the operation of the polarimeter was well understood and its systematic effects identified and evaluated. Consequently, the aim of this thesis is to provide a comprehensive study of the operation of our polarimeter; in effect this is the "E331 Polarimeter Users' Handbook". Chapters II, III, and IV outline the major concepts of polarimeter operation like scattering asymmetries, proton-carbon analyzing powers, and the use of multi-wire tracking chambers. These chapters provide a brief 'polarimetry' reference guide, and an introduction all the definitions and conventions used in the subsequent chapters. Chapter V describes

the E331 polarimeter system in detail, covering cart and wire chamber construction, as well as data acquisition nucleonics, logic, and online diagnostic procedures. The system presented here has evolved over the period January 1987 to October 1988 as a result of our data acquisition experience.

This study focuses on the multi-wire delay-line drift chambers used in our polarimeter, with special emphasis on the techniques used to extract and analyze the wire chamber position information. Chapter VI will present step-by-step the wire chamber calibration procedure adopted by our group. In particular, techniques employed for resolving the inherent left/right ambiguity in drift chamber trajectory determination are discussed in some detail.

Chapter VII presents some polarimeter and wire chamber performance results. Wire chamber efficiencies are presented as functions of chamber high voltage and incident beam rate, and the ability of our system used to resolve the left/right ambiguity under various operating conditions is investigated. Performance benchmarks like systematic artificial asymmetries and the polarimeter 'figure-of-merit' (\mathcal{F} defined in Section III.3) are given for a particular test run using 235 MeV protons incident on a 7cm analyzer. (Figures-of-merit permit experimenters to accurately estimate scattering rates when using this type of polarimeter system). Also, systematic effects which could result in false scattering asymmetries are explored here and throughout the thesis and their relative importances analyzed. Finally, a number of recommendations relating to improvements on established practises are offered to future users of such systems.

Chapter II

Polarizations, Analyzing Powers, and all that

II.1 COORDINATE SYSTEM CONVENTION

The ‘Madison Convention’ [12] has come to be the accepted description for the labelling of polarization-related quantities and the coordinate systems in which they are defined. Consequently, this will be the scheme adopted here. Let \hat{k}_i and \hat{k}_f denote the unit vectors along the direction of momentum for the particles entering and leaving a nuclear reaction, respectively. The positive y-axis is defined parallel to the normal to the scattering plane defined by \hat{k}_i and \hat{k}_s :

$$\hat{y} = \hat{n} = \frac{\hat{k}_i \times \hat{k}_s}{|\hat{k}_i \times \hat{k}_s|} \quad (1)$$

Incident particle polarizations are defined with respect to some suitable frame $(\hat{i}, \hat{j}, \hat{k})$

$$P_p = P_x \cdot \hat{i} + P_y \cdot \hat{j} + P_z \cdot \hat{k}$$

which can be the lab frame, or the coordinate system defined in terms of the scattering plane of a prior reaction from which the incident particles emerged. As examples, a primary or secondary proton beam from an accelerator incident on a polarimeter will be referred to the lab frame, whereas protons from a reaction like $\pi d \rightarrow pp$ will be referred to the coordinate system defined by this reaction’s

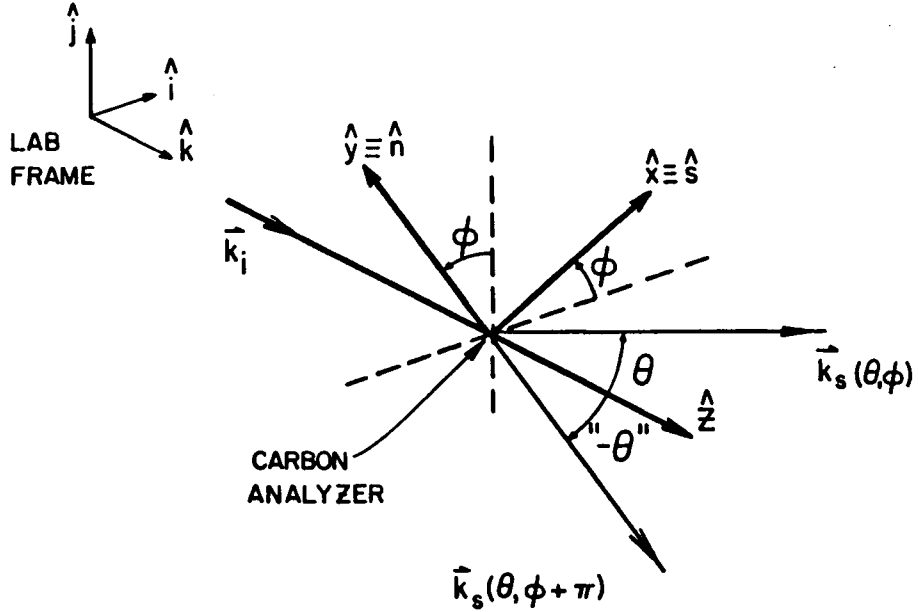


Figure 2: The coordinate system conventions adopted here for describing the scattering of protons off a polarimeter carbon analyzer. These definitions follow those recommended in the Madison Convention.

scattering plane, using the convention discussed here. Quantities like analyzing power (which describe the effects on cross-sections of initial beam polarizations) or *incident* proton polarizations are referred to the right-handed coordinate frame defined by \hat{y} and $\hat{z} = \hat{k}_i$. With this reference in hand, one can then construct the polar and azimuthal scattering angles in the carbon, θ and ϕ :

$$\sin(\theta) = |\hat{k}_i \times \hat{k}_s| \quad (2)$$

$$\cos(\phi) = \hat{j} \cdot \hat{n} \quad (3)$$

$$\sin(\phi) = -\hat{i} \cdot \hat{n} \quad (4)$$

See figure 2 for a schematic representation of the above definitions.

II.2 POLARIZATION and ANALYZING POWER

To understand how the polarimeter can determine the polarization of a particle, first recall that protons are strongly interacting particles and therefore obey parity invariance. In the case of spin- $\frac{1}{2}$ particles (like protons) scattering off spin-0 targets (like carbon), the most general form of the differential cross-section that satisfies parity, linear, and rotational invariance can be written [13]:

$$\sigma(\theta, \phi) = \sigma_0(\theta) + \sigma_1(\theta)(\hat{n} \cdot \vec{P}_i) \quad (5)$$

where \vec{P}_i is the incident proton polarization, $\sigma_0(\theta) = \sigma_{\uparrow} + \sigma_{\downarrow}$ is the **unpolarized** proton-carbon cross-section and $\sigma_1(\theta) = \sigma_{\uparrow} - \sigma_{\downarrow}$ is the difference in **pure polarized** ‘up’ and pure polarized ‘down’ cross-sections (with respect to \hat{n}) [7].

The **scattering asymmetry** is defined as

$$\epsilon(\theta) \equiv \frac{\sigma(\theta) - \sigma(-\theta)}{\sigma(\theta) + \sigma(-\theta)} \quad (6)$$

which is the normalized difference in the number of scatterings to the ‘left’ ,(+ θ), and to the ‘right’ ,(- θ), of the incident beam *in the target scattering plane* (see figure 2)¹. By observing that $\sigma_0(\theta) = \sigma_0(-\theta)$ and that the scattering normals in the ‘left’ and ‘right’ cases are opposite in direction, one derives the expression which directly relates the incident proton polarization to the scattering asymmetry:

$$\epsilon(\theta, \phi) = \frac{\sigma_1(\theta)}{\sigma_0(\theta)}(\hat{n} \cdot \vec{P}) \quad (7)$$

$$= \mathcal{A}(\theta)(\hat{n} \cdot \vec{P}) \quad (8)$$

The quantity $\mathcal{A}(\theta)$ is called the **analyzing power**. It describes the dependence of the angular distribution of a reaction on the initial beam polarization. The ϕ

¹For purposes of explanation, here the azimuthal angle ϕ is restricted to $0 \leq \phi < \pi$ and the polar angle θ is allowed to take negative values. However, the Madison convention as defined in equations 2,3, and 4 restricts $\theta \geq 0$ and allows $\pi > \phi \geq -\pi$

dependence on ϵ comes from the dot product of the scattering normal with the polarization vector, and from this one notes that only the polarization component *normal* to the scattering plane affects the cross-section and therefore the asymmetry. *i.e.* with a known $\mathcal{A}(\theta)$ for the reaction in question, measuring the left-right asymmetry in a scattering plane with normal \hat{e} determines the polarization component $P_{\hat{e}}$. (To measure the longitudinal polarization with such an apparatus, the polarization vector of the incident particle beam must first be precessed 90° from the beam direction using a magnetic field). The analyzing power $\mathcal{A}(\theta)$ can be measured by preparing a beam of known polarization and then measuring the resulting scattering asymmetries, or by taking the difference of the cross-sections at a fixed angle (θ, ϕ) for beams of opposite polarization. (for more detailed information, see [13]).

One can derive the expression for the differential cross-section in the form usually found in the literature by using equations 2, 3, 4, and 8 :

$$\sigma(\theta, \phi) = \sigma_0(\theta)[1 + \mathcal{A}(\theta)(\hat{n} \cdot \vec{P})] \quad (9)$$

$$= \sigma_0(\theta)[1 + \epsilon_N(\theta) \cos(\phi) + \epsilon_S(\theta) \sin(\phi)] \quad (10)$$

where $\epsilon_N \equiv P_y \mathcal{A}$ and $\epsilon_S \equiv -P_x \mathcal{A}$ are called the **left/right** and **up/down** asymmetries used to calculate the **normal** and **sideways** ($\parallel \hat{j}$) components of the initial beam polarization, respectively. Note that the scattering asymmetries have a sinusoidal dependence on ϕ , so that normal and sideways components can be determined from any azimuthal angle, with maximum asymmetries occurring at $\phi = 0^\circ$ and $\phi = 90^\circ$ respectively. This expression is the starting point for the various analysis techniques used to extract the asymmetries from measured particle angular distributions in θ and ϕ . Some of these techniques are briefly outlined in the following chapter.

Chapter III

Polarimeter Fundamentals

Some background information on polarimeter design, scattering efficiency principles, and polarization extraction techniques are outlined in this chapter. This will serve to introduce the basic principles and techniques involved in the use of polarimeters to those unfamiliar with their operation. The topics are treated in some length; however, since the aim of this thesis is to present mainly the operation of the E331 polarimeter system, more detailed information on these subjects can be obtained from the many excellent papers on these subjects (see for example [14,15,19]). References to these papers will be indicated where appropriate throughout the chapter.

III.1 DESIGN CONSIDERATIONS

Besides our own, there are a number of intermediate energy proton polarimeter systems in use around the world based on inclusive proton-carbon scattering. These include JANUS at LAMPF [3], POMME at Saclay [15], the Geneva groups' unnamed system at PSI [2], as well as the focal plane polarimeters in the MRS at TRIUMF [4] and the HRS at LAMPF [16]. These systems operate for incident proton kinetic energies varying from a low of 95 MeV at PSI to a high of 1.2 GeV at Saclay. Consequently the operational principles and techniques have become well established and are thoroughly documented in the literature. For example,

the inclusive proton-carbon analyzing powers have been measured and parameterized throughout this energy range and are reported in McNaughton, *et al.* [1] and Bonin, *et al.* [15].

All these polarimeters consist basically of a carbon analyzer situated between two arrays of trajectory-defining wire chambers. Carbon is the analyzer of choice for protons since it combines relatively high analyzing powers and cross-sections with moderately-low multiple scattering, high chemical purity and stability, easy handling, wide availability and low cost. Thin scintillators before and after the carbon define event coincidences, and in most cases provide energy-loss ($\frac{dE}{dX}$) and time-of-flight (TOF) information for particle identification. A rigid, movable carriage or support secures these elements into a fixed, or variable, yet reproducible geometry.

III.1.1 Wire Chambers

The wire chambers are obviously the most critical components of any polarimeter system. They are organized into tracking groups (or telescopes) of 2-4 wire planes each for x and y on either side of the carbon in order to determine the trajectories of the protons entering and leaving the carbon analyzer, and thus the scattering angles. The redundancy provided by the use of three (any 2/3) or four (2/4) chambers greatly increases particle tracking efficiency above that resulting from the use of only two chambers.¹ On the other hand, by using all three (or four) chambers, a trajectory can be fitted to the coordinates thus reducing the directional uncertainty over those trajectories calculated with two chamber coordinates as segment endpoints. Individual chamber spatial resolution requirements depend on the desired angular resolution in each tracking group,

¹For example, assuming single chamber efficiencies of 90%, the probability of both of two chambers firing is 81%; whereas use of any two out of a three chamber group raises the tracking efficiency to $(.9)^3 + 3(.1)(.9)^2 = 97.2\%$.

which also depend on the interchamber distances. Usually, tracking groups yield angular resolutions of $\ll 1^\circ$ for precise angular binning of scattered events.

Other attributes necessary for all polarimeter wire chambers include stable, reliable operation with a high efficiency which is uniform across the active area of the chamber. These characteristics follow from the need for accurate, unbiased measurements of the scattering angles to prevent erroneous systematic asymmetries from being introduced into the data. Systematic effects in either chamber group causing errors in trajectory determination (like shifts in measured positions) can generate these false, or **parasitic**, scattering asymmetries. The performance of the group tracking the protons scattered by the carbon (the 'post-carbon' group) is more critical than the 'pre-carbon' group since regional inefficiencies in the post-carbon chambers and scintillators could cause false asymmetries to be measured. Similar inefficiencies in the pre-carbon chambers do not introduce parasitic asymmetries but merely alter the incident acceptance of the polarimeter. The chambers tracking the scattered protons are usually larger than the incident chambers since they must be able to accept protons scattering by as much as 25° from the carbon with respect to the incident beam. Events passing at large angles through the wire chambers are often not detected as efficiently as events incident perpendicularly, so particular care has to be taken to account for these and other inefficiencies in the asymmetry analyses.

All of the polarimeter systems referred to earlier employ either multi-wire proportional chambers (MWPC, with wire-by-wire readout) or multi-wire delay-line drift chambers (MWDDC or DDC, with delay-line readout) for their particle tracking. The two chamber types differ quite markedly in their respective strengths and weaknesses. MWPCs have typically 2 mm wire spacing resulting in $\sim \pm 0.68$ mm resolution; whereas the DDCs can achieve resolutions around ± 0.20 mm with 8 mm wire spacings. Therefore the DDCs can be mounted closer together

than the MWPCs for a given angular resolution, thus saving space and increasing solid angle. The MWPCs, however, operate as ‘amplifier-per-wire’ systems which increases their rate capability and offers the ability to identify multiple tracks. DDCs have only two preamplifiers-per-plane at either end of a delay-line, thereby precluding multi-track identification as well as high rate operation (due to greatly increased dead-times) while offering greater electronic simplicity and hence reduced cost compared to the MWPC preamplifier system. Modern versions of both types offer good stability and efficiency across the active detection area, but again there is a tradeoff between dealing with the small differences in each of the many preamplifiers associated with a MWPC, or accounting for the small non-linearities which inevitably arise from the use of delay-lines.

Of all the above attributes, the requisite rate capability stands as the limiting factor when choosing polarimeter wire chambers. As examples, proton-carbon analyzing power studies over a large angular range need proportional chambers to handle the high particle intensities associated with primary proton beams. On the other hand, polarization analysis studies involving scattered (or double-scattered) beam intensities which are relatively low, generally utilize drift chambers due to their efficiency and cost effectiveness since they can cover a larger solid angle than MWPCs for a given chamber size and spatial resolution. Chapter IV discusses wire chamber operation in more detail, with emphasis on delay-line drift chambers of the type used in our polarimeter system.

III.1.2 Small-Angle Scattering Rejection

As in all scattering processes involving charged particles, coulomb multiple scattering dominates the p-C inclusive cross-section at small angles.

Unfortunately, coulomb scattering is not spin-dependent, so it cannot be used as a polarization-analyzing reaction. Consequently polarizations inferred from

scattering angles in the coulomb-dominated region will appear lower than their true value if one uses analyzing powers which have not been corrected for coulomb effects². Small-angle coulomb dominance coupled with the fact that analyzing powers associated with nuclear scattering vanish at zero angle (making these small-angle scatters of limited use for determining polarizations), clearly indicate that these data should be rejected before attempting to extract polarizations. One can reject this data with a simple software small-angle cut in the offline data analysis, but with over 90% of the incident protons suffering these small-angle coulomb (or nuclear) scatters, data tapes will be needlessly filled up with useless information with consequent increased electronic deadtime. For this reason all polarimeter systems have some form of online small-angle rejection to improve the 'useful' event fraction written to tape.

Historically, online small-angle scattering rejection has proceeded via one of numerous hardware techniques, but recent advances in real-time computer hardware have enabled a few systems to implement software preprocessing schemes. The software and the hardware approaches both rely on the positional information provided by the wire chambers in 'real-time'. Usually the chambers are uncalibrated, or only partially calibrated, during a run,³ so the scattering angles reconstructed online are of limited accuracy. But since the calculations can be improved offline to ensure a symmetrical small-angle cut (necessary to avoid introduction of artificial asymmetries as will be discussed in Section III.2.3), a coarse angle determination suffices for small-angle rejection purposes. Hardware systems encode these chamber signals into bit patterns or proportional analog signals which can then be manipulated by fast-decision logic circuits to determine

²Aprile-Giboni, *et al.*[2], published a p-C inclusive analyzing power parameterization which includes a damping term for small-angle scattering; whereas McNaughton, *et al.* [1] have published a similar parameterization without said correction. See Section III.2.1.

³Fully calibrated wire chambers employ many constants in the position determinations which normally require too much computer effort for inclusion into the real-time calculations.

scattering angles. Events are accepted or rejected with fast veto pulses. Software systems replace the fast-decision logic with computer preprocessors which calculate the scattering angles in real-time programs, and apply rejection decisions based on software instead of hardware logic. To be safe, both these schemes normally accept those events where a decision can not be reached so that they can be rechecked offline. (Reasons for such include multiple hits and chamber inefficiencies). Specific examples of both these approaches can be found in Häusser, *et al.* [4], Ransome, *et al.* [3], Bonin, *et al.* [15], and Besset, *et al.* [17].

When designing any complex system, one inevitably confronts a hardware versus software tradeoff and the case presented above is no exception. Of the two, hardware rejection offers the fastest decision making. Experiments where other preprocessing decisions must be made online and where computer dead-time must be minimized will benefit from the decision speed advantage of hardware over software rejection. On the other hand, logic circuits cannot be manipulated easily so that changing experimental conditions cannot usually be accommodated quickly in hardware, but simple program code and/or parameter changes can be easily implemented in the software approaches. Furthermore, if increased computer dead-time is not a problem, much more complex preprocessing demands can be implemented in software. Software decisions require approximately 100 μsec [15] to 1100 μsec [4], depending on the complexity, whereas hardware decisions can be made in $\sim 3 \mu\text{sec}$ [2,18]. These times should be compared to the typically few *milliseconds* necessary for the acquisition computers to read and write out the data to tape.

The software approach adopted by our group, employing the CES Starburst J11 CAMAC microcomputer as the front-end preprocessor, will be discussed in Section V.2.3.

III.2 EXTRACTION of ASYMMETRIES from SCATTERING DATA

This section offers a brief summary of some of the analysis techniques used to extract asymmetries from the scattering distributions. Since a detailed discussion lies outside the scope of this thesis, the reader should consult Besset, *et al.* [19], Waters, *et al.* [6], and the theses of Ransome [14] and Feltham [10], for more specific details on the analysis procedures.

In practice, the theoretical expression describing the distribution of analyzer-scattered protons, equation 10, must be modified to reflect the non-ideal detection efficiency of the polarimeter system and the contributions from the many possible p-carbon reactions occurring in the analyzer. The *observed* angular distribution $I(\theta, \phi)$ can then be written as

$$I(\theta, \phi) = N\sigma_0^{inc}(\theta)[1 + \epsilon_N \cos(\phi) + \epsilon_S \sin(\phi)] \cdot D(\theta, \phi) \quad (11)$$

where σ_0^{inc} is the **inclusive cross-section**, N is the overall normalization, and $D(\theta, \phi)$ is the **detection efficiency**, or **acceptance**. Inclusive cross-sections and analyzing powers combine contributions from all the reactions ($p + C \rightarrow \text{charged} - \text{particle} + X$) which can occur in the analyzer. The detection efficiency represents both the geometrical acceptance and the spatially-varying efficiency of the post-carbon tracking group.

III.2.1 Inclusive Analyzing Powers

For practical reasons only inclusive analyzing powers are considered for use with polarimeters. Firstly, it would be difficult to equip the polarimeters to distinguish between the dominant elastic and quasi-elastic (p-N) reactions occurring in the analyzer. Also, the purely elastic analyzing power typically shows wide variations over narrow angular ranges which are 'smoothed out' by the quasi-elastic

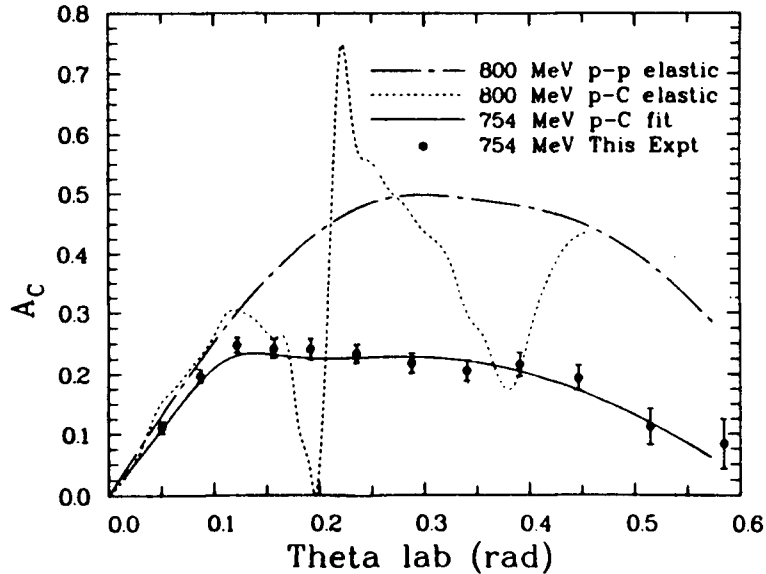


Figure 3: Comparison of the elastic and quasi-elastic proton-carbon analyzing power at $T_p=800$ MeV measured at LAMPF with the inclusive result at 754 MeV. (From Ransome, *et al.* [20], page 318)

analyzing power, thus making the determination of the carbon scattering angles much less critical. Figure 3 compares inclusive, elastic, and quasi-elastic analyzing powers measured at LAMPF [20] and clearly shows the smoothing effect of the quasi-elastic contribution.

Even though elastic and quasi-elastic scattering dominate the other inelastic and production reactions that occur in the analyzer (which have been shown [18] to reduce somewhat the overall effective analyzing power); these other processes contribute non-negligibly and can be strong functions of energy. This implies that the inclusive analyzing power at a given energy varies with carbon thickness due to the proton energy loss. Aprile-Giboni, *et al.* [2] show that the differences are only significant below ~ 250 MeV. Also, for the highest possible accuracies, each polarimeter should have its own analyzing powers measured since experimental conditions (like energy thresholds, which limit allowable inelastic events) vary from system to system. For example, figure 4 shows a small discrepancy between

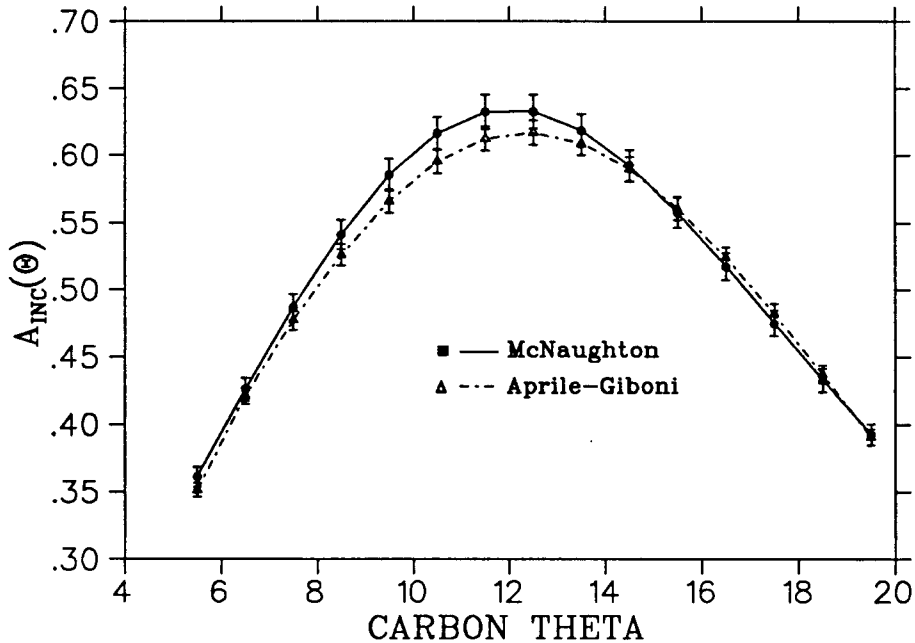


Figure 4: Discrepancy between the 215 MeV inclusive analyzing powers of McNaughton, *et al.* [1] and Aprile-Giboni, *et al.* [2] obtained from their global energy fits. Error bars represent their quoted uncertainties of 2% and 1.5%, respectively.

the global energy-dependent fits to the analyzing powers of McNaughton, *et al.*[1] and Aprile-Giboni, *et al.* [2] at $T_p^{center}=215$ MeV, corresponding to the proton kinetic energy at the center of the analyzer.⁴ For the most part, such variations appear to be small as there has been good agreement between the analyzing powers measured at different labs [1,2,15] over a broad energy range. As long as the carbon thicknesses used at a particular energy do not differ greatly, the ‘average’ energies (taken at the center of the analyzer) quoted with the compilations are good approximations, so one can expect that these inclusive analyzing powers can be used with different systems with reasonable accuracy.

⁴We (E331) have chosen to employ McNaughton values in our analyses since these (more recent) results represent a fit to the ‘world’ data; whereas the (older) Aprile-Giboni fits do not.

III.2.2 Asymmetry Extraction and Acceptance Functions

The choice of the particular asymmetry extraction technique to use depends intimately on the way in which the acceptance function is handled. The most straightforward technique requires the determination of the acceptance function $D(\theta, \phi)$ directly as a Fourier decomposition in ϕ [6]:

$$D(\theta, \phi) = a_0 + \sum_n [a_n(\theta) \cos(n\phi) + b_n(\theta) \sin(n\phi)] \quad (12)$$

This function can be determined experimentally by fitting the coefficients $a(\theta), b(\theta)$ to the scattering distribution

$$I_+(\theta, \phi) + I_-(\theta, \phi) = 2 \cdot N \cdot \sigma_0^{inc}(\theta) \cdot D(\theta, \phi) \quad (13)$$

Here the unpolarized cross-section is known, and $I_{\pm}(\theta, \phi)$ are the measured intensity distributions arising from polarized ‘up’ and ‘down’ initial beams, respectively. This ‘acceptance map’ combines both the geometric acceptance and the wire chamber efficiencies of the polarimeter. With the efficiency function determined, asymmetry extraction follows in this straightforward, ‘brute-force’, technique by fitting the asymmetry coefficients $\epsilon_N(\theta)$ and $\epsilon_S(\theta)$ to the observed distribution in ϕ for each θ bin (equation 11) using χ^2 or maximum-likelihood minimization. (An example is illustrated in figure 5 .)

One can improve the above procedure by applying a symmetry constraint on the acceptance function. Normally, since wire chambers have rectangular construction, the geometric acceptance component of $D(\theta, \phi)$ will introduce many terms to the Fourier series, thus increasing the number of coefficients necessary to give a good fit and possibly compromising the accurate determination of asymmetries. The geometric acceptance component can be greatly simplified by insisting on a full 2π azimuthal acceptance. *i.e.* a scattered ray is accepted if and only if all other rays rotated by an arbitrary angle $\Delta\phi, (0 \leq \Delta\phi < 2\pi)$ satisfy some

geometric acceptance requirement. For example, one might require the projections of all rotated rays to fall within some prescribed region on the back wire chamber [10] (see figure 7). This can be accomplished rather simply as a software cut and it essentially defines a geometric acceptance equal to unity. The remaining detection efficiency will then represent just the spatially-varying wire chamber efficiency, which can be expected to be near unity for all (θ, ϕ) and thus can be expected to be fit well by only a few terms in its Fourier series. Asymmetry extraction follows as before through minimization techniques applied to the observed scattering distribution $I(\theta, \phi)$. A very similar procedure was carried out by the BASQUE and POMME collaborations [6,15] for determining analyzing powers.

Besset, *et al.* describe in [19] an alternative to the methods outlined above that removes the need for both polarimeter acceptance studies (Monte Carlo or otherwise) and χ^2 fitting procedures, while improving the overall acceptance. As noted in that paper, the above ‘brute-force’ procedure can become “technically useless if extensive sets of asymmetries have to be estimated simultaneously”. The method is based on taking the Fourier sine and cosine transforms of $I(\theta, \phi)$ (equation 11) over the azimuthal angle ϕ and then estimating the resulting integrals by sums. If the detection efficiency has a full 2π azimuthal symmetry, only three sums (neither of which include $D(\theta, \phi)$) are required to estimate the asymmetries at each angle θ . However, this condition can be relaxed to the less restrictive symmetry property $D(\theta, \phi) = D(\theta, \phi + \pi)$ and still not have the acceptance appear in the sums. These transforms have additional cross-terms, but it is shown in [19] that the resulting equations can be expressed in a simple matrix form and the asymmetries estimated with straightforward matrix inversion and multiplication. In this case five sums need to be calculated for every θ bin. The technique can also be directly generalized to enable extraction of polarizations by forming weighted sums over all ϕ and θ bins where the analyzing powers $\mathcal{A}(\theta)$

serve as the ‘weights’.

These polarization estimators for this so-called **weighted-sums** technique claimed to be [19] unbiased, robust, and almost as efficient as the theoretical maximum likelihood estimators (see figure 6), as well as being computationally inexpensive since simple sums over (θ, ϕ) bins replace functional minimization. The elementary acceptance demand also increases the efficiency over that of the 2π azimuthal symmetry since events scattering near the edge of the carbon analyzer have a greater probability of being accepted by this acceptance test than the ‘cone’ test (see figure 8). The π -symmetric acceptance requirement can also be realized by flipping the polarization of the incident particles. In the next section, it is pointed out that this has the added benefit that the effects of instrumental systematic errors cancel to first order when summing over the opposite polarizations.

III.2.3 Artificial Asymmetries

Artificial (or parasitic) asymmetries can arise when instrumental imperfections either cause events to be registered with greater efficiency at one ϕ scattering angle than at another, or cause events to be placed into the wrong angular (θ, ϕ) bins. Inefficiencies and misalignments in the post-carbon scintillators or wire chambers can pervert the expected $\cos(\phi)$ and $\sin(\phi)$ dependences of given normal and sideways scattering asymmetries (see equation 11), thus affecting the asymmetry extraction routines which *assume* these forms.⁵ As another example, a small-angle rejection cut not centered on zero degrees can also bias asymmetry extraction at angles near the cut limit. Some of these errors can be corrected for (see Section VII.2.1), but mostly they account for the remnant systematic error in

⁵Recall from Section III.1.1 that inefficiencies in the scintillators and wire chambers before the carbon only reduce the tracking efficiency of the polarimeter and not the p-C asymmetries or post-carbon acceptance.

the polarization determination . One can estimate the effect of the parasitic errors on the measured asymmetries by determining whether or not the polarimeter registers non-negligible asymmetries for *unpolarized* proton beams, where no asymmetries should exist [4].

To limit possible parasitic processes, a number of conditions must be met by each event before they can be considered for use in determining scattering asymmetries. These conditions are applied on top of the most basic requirement of sufficiently good wire chamber signals. In most systems, some or all of the following cuts are applied to all reconstructed candidate trajectories:

1. **Small-angle cut.** As mentioned previously, online small-angle rejection systems have coarse angular resolutions which are sufficient for cuts to reduce the useless data rate to tape, but are too imprecise for final polarization analysis. An uncentered cut will introduce unwanted asymmetries in the angular bins near the cut's edge. For this reason, a larger offline cut that results in a well-centered angular void needs to be defined prior to final analysis.
2. **Multiple tracks.** When using MWPCs (delay-line chambers cannot resolve multiple events), one discards events with multiple tracks in either the pre- or post-carbon wire chamber telescopes. This can be implemented either online or offline.
3. **Good event traceback to carbon.** The carbon scattering vertex must lie within the volume of the carbon analyzer. Also, the distance of closest approach between the incident and scattered trajectories must be closer than some amount s estimated by Monte Carlo simulation to be compatible with multiple scattering in the carbon. This latter cut discriminates against

events suffering either double nuclear scattering or excessive multiple scattering.

4. **Uncertain trajectories.** In those systems using least-squares fitting of 3 or more chamber positions to determine trajectories, events are kept only if the calculated χ^2 of the fit is less than some value, typically the square of the intrinsic chamber resolution. Used after test 2), this cut mainly eliminates events where a chamber misassigned a wire position.

Together, these conditions eliminate most sources that can compromise asymmetry calculations; and, of course, they are imposed on top of any other requirements of a particular experiment. However, even with such a ‘cleansed’ subset of events, parasitic asymmetries can still creep into the data.

Wire chamber misalignments in the post-carbon group are one source of parasitic asymmetries in the polarimeter system. Misalignments lead to angular errors in trajectory determination which cause erroneous assignment of angular bins after calculating scattering angles. The parasitic asymmetries resulting from small angular displacements $\Delta\theta$ can be determined approximately [2,5] by using events not scattered by the carbon analyzer (‘straight throughs’) and using these in the expressions

$$\Delta\epsilon_N(\theta) = \Delta\theta_y \frac{d}{d\theta}(\log I_0(\theta)) \quad (14)$$

$$\Delta\epsilon_S(\theta) = \Delta\theta_x \frac{d}{d\theta}(\log I_0(\theta)) \quad (15)$$

$$(16)$$

where the angular displacements $\Delta\theta_{x,y}$ are the means of the distributions

$$\Delta\theta_y = \langle \tan \theta \cdot \cos \phi \rangle \quad (17)$$

$$\Delta\theta_x = \langle \tan \theta \cdot \sin \phi \rangle \quad (18)$$

and where $I_0(\theta)$ is the observed (unnormalized) differential cross-section. If these errors are found to be significant, ‘corrected’ asymmetries can be obtained by straightforwardly subtracting these from the measured asymmetries.

As explained in Section III.2.2, the post-carbon acceptance can be mapped out and then parameterized by a Fourier series (equation 12). This function includes contributions from chamber and scintillator inefficiencies in addition to the geometric acceptance. Potentially, these spatially-dependent inefficiencies are the largest source of parasitic errors since even marginally preferential detection of protons scattered to the ‘left’ (say) compared to the ‘right’ will result in measurable asymmetries. Fortunately, one can correct for these effects using the acceptance function, $D(\theta, \phi)$.

The ratios of the first coefficients in the series expansion of $D(\theta, \phi)$, $\frac{a_1}{a_0}$ and $\frac{b_1}{b_0}$, represent the systematic errors to first order on the ‘normal’ and ‘sideways’ asymmetries, respectively. It is straightforward to show [6] that when summing over opposite beam polarizations, the first order parasitic errors cancel and only a second order correction of the form $\frac{a_2}{2a_0}$ remains, in the case of normal asymmetries. As an example, Aebischer, *et al.* [18] reported parasitic asymmetries of 0.007 for one beam polarization, but 0.0001 when summing over opposite polarizations, a value which was completely negligible compared to their statistical error. Even in those cases where the beam polarizations are opposite in sign, but unequal in magnitude, one can still expect the parasitic asymmetries to largely cancel to first order when the data is properly normalized.

III.3 SCATTERING EFFICIENCY and the FIGURE-OF-MERIT

When discussing inclusive cross-sections and analyzing powers in the previous section, it was noted that at a given energy and angle, these quantities varied with the thickness of carbon analyzer used. Increasing carbon thickness increases the probability that the incident protons will undergo a ‘useful’ reaction, hence increasing data rates. Unfortunately parasitic reactions (*e.g.* nuclear breakup) that remove useful flux from the polarimeter, and inelastic processes with low analyzing powers also increase in probability [15]. Also, the p-C multiple scattering cone starts to venture into angles where significant nuclear scattering analyzing powers exist, again reducing effective analyzing powers at small angles. The accuracy to which reaction angles can be determined diminishes with increasing carbon thickness due to the multiple scattering. At lower proton energies (< 200 MeV) where the angle-averaged p-C analyzing power is a strong function of energy (see figure 9), the uncertainty in the proton’s reaction energy due to energy-loss straggling in the carbon leads to an increased uncertainty in the extracted polarization due to an ambiguously modified effective analyzing power [15]. Clearly then, at a particular proton energy there will be a carbon thickness which balances the beneficial and detrimental effects to provide optimum polarimeter performance. The following paragraphs introduce the polarimeter scattering efficiency and the figure-of-merit, and show how they can be used to determine scattering rates and optimal carbon thicknesses. The notations used follow those in reference [15].

The fraction of protons suffering a useful scattering into the angular range $(\theta, \theta + d\theta)$ defines the **differential polarimeter efficiency**, $\alpha_u(\theta)$:

$$\alpha_u(\theta)d\theta = \frac{N_u(\theta)}{N_{incident}}d\theta \quad (19)$$

where $N_u(\theta)$ is the number of useful events (satisfying all the imposed cuts), and $N_{incident}$ is the *total* number of protons incident on the polarimeter. The **global efficiency**, α_u , is then simply the differential efficiency integrated over all useful angles:

$$\alpha_u = \int_{\theta_{min}}^{\theta_{max}} \alpha_u(\theta) d\theta \quad (20)$$

where θ_{min} is chosen to exclude the multiple scattering cone (therefore a function of proton energy), and θ_{max} represents the maximum scattering angle consistent with the geometric-acceptance symmetry adopted. Scattering efficiencies can be determined straightforwardly using unpolarized monochromatic proton beams without a small-angle cut in effect; however, like the inclusive analyzing powers, they depend on carbon thickness. Therefore one would like to determine the scattering efficiencies with the *optimized* analyzer thickness determined for each proton energy. These optimal carbon thicknesses are determined using the figure-of-merit.

Assuming Poisson statistics, it can be shown [7] that the statistical error in measuring the asymmetry $\epsilon(\theta)$ for $N(\theta)$ events scattering into an angular bin at θ degrees is

$$\Delta\epsilon(\theta) = \frac{\sqrt{2}}{\sqrt{N(\theta)}} \quad (21)$$

Using the definitions $N_u(\theta) = N_{inc} \cdot \alpha_u(\theta)$, $\epsilon(\theta) = P(\theta) \cdot \mathcal{A}(\theta)$, and integrating over all useful scattering angles (typically 5° to 20°), one derives the statistical error on the polarization with N_{inc} incident protons as:

$$\Delta P = \frac{\sqrt{2}}{\mathcal{F} \cdot \sqrt{N_{inc}}} \quad (22)$$

where the quantity \mathcal{F} is called the polarimeter **global figure-of-merit** defined as

$$\mathcal{F}^2 = \int_{\theta_{min}}^{\theta_{max}} \mathcal{A}^2(\theta) \cdot \alpha_u(\theta) d\theta \quad (23)$$

$$= \int_{\theta_{min}}^{\theta_{max}} g(\theta) d\theta \quad (24)$$

The quantity $g(\theta)$ is called the **differential figure-of-merit**, analogously to the differential scattering efficiency. Knowledge of \mathcal{F} for every proton energy-carbon thickness combination enables experimenters to accurately determine the beam time necessary to achieve a desired statistical accuracy. Since \mathcal{F} is a function of analyzing power and scattering efficiency, both of which depend on the carbon thickness used at a particular energy, a reasonable definition of optimum carbon thickness would be that thickness which maximizes \mathcal{F} , hence minimizes the statistical error ΔP for a given number of incident protons (*i.e.* beam time). To determine \mathcal{F} , one needs to measure both $\mathcal{A}(\theta)$ and $\alpha_u(\theta)$ over a range of carbon thicknesses. This program has been carried out by the POMME collaboration for their polarimeter [15] with several incident proton kinetic energies (at the center of the analyzer) between 0.5 and 1.2 GeV, with one additional energy at 200 MeV. They find optimum carbon thicknesses around 30cm for 500 MeV and above, and 7.2cm at 200 MeV. At 500 MeV, their figure-of-merit \mathcal{F} for 30 cm thick carbon is considerably larger ($\sim 1.5X$) than their value of \mathcal{F} at 15 cm. Compared to the thicknesses used by other groups in this energy range (*e.g.* McNaughton, *et al.* [1] : 12.7 cm ; Waters, *et al.* [6] : 6 cm), operating with this carbon thickness provides a considerable savings in beam time. On the other hand, their 7.2cm value at 200 MeV lies in the range of thicknesses typically used by most groups near this energy. These results demonstrate the usefulness of the figure-of-merit in determining optimum operating conditions, and furthermore suggest the desirability of determining the inclusive analyzing powers and scattering efficiencies at these optimum carbon thicknesses. (For more information, see reference [15]).

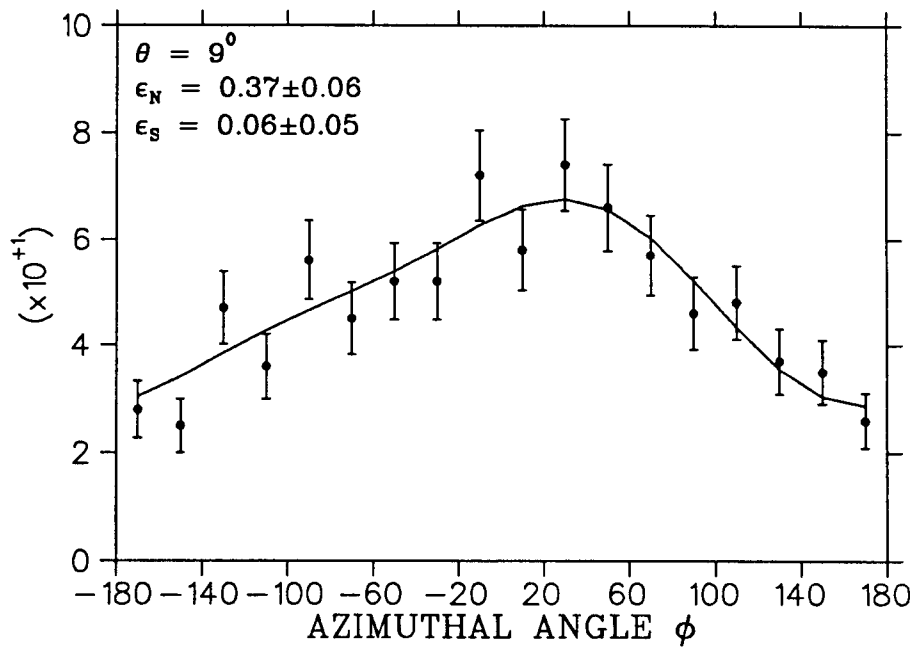


Figure 5: ϕ -distribution for one particular carbon θ scattering bin. The superimposed curve represents a 2nd order Fourier fit to this distribution, yielding the asymmetries shown.

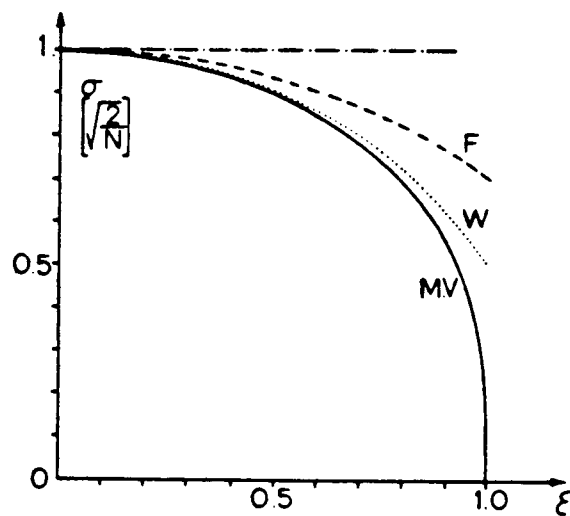


Figure 6: Normalized standard deviations in the calculated asymmetry for log-likelihood (MV), χ^2 -minimization (F), and the weighted-sums technique of Besset, *et al.* (W), as a function of the asymmetry. Note that the log-likelihood results represent the theoretically minimum errors for estimators. (from Besset *et al.* [19])

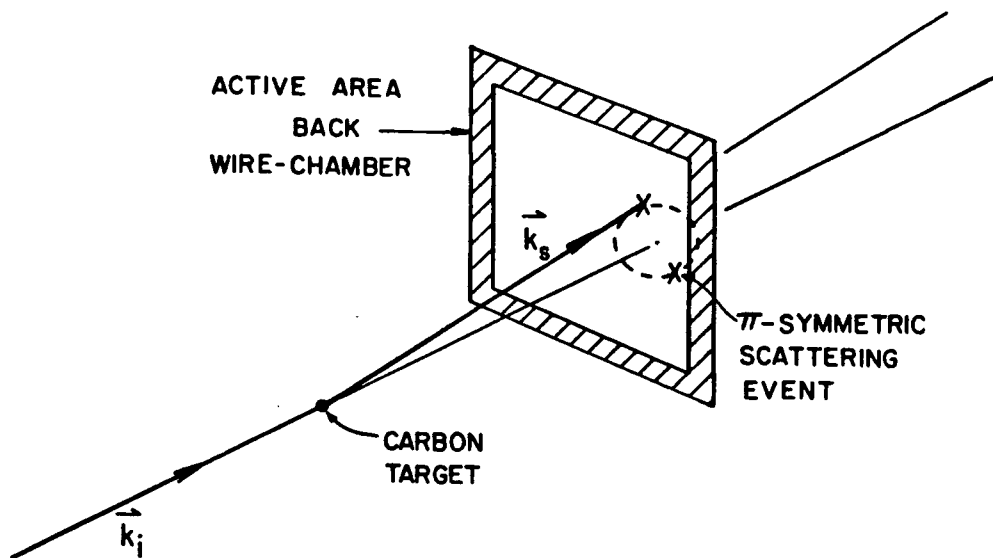


Figure 7: Diagram depicts the 2π azimuthal acceptance test (dashed line), the π azimuthal acceptance ' $\phi + \pi$ ' test (marked with an 'X'), and the 'full' acceptance (whole rear chamber region apart from hatched area). The event shown passes the full and π acceptances, but fails the 2π acceptance.

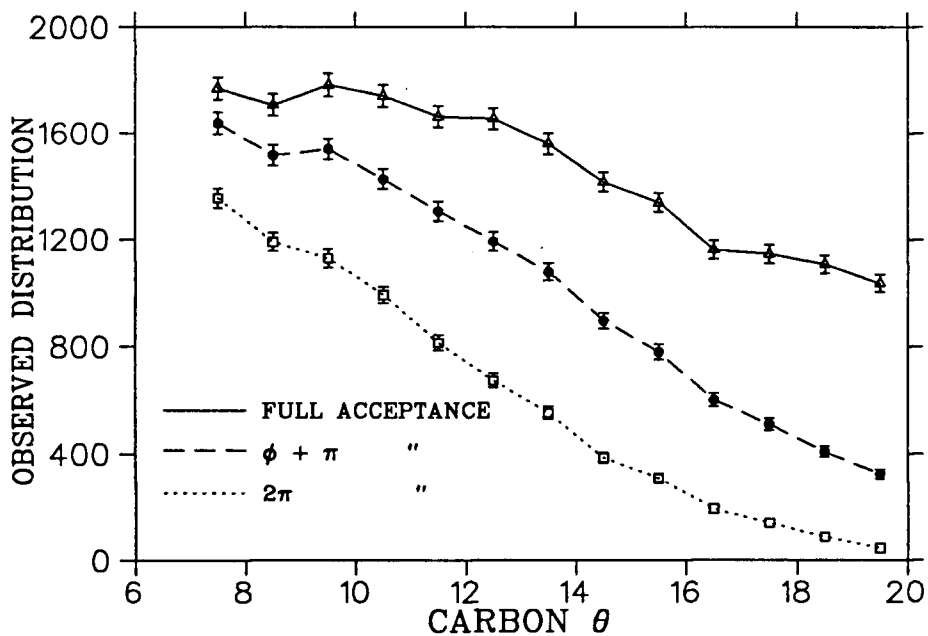


Figure 8: Angular distributions showing events passing the full acceptance test (solid line), the $\phi + \pi$ test (dashed line), and the 2π symmetry (cone) test (dotted line), for a fixed number of incident protons.

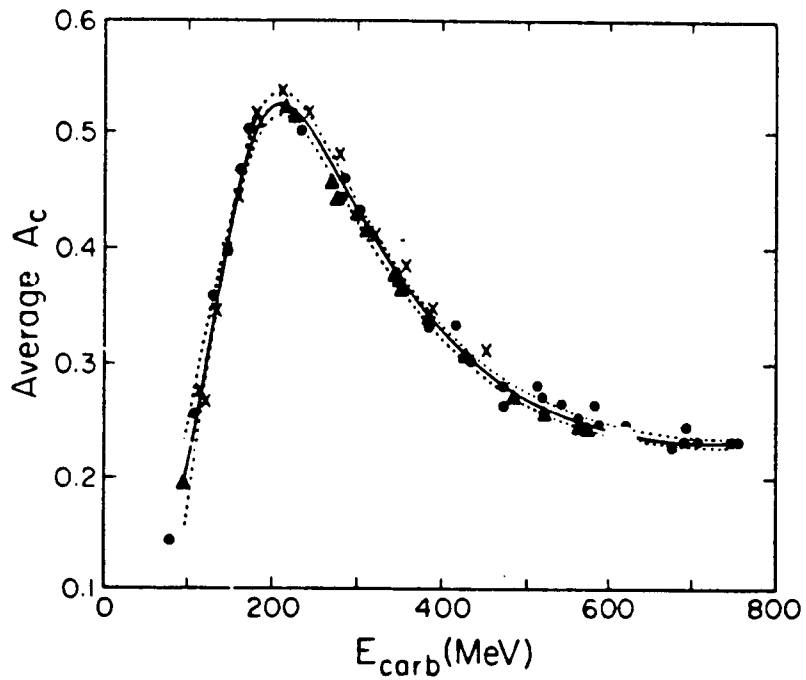


Figure 9: The angle-averaged analyzing power for inclusive proton-carbon scattering as a function of proton kinetic energy at the center of the carbon. (from McNaughton, et al. [1])

Chapter IV

Multi-Wire Delay-Line Drift Chambers

This chapter will present some of the basic principles associated with the operation of multi-wire delay-line drift chambers (DDCs). The initial discussion of the theory behind drift chambers provides the necessary background for the subsequent sections on delay-line chambers which outline in general how position and efficiency information can be extracted from the four chamber signals. Details of the specific calibration techniques used in the analysis of our polarimeter system will be left to Chapter VI.

IV.1 BASIC DRIFT CHAMBER PRINCIPLES

IV.1.1 Pulse Formation

Gaseous ionization chambers operate on the well known principle that charged particles passing through matter deposit some of their energy to the surrounding atoms through electromagnetic interaction. The atoms absorb the energy by: a) ionization to form a free electron and a positive ion (if the energy-loss by the passing particle is high enough), or b) excitation to a metastable state which can subsequently de-excite by photon radiation, or ionization through atomic collision

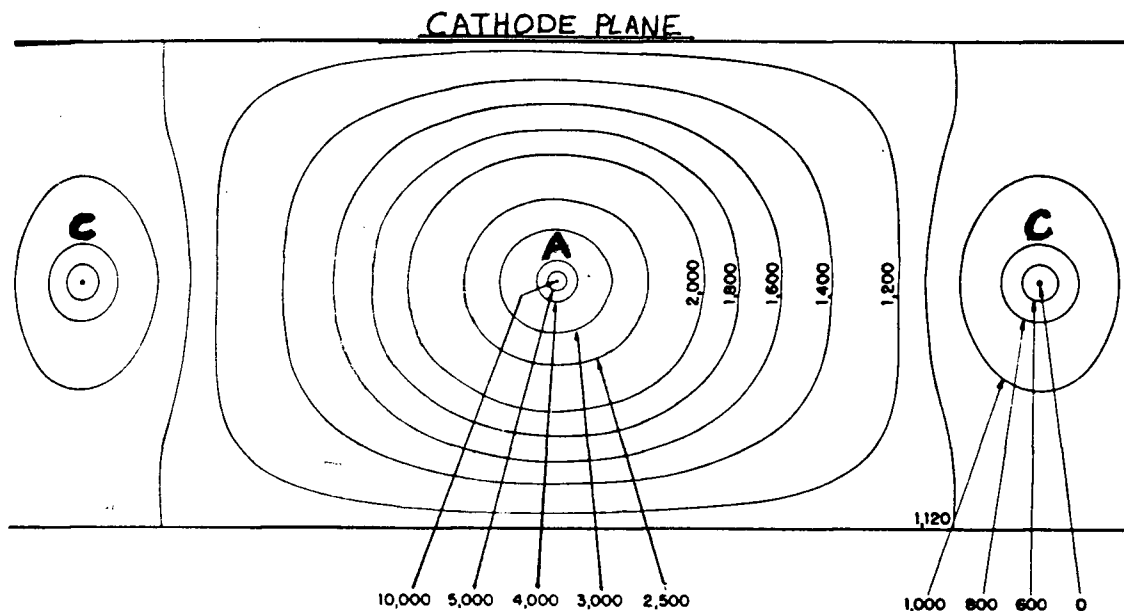


Figure 10: The unit cell for a typical drift chamber. The equipotential lines are for the anode wire at positive high voltage and the surrounding cathode wires and cathodes planes at ground potential. These lines clearly show the regions of uniform and $\frac{1}{r}$ radial dependence of the potential. (field map from Walenta [21])

(Penning effect). These **primary** electrons may induce other, **secondary**, ionizations. Normally, these primary-plus-secondary electron-ion pairs, (~ 1 pair-per-30 ev energy loss) will quickly recombine into neutral atoms, but in the presence of an external electric field, electron and ion 'clouds' drift apart. In chambers of the kind used in our polarimeter, thin anode wires maintained at a high positive d.c. voltage provide the source of the field with respect to adjacent cathode wires and planes at ground potential. Such a configuration is called the **unit cell** (refer to figure 10).

In the unit cell of a drift chamber, the anode and cathode wires are arranged to provide as constant a field-gradient between them as possible so that the electrons and ions drift with relatively uniform velocity. However, the electrons begin to accelerate when they electrons enter the cylindrical $\frac{1}{r}$ region of the anode

potential (a few wire radii from the anode). Above a certain threshold voltage, the electrons will gain enough energy between collisions to initiate **avalanche** electron multiplication. ¹ Sauli [22] shows that the drifting ions produced in the avalanche distort the electric field, thus inducing pulses on the anode and cathode wires simultaneously. (For most commonly used fill gases, the contribution to the resulting pulses from the drifting electrons can be safely neglected). Due to the avalanche multiplication, these pulses are large enough to be detected electronically. Furthermore, they occur almost immediately after avalanche (~ 1 nsec) and exhibit very sharp risetimes, typically < 5 nsec at the anodes and < 15 nsec at the cathodes. In conjunction with fast timing electronics like leading-edge or constant-fraction discriminators, very good timing resolutions are possible on both the anode and cathode signals.

IV.1.2 Drift Information

The timing of the pulses forming at the anode wires in a multi-wire drift chamber contain information pertaining to both the rough position of the charged particle trajectory through the chamber (namely the nearest anode wire), and also the position in the unit cell *between* the anode and cathode wires. As previously mentioned, the unit cells in drift chambers are designed such that the initial ionization clouds drift with more-or-less constant velocity across the anode-cathode gap, except for the region very near the anode wire. Therefore, if the arrival of a pulse at a single anode (or cathode) is timed with respect to some system **prompt** (*e.g.* polarimeter scintillator coincidence) which defines $t = 0$, one would expect to get a timing distribution (**drift-time spectrum**) much like that of figure 11 when the incident charged particles uniformly illuminate the unit cell.

¹The primary ions collected at the cathode wires do not avalanche since their velocities are much lower than electrons and the thicker wires do not have as strong a $1/r$ field.

For typical gap widths of 2-10 mm, uniform unit cell illumination is an excellent approximation.

The broad flat central region indicates that the electrons are drifting with uniform velocity in the central gap regions. Once electrons enter the avalanche region, they accelerate and collect at the anode very quickly. Incident charged particles that pass anywhere within the avalanche region will cause virtually instant pulses at the associated anode wire yielding signals with essentially the same drift time. This accounts for the spike at short drift times in figure 11, which will vary in height depending on the width of the avalanche region due to the anode voltage. The tail at long drift times comes from events occurring near the cathode. Since the ionization must travel the whole gap width, these events suffer the most from timing ‘jitter’ due to spatial broadening of the clouds due to diffusion [22].

The drift-time to drift-distance relationship can be determined using the the measured drift time distributions and the assumption that the unit cell is uniformly illuminated [23]. For a uniformly illuminated cell, the following expression holds:

$$\frac{dN}{ds} = \frac{dN}{dt} \cdot \frac{dt}{ds} = \text{constant} \quad (25)$$

where dN is the number of events occurring in the drift-time increment dt , or the drift-space increment ds . Note that $\frac{dN}{dt}$ represents mathematically the form of the drift-time distribution. Rearranging terms and integrating, we find:

$$ds = c \cdot \frac{dN}{dt} \cdot dt \quad (26)$$

$$\Rightarrow s(t) = c \int_0^t \frac{dN}{dt} dt \quad (27)$$

The drift distance from the anode wire corresponding to a drift time t can be calculated simply by integrating the drift time distribution up to time t (see figures 34 and 35 on page 87). The normalizing constant, c , is found by

recognizing that integration of the entire drift time spectrum gives the maximum drift distance, corresponding to the unit cell gap width.

IV.1.3 Left/Right Ambiguity

After determining the anode wire that ‘fired’ and the drift distance to this wire, one still cannot uniquely determine the position of the event in the unit cell. Without additional information, it is impossible to know on which *side* of the anode wire the event occurred: this is known as the **left/right ambiguity**. One method to resolve the ambiguity involves another plane of wires behind the first, but displaced half the gap width. Knowledge of the anode in the second plane that fired will allow one to infer the drift side in the first plane. This technique has been used extensively (*e.g.*[6]) in the past, but it suffers from the increased cost of requiring two chambers (and associated electronics) to determine one coordinate, as well as the parallax problem for trajectories having large incident angles to the chambers. Another method employing the cathode wires solves both of these problems and has found widespread acceptance in recent years.

Originally, the cathode wires were not used for position tracking but simply as field defining wires that separated the various drift cells in a chamber. Then Walenta [21] pioneered a technique where the pulses induced on the cathode wires adjacent to the firing anode were used to resolve the left/right ambiguity. In the voltage plateau region of a proportional chamber (defined Section IV.1.5), the avalanching electrons do not spread along the length of an anode wire, but instead highly localize in a region transverse to the primary ionizations [22]. Previous to Walenta’s work, it was widely believed that the avalanche developed in a cylindrically symmetric fashion around the anode wire, thus losing any memory of the side of the anode wire on which the avalanche initiated. However, it was discovered [25] that below a certain avalanche size (of order $5 \cdot 10^7$ ion pairs), the

avalanche cloud does not completely surround the anode, but instead localizes on the side nearest the primary ionizations. The sizes of the induced pulses on the adjacent cathode wires could differ by as much as about 10%, largely independent of the fill gases, voltages, and unit cell geometries adopted [21]. Consequently, simply the sign of the difference of the charge-integrated pulses on the adjacent cathode wires indicates on which side of the anode wire an event occurred. This technique has been found to work well with many systems [14,21,24], with the chief advantages over the staggered wires method being decreased cost and improved performance for trajectories with large incident angle.

IV.1.4 Fill Gases

The choice of fill gas determines most of the operating characteristics of any wire chamber. In general, one desires the fill gas to provide high gain, high drift velocities (implying good rate capability), and small parasitic ionizations, all at a reasonably low applied voltage. Noble gases are normally used since they ionize at the lowest electric fields, with argon being favoured in DDCs due its high specific ionization and low cost. Unfortunately, metastably excited argon atoms can de-excite by radiating 11.6 eV photons which can liberate photoelectrons from the cathodes, causing subsequent parasitic avalanches. Polyatomic gases like CO_2 and isobutane are introduced as **quenchers** as they absorb these radiated photons via nonradiative vibrational or rotational excitations, and subsequently dissipate their excess energy during collisions or by molecular dissociation. Although slightly higher threshold voltages are required, quenching results in much higher gas gains, *e.g.* from $\sim 10^4$ in pure argon to $\sim 10^6$ in an argon-isobutane mixture. Also, drift velocities are found to increase in quenched gases [22]. Noble gas/quencher ratios vary considerably, but a mixture of 65%-35% argon-isobutane appears to one of the most frequently used [28].

In addition to the noble gases and quenchers, very small amounts of electronegative gases like freon and oxygen are often added to trap electrons emitted from the cathodes after ion capture. The presence of these gases permit another order of magnitude increase in gas gain [26]; however excessive amounts degrade efficiency by trapping electrons from particle ionizations, especially in drift chambers with large gap widths. It follows that it is very important to prevent the entry of any oxygen through leaks or impure gas.

IV.1.5 Chamber Operating Voltage

The choice of a practical operating voltage for multi-wire drift chambers is based on a compromise between three competing effects in the chambers.

Firstly, particle detection efficiencies level off at a value approaching 100% for a range of anode voltages known as the **efficiency plateau**. The existence of such a plateau implies that only for a very small fraction of the events do the primary ionization electrons recombine before initiating avalanche multiplication. The threshold and width of this region are important parameters for a chamber.

Secondly, the sizes of the anode and cathode voltage pulses are directly proportional to the energy-loss of the incident particle for applied voltages above the **proportionality threshold** (hence the term 'proportional counter'). Eventually, above some critical voltage, proportionality ends and spontaneous discharges in the gas cause noise pulses develop. These noise discharges also indicate the end of the efficiency plateau since erroneous signals will cause an efficiency $>100\%$ to be recorded.

Lastly, as discussed in Section IV.1.3, the cathode wires can be used to resolve the left/right ambiguity, provided that the number of avalanching electrons is **below** a certain value. This implies that there exists a critical voltage above which the left/right ambiguity cannot be well resolved, hence setting a voltage

limit for high resolution particle tracking.² Furthermore, the left/right differentiation can be expected to be optimum at some voltage below this limit (and yet above the avalanche voltage). Therefore, for high resolution operation, a practical operating voltage is chosen as one for which the left/right differentiation is optimum as long as this optimum voltage is not too close to the avalanche threshold. If it is, a compromise value is chosen at the center of the region in the efficiency plateau below the left-right ambiguity voltage limit. This choice reduces the effects on chamber efficiency of slight voltage variations from power supplies, and variable chamber currents induced by varying charged-particle fluxes. If only the anode wire position information is to be used, the operating voltage is chosen at the center of the efficiency plateau region below the discharge limit.

IV.1.6 Chamber Aging and Cleaning

As mentioned in Section IV.1.4, organic quenchers dissipate their excess energy (obtained from photon absorption) through various molecular dissociation processes. Unfortunately, the simpler radicals which result often recombine to form long liquid or solid polymer chains which can deposit on the anodes or cathodes. Over long periods of time such accumulations can increase on the cathode to the point where positive charges ('space charges') build-up since they cannot diffuse quickly enough through the polymer coating. Such space charges 'screen' the cathode from subsequent event pulses. Visible effects of such 'aging' include reduced efficiency and a narrowed voltage plateau. Of even more concern is the possibility that high voltage discharges can occur which can damage both the wire and the detection electronics.

To inhibit polymer build-up, non-polymerizing liquid agents like methylal

²Above this voltage and below the discharge region, the anode wires can still be used for coarse position resolution.

and isopropanol are introduced to the noble gas-quencher mixtures by ‘bubbling’ the primary gas mix through the liquid, picking up roughly 0.5% vapour by volume. Although they do not completely stop polymer formation, these agents greatly increase the life of a chamber .

Any polymers and dust particles that have collected and formed on the wires can be partially removed by a process of **reverse biasing** of the chamber prior to use; only manual cleaning can completely remove all the debris. Reverse biasing results when a large *negative* voltage is applied to the anode instead of the usual operational positive high voltage. The resulting heavy-ion bombardment frees dust and loose polymer flakes electrostatically attached to the wires, subsequently ‘sweeping’ them away by the flowing gases. Voltage discharges often occur during this cleaning stage and cease only when all loose particulates are freed. This procedure is usually carried out immediately prior to a run, especially if room air had been allowed to enter the chamber. The negative voltage is increased until significant discharge currents develop (\sim few μ amps). The voltage at which such discharges occur moves to higher and higher values as the chamber gets cleaner, with the limiting value being at a voltage somewhat lower in magnitude than the usual operating voltage. However, if the discharges do not cease, and the negative voltage cannot be raised up to a suitable level, the chamber is probably very ‘dirty’ and must be opened and cleaned by hand. (See table I in Section V.1.2 for operational and reverse-biasing voltages used with our wire chambers).

IV.2 DELAY-LINE CHAMBERS and POSITION EXTRACTION

Multi-wire delay-line drift chambers offer an inexpensive alternative to the amplifier-per-wire readouts found in many systems. Large chambers containing

dozens of anode wires can become prohibitively expensive if equipped with preamplifiers on every wire. On the other hand, delay-line chambers require only two anode amplifiers regardless of the chamber's size, drastically reducing both the cost and the maintenance of the electronic readout. Furthermore, they offer basically the same resolution and efficiency performance as drift-chambers with wire-by-wire readouts. Of course, this approach has own its drawback: a low rate capability ($\sim 10^6 s^{-1}$ per wire plane [27]) due to the increased dead-time from the delay-line, and the inability to provide tracking information for multi-particle events.

IV.2.1 Chamber Geometry

A series of unit cells (of the type illustrated in figure 10) make up one plane of a delay-line drift chamber (hereafter DDC). The delay-line typically consists of a printed-circuit board coated with copper etched into a tight zig-zag pattern [29] with tabs to allow anode wire connection. The anode wires are directly connected under tension to the delay-line, spaced so as to provide some measurable signal delay between adjacent wires. The tension reduces the small displacements between the wires due to electrostatic instabilities when under high voltage, as well as the gravitational 'bowing' when the wires run horizontally. Similarly, the cathode wires are also directly connected under tension, but in this case alternately to two grounded, non-dispersive buses, labelled 'ODD' and 'EVEN'. The single anode outputs at each end of the delay-line, dubbed 'left' (L) and 'right' (R), are connected in parallel to large resistors to control voltage shifts arising from current fluctuations. Capacitors block each end to DC voltages to allow a positive high voltage to be applied to the anodes. Usually, two such wire planes are oriented orthogonally in one DDC unit to provide both X and Y coordinates. A schematic diagram of such a wire plane appears in figure 20.

IV.2.2 Fundamental Chamber Signals

DDCs have four outputs per chamber plane which provide the five signals used to uniquely determine the position of an event, together with a signal indicating whether or not the event was a ‘good’ single-particle hit. These five signals are:

- t_L, t_R - the anode timing signals from the left and right ends of the delay-line. The ionization cloud resulting from passage of a particle through a DDC first must drift towards the nearest anode before causing a pulse-inducing avalanche. This anode pulse then splits at the delay-line into two signals travelling in opposite directions, one to the left and the other to the right anode preamplifiers, respectively. After further electronic ‘treatment’, these signals continue on until eventually stopping their respective time-to-digital converters (TDCs), which have been previously started by a system prompt. Consequently, each anode timing signal can be decomposed into four basic components:

$$t_L = t_{drift} + n \cdot D_a + K_L + h.o.t \quad (28)$$

$$t_R = t_{drift} + (N - n) \cdot D_a + K_R + h.o.t. \quad (29)$$

where n and N are the wire number at which the avalanche occurred and the total number of wires, respectively; D_a is the time-delay between anode wires; t_{drift} is the drift-time; and $K_{L,R}$ are constant delays associated with propagation times from the chamber to the TDCs. Slight differences in the characteristics of the electronics of each channel and non-linearities in the delay-line contribute to the higher-order correction terms (h.o.t.).

- E_{odd}, E_{even} - analog signals taken from the ODD and EVEN cathode buses and recorded by charge-integrating or peak-sensing analog-to-digital converters (ADCs). These signals differ by only $\sim 10\%$ as mentioned

previously. The difference between these signal sizes resolves the left/right ambiguity; therefore it's important that mutual variations in gain and/or offset be corrected for. In Section VI.2.4 such calibration procedures are discussed.

- t_{cath} - timing signal taken from one of the ODD or EVEN cathode buses. Since the voltage pulses occur simultaneously at the anode and the adjacent cathode wires, both readout systems will record the *same* drift-time component. In principle, the cathode timing signal should contain just a constant delay plus the drift-time, but even low-dispersion cathode buses introduce some delay per unit length which cannot be neglected even to first order. The dispersion delay can be corrected for with knowledge of the length of bus traversed by the signal pulse. One cannot determine the location of an event along the cathode bus exactly, but it can be estimated by using the position of the anode wire n registering the event. The cathode time can then be expressed as:

$$t_{cath} = t_{drift} + n \cdot D_{bus} + K_{cath} \quad (30)$$

where D_{bus} is the delay per unit length of the cathode bus, and K_{cath} accounts for a constant delay from the signal cabling.

IV.2.3 Position Determination

Using equations 28 and 29, it is clear that the anode wire number can be calculated by taking the difference

$$t_L - t_R = n \cdot (2D_a) + [K_L - K_R - N \cdot D_a] + h.o.t \quad (31)$$

where the quantity in square brackets is a constant. A distribution of difference-time or **DIFFTIME** events, $t_{diff} \equiv t_L - t_R$, yields a familiar discrete 'picket-fence' or **COMB** structure as shown in figure 12.

The above equation implies that the wire number is linearly related to the difference in arrival times of the left and right anode signals. All electronic systems behave non-linearly to some degree and therefore in general there are non-zero corrections to this expression. Most non-linearities should cancel in the timing difference; however, delay-line pulse dispersion can contribute non-linear terms that do not cancel in a simple linear difference. Voltage pulses slow down non-linearly in dispersive media, so events near a chamber's edge will produce left and right anode signals with maximally different average transmission velocities resulting from different *effective* delays per unit length. These effects are expected to be small and as such can be easily corrected for. Refer to Section VI.2.3 for a discussion of COMB calibration techniques.

Having determined the proper anode wire position, one can use equations 28 and 29 to determine the drift-time as measured by the anode electronics, or equation 30 for the drift-time measured by the cathode electronics. Generally, the faster anode signals provide better timing resolution than the slower cathode pulses, so the drift-time calculated by the anode signals is used in the position analysis [24]. The anode drift-time is obtained by calculating the SUMTIME

$$t_{sum} \equiv t_L + t_R \quad (32)$$

$$= 2 \cdot t_{drift} + N \cdot D_a + K_s + h_{at} \quad (33)$$

This expression is seen to be independent of the position along the delay-line at which the event occurred. A typical distribution appears in figure 11. Recall from the discussion in Section IV.1.2 that ultimately this spectrum is integrated and normalized, which is then used to determine the drift-distance. This means that in any case, integration should 'smooth out' small non-linear effects and render them insignificant compared to the linear behavior.

ODD - EVEN and Left/Right Ambiguity

Finally, one needs the cathode ODD and EVEN analog signals to resolve the left/right ambiguity and thus to pin down the position of an event. In principle, one merely calculates the sign of the difference $E_{odd} - E_{even}$ to determine on which side of the anode wire an event occurred. However, the situation is not quite so simple in multi-wire chambers. If an ODD cathode wire is on the right side of one anode wire, it is also on the *left* of an adjacent anode wire. So without more information, one does not know whether to add or subtract the drift distance from the anode wire position in order to calculate the trajectory coordinate. The final piece of information required is the relationship between the cathodes and the anode wire number in the chamber. *e.g.* the ODD wires can be chosen to be on the left of all odd-numbered anode wires, so drift distances will be (say) subtracted from these wire positions, and added to the even-numbered positions.

Cathode signal pulse-sizes generally exhibit a broad range of values (figure 13) which depend on the particle energy-loss and the drift distance. To remove this energy-loss dependence of the $E_{odd} - E_{even}$ signal, a common technique involves the normalized difference of the ODD and EVEN pulses to solve the left/right ambiguity

$$O - E \equiv \frac{E_{odd} - E_{even}}{E_{odd} + E_{even}} \quad (34)$$

This form compensates for variations in pulse-size from events distributed around the unit cell without introducing any new parameters.

Figure 14 shows a typical normalized ODD - EVEN spectrum. The cathode pulse-size difference can be realized either by using special hardware subtraction circuitry [14] where only the difference signal is recorded on tape; or by recording both the 'raw' ODD and EVEN signals separately and calculating the difference in software [24]. The latter technique has been adopted for our analysis and will be

discussed in detail in Section VI.2.4.

IV.2.4 CHECKSUM and Chamber Efficiency

Using the drift-times measured separately by the anode (t_{sum}) and cathode (t_{cath}), it's possible to determine whether or not a signal arose from a 'good' chamber event. As mentioned earlier, both the anodes and cathodes 'see' the same drift-time, so barring bad events (like background events, noise, or multiple hits), the difference between their respective drift-times should yield a constant arising from the difference in their timing offsets. In practice, the anode SUMTIME, measured by the sum of t_L and t_R , is actually double the anode drift-time, and so using equations 28, 29, and 30, we write the difference in the anode and cathode drift-times, or **CHECKSUM**, as

$$t_{checksum} = t_{left} + t_{right} - g_1 t_{odd} + g_2 \cdot n + K_{cs} \quad (35)$$

where the constants g_1 and g_2 are nominally ~ 2 and $2 \cdot D_{bus}$, respectively (see Section VI.2.2). Figure 15 shows a typical checksum distribution.

In practice, the checksum is *the* quantity that reflects the detection efficiency of a chamber. The distribution has a large narrow peak corresponding to good single-particle events, a smaller peak corresponding to 'time-outs' (no anode event chamber information recorded), and a tail leading to the main peak corresponding multiple hits, background radiation, and parasitic avalanches preceding the ionization cloud to the anode. These effects vary with changing conditions such as beam rate and applied voltages, so the checksum is more indicative of a chamber's overall performance than merely indicating triggering efficiency. Since the peak is so narrow, the checksum is sensitive to even small timing errors like those due to miscalibrated discriminators (see Section V.2.2) and the premature avalanches caused by energetic knock-on electrons, or **deltas**. Deltas have been identified as

major causes of checksum failure in some systems [14], although not in others [4].
(see Sauli [22] for an excellent discussion on delta electron effects in gas chambers)

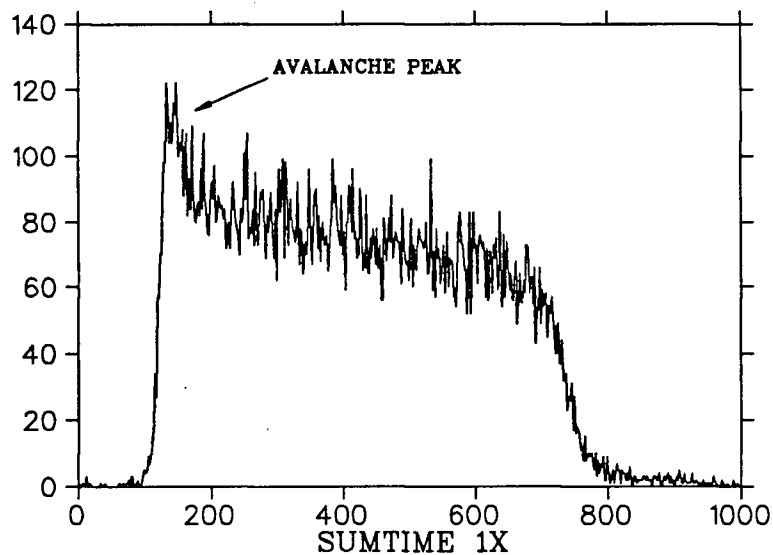


Figure 11: Typical distribution of pulse drift times at a drift chamber anode. Note the short time spike due to the avalanche and the long tail from events near the cathode.

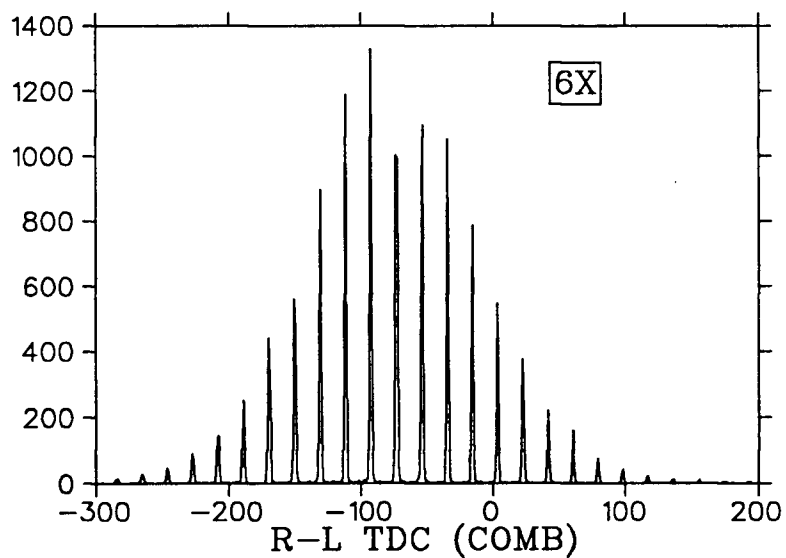


Figure 12: The typical COMB structure of a $t_L - t_R$ anode wire timing distribution. Each spike corresponds to one anode wire

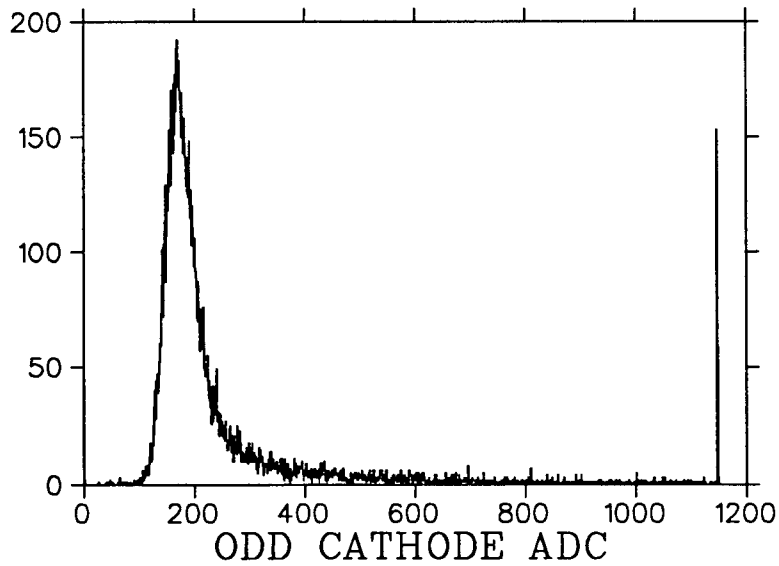


Figure 13: The distribution of charge-integrated cathode pulse-sizes resulting from a monochromatic beam of protons. The peak at channel 1150 indicates events that overflowed the ADCs.

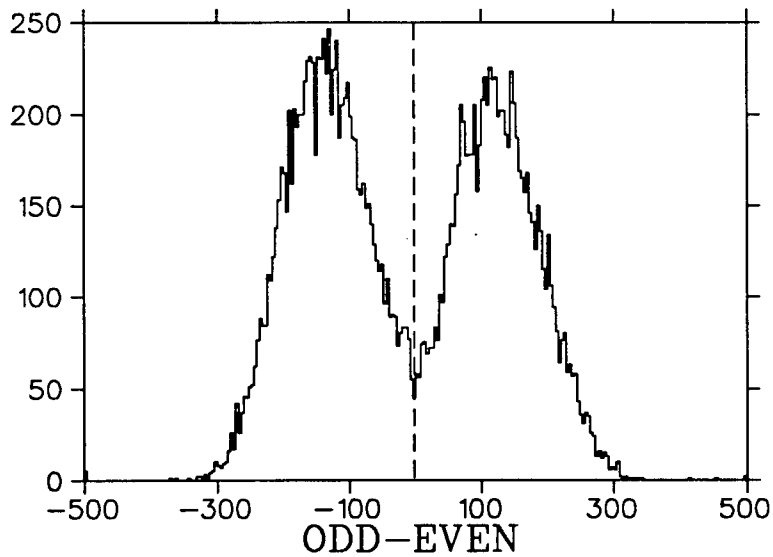


Figure 14: Typical example of a normalized ODD - EVEN distribution. The region in the valley corresponds to those events occurring near the anode wire for which the induced cathode pulse sizes are too similar to allow good discrimination (see Section VI.2.4).

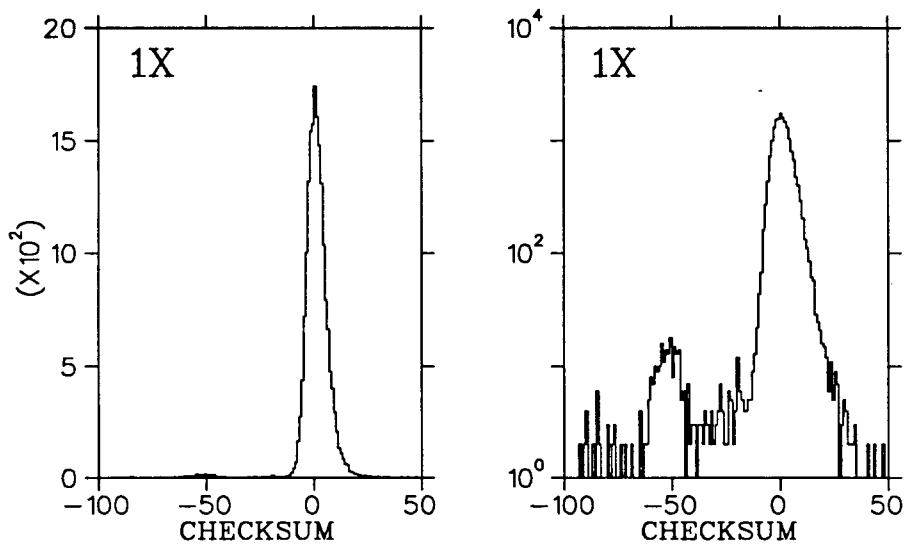


Figure 15: Typical checksum distribution for a delay-line drift chamber. The logarithmic scale on the right clearly shows the tail of bad events due to chamber inefficiencies, multiple hits, etc., leading up to the (gaussian) main peak.

Chapter V

The E331 Polarimeter System

V.1 CONSTRUCTION DETAILS

V.1.1 System Layout and Cart Construction

The E331 Polarimeter consists of an aluminum ‘cart’ supporting the carbon analyzer, a set of three equally spaced multi-wire delay-line drift chambers (DDCs) on either side of the carbon, two sets of scintillators before and after the post-carbon chambers, and all the chamber preamplifiers and power supplies. A second cart, or ‘arm’, consists of three equally spaced DDCs with a pair of scintillator sets at the front and back, along with the chamber preamps and power supplies. Figures 16 and 17 provide schematic representations of the polarimeter and second arm carts, respectively. The important dimensions are also provided. A photograph of the carts appears in figure 1 on page 2.

Both carts are constructed of aluminum angle channel throughout. The axis passing through the center of the wire chambers on either cart is nominally 137 cm above floor level, corresponding to beam height on the M11 pion channel at TRIUMF [30]. Each cart is also equipped with individually adjustable corner legs which allow for several centimeters of vertical adjustment. These legs can be fully retracted to allow the carts to be rolled on their attached wheels. Each cart can be rotated at a fixed radius about a target position by means of a long steel pipe

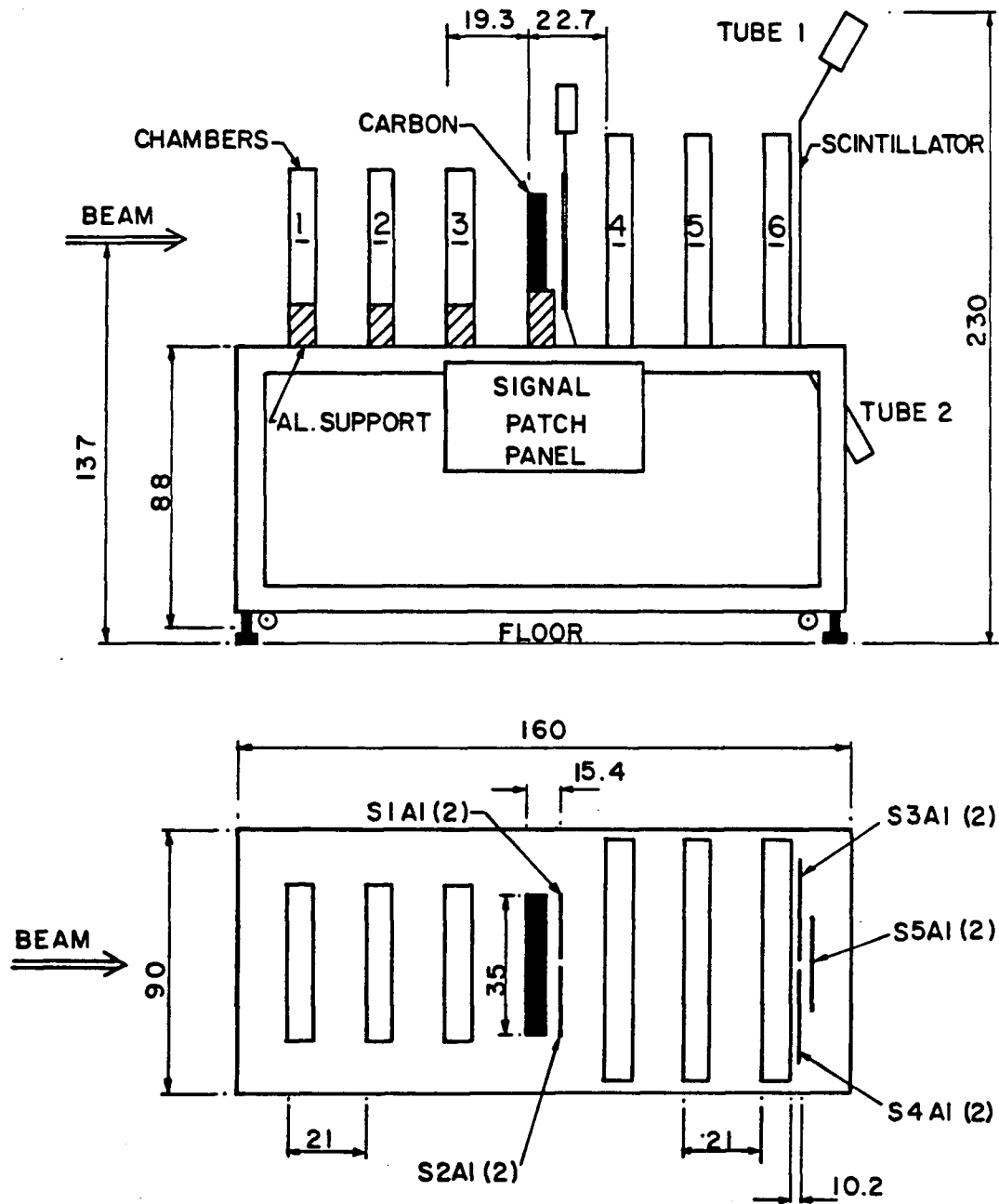


Figure 16: Side and top views of the polarimeter cart showing important dimensions and labelling schemes. All units in centimeters.

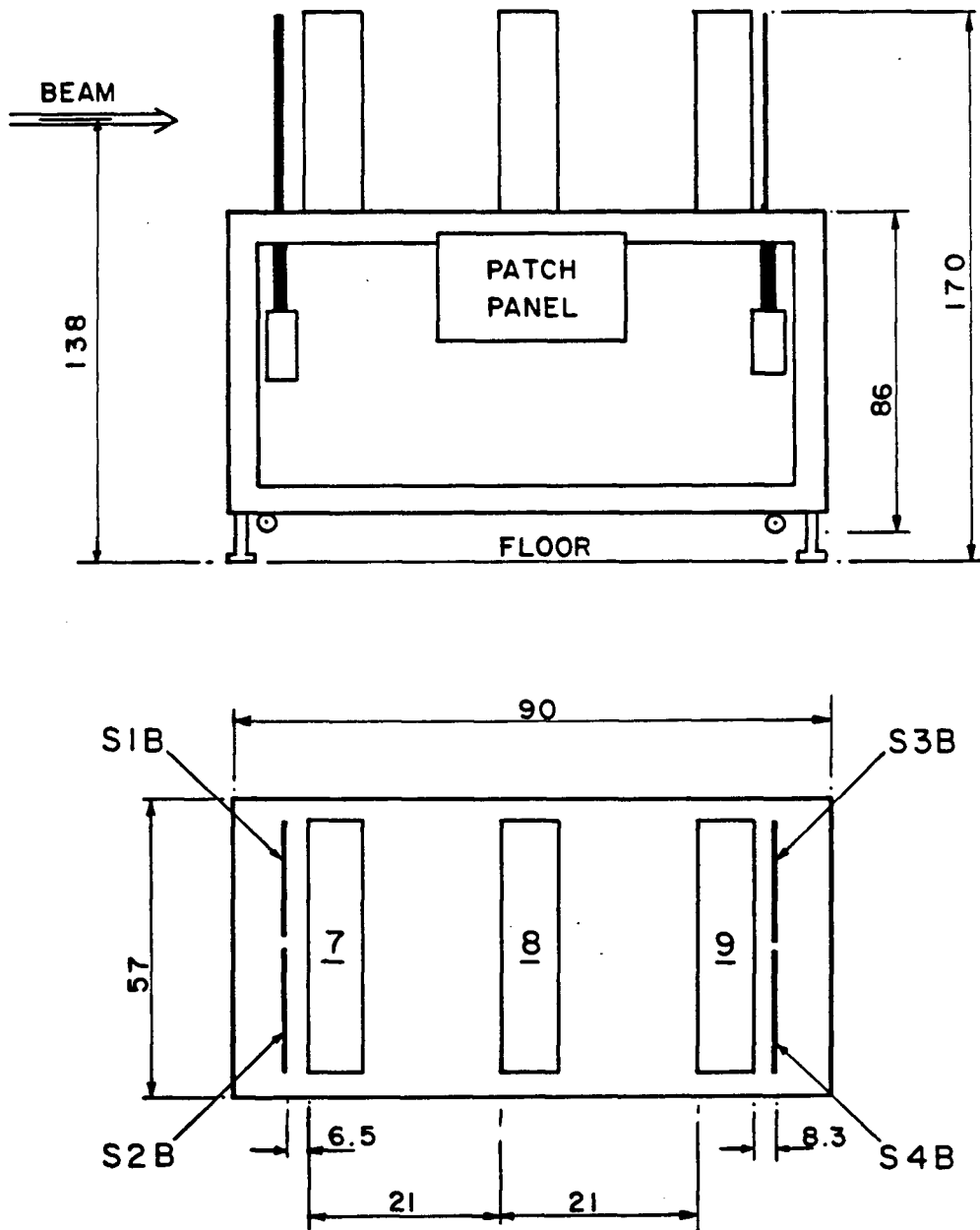


Figure 17: Side and top views of the second arm cart with dimensions and labelling schemes. All units in centimeters.

attached at one end with a freely rotating clamp to a cylindrical aluminum base at the target position, and at the other end to the cart base with fixed clamps at the front and rear. The target base can support the TRIUMF Polarized Deuteron Target [8], or an aluminum platform upon which target equipment can be positioned. The carriages also carry all the power supplies required for the chamber preamplifiers on internal tables. To tidy up cabling, patch panels are mounted on each cart, supporting all the coaxial, high voltage, and signal LEMO cable requirements.

Three small and three large frames for holding the wire chambers are mounted onto the polarimeter cart before and after the carbon analyzer, allowing the DDCs to be inserted or removed while the frames remain fixed to the cart. Blocks raise the small DDC frames so as to maintain a common central axis between the small and large chamber groups. The DDCs are fastened to the frames with set screws to provide rigid, reproducible positioning.

Our system employs three DDCs in each tracking group. DDCs were chosen since they were deemed to be more 'efficient' (in a broad sense) than the available proportional chambers. The better spatial resolutions of the DDCs chambers allows closer inter-chamber spacing to achieve a required angular resolution. For a given chamber size, this substantially increases the solid angle coverage of a DDC system compared to that achievable with a proportional chamber system. On the other hand, for given angular resolution and solid-angle requirements, DDC chambers can be constructed smaller than proportional chambers, thus saving on manufacturing costs. Three chambers were used (instead of two) to exploit the increase in overall tracking efficiency (see Section III.1.1). This is especially important when the polarimeter is used in secondary pion channel areas like M11 at TRIUMF, where the incident pion intensities are relatively low ($\sim 10^8 \text{ s}^{-1}$) [30], and thus secondary proton intensities are even lower.

Adjacent frames in each chamber group are mounted with a fixed 210 mm distance between centers. If different spacings are desired, positional adjustments of the frames can be made in 3 cm increments. With 210 mm separating adjacent x (or y) -wire planes, the anode wire spacing of 8mm will result in a $\sim \pm 0.5^\circ$ ($\pm 1\sigma$) angular error in trajectory determination when using only the anode wire position information and the outside chambers in each group (420 mm separation). Such an inter-plane separation ensures that in the worst case scenario of a complete loss of ODD-EVEN cathode information (necessary for high resolution operation of DDCs), the resulting angular error corresponds to the minimum acceptable resolution that can be tolerated in the polarization extraction routines without introducing unacceptable systematic errors [31].

The solid angle subtended by polarimeter and the second arm are defined by the active areas of chamber 3 and 9, respectively. (see figures 16, 17). Active areas of $\sim 900 \text{ cm}^2$ each correspond to 40 milliradians coverage at a typical 150 cm chamber-to-target separation. (Details of our DDCs appear later on in this chapter).

The carbon analyzer is mounted on a raised aluminum frame in the center of the polarimeter cart. The analyzer is composed of a sandwich of flat carbon sheets of various thicknesses. The measured density of the carbon is $\rho_C = 1.71 \frac{\text{gm}}{\text{cm}^3}$ ¹. The sheets measure typically 54H X 17.6W cm², and come in thicknesses of 1, 2, and 4 cm, with 4, 2, and 2 such slabs, respectively. Two sheets side-by-side are necessary to cover the active area of the solid-angle defining small chamber. The graphite sandwiches are held together by set screws around the perimeter of the frame so that the center of the analyzer is 210 mm from the adjacent wire planes (i.e. halfway between) and at beam height above the floor.

¹Our carbon analyzer slabs are in fact recut portions of the analyzer graphite used in the original BASQUE polarimeter.

The polarimeter cart is equipped with two sets of double-ended scintillator counters: one smaller set immediately downstream of the carbon analyzer, and the other, larger behind the last large wire chamber. All are constructed of 3 mm thick NE102 plastic coupled at each end of the scintillator to standard TRIUMF 41mm ϕ photomultiplier tubes (RCA8575) via adiabatic light guides. The scintillators are 'double-ended' for improved timing (when using meantimers) and for improved light collection, resulting in higher efficiency and better energy-loss resolution. (The top and bottom tubes on each scintillator are labelled with a '1' and '2', respectively in figure 16). The smaller set consists of two 35H X 18W cm² scintillators placed side by side, whereas the large set consists of two 70H X 18W cm² side-by-side scintillators, with a third, identical, scintillator placed behind the junction of these two. This redundant counter is used to monitor the relative efficiencies of the large scintillators, which must be equal in order not to introduce false scattering asymmetries into the data (see Section III.2.3).

There are two main advantages for placing the front scintillators behind the carbon analyzer instead of either in front of the carbon, or in front of the first wire chamber:

- most events scattered by the carbon out of the active region of the back chambers will not trigger the scintillators, and
- low energy background events (*e.g.* deuterons) will be ranged out by the carbon, again reducing background trigger rates in the front scintillators.

The chief disadvantage stems from the 'smearing out' of energy-loss and time-of-flight (TOF) resolutions in the scintillators; however, the scintillators are placed close enough to the carbon analyzer that there is little effect on the TOF resolution. In fact, TOF measurements based on these scintillators has been used by Experiment 445 with good results [32].

The second arm employs two sets of the smaller scintillators, one on each end of the cart close to the wire chambers. Unlike the polarimeter counters, these have only one photomultiplier tube per scintillator ('single-ended'). They were constructed as such for economic reasons.

V.1.2 Drift Chamber Construction

Our chambers are modified versions [33] of the Vertical Drift Chambers (VDCs) built for the TRIUMF MRS Focal Plane Polarimeter (MRS FPP) [24], which were in turn based on a LAMPF design for use on the EPICS spectrometer [29]. We employ seven small wire chambers with opening apertures of 31.5 X 31.5 cm², and four large wire chambers with 67 X 67 cm² apertures². The chambers are constructed of seven different layers: two orthogonal wire planes, three ground planes, and two cover windows, in the sequence window-ground-wire-ground-wire-ground-window. Eight-4.75mm aluminum frames separate each of these layers. Because of the uncentered chamber aperture, the chambers can only be mounted one way on the carts (see figure 18). Looking downstream, the horizontal wire plane (Y coordinate) is situated upstream of the vertical wire plane (X coordinate). Vacuum-stretched 25 μ m thick aluminized mylar ground and window planes are epoxide directly onto the aluminum frames. O-rings between each layer maintain the gas seal. The operating gas (typically 65% argon, 35% isobutane by volume, with a trace of isopropanol from a bubbler at 0°C) at a few Torr above atmospheric pressure enters each chamber via one standard $\frac{3}{8}$ " PVC connection that feeds both wire plane cavities (which are connected in series). The gases exit via two similar outlets, one from each cavity. Chamber signals are accessed through standard BNC coaxial connectors on the

²The extra large and small chamber are usually maintained at high voltage with a gas flow to facilitate their use as replacement spares during a run period.

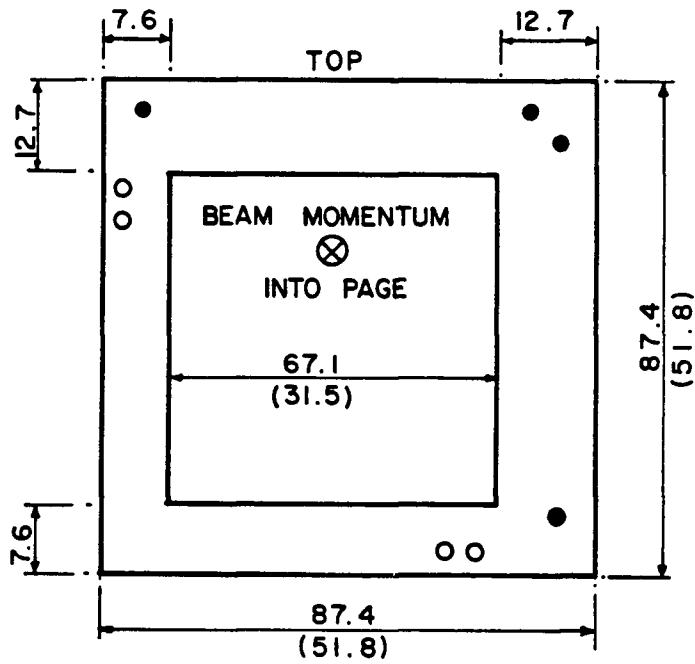
front aluminum panel. (See figure 18 and 19 for schematic diagrams of our drift chambers with important external dimensions and signal labelling scheme).

Each wire plane consists of a series of alternating anode and cathode wires separated with a constant 4.064mm spacing. The small chambers have 38 anode and 39 cathode wires, whereas the large chambers have 82 anode and 83 cathode wires [33]. Parallel ground planes situated 4.75mm from the wire planes complete the drift cell geometry shown in figure 20. The outermost anode wire on either end of each plane is substantially thicker than the normal anodes, resulting in a drastically reduced 'gas gain', These wires are effectively 'dead', but they are still held at high voltage to maintain the electric field symmetry for the outermost drift cells. The remaining 36 and 80 'live' anode wires for the small and large chambers define active apertures of 29.3 X 29.3 cm² and 65.0 X 65.0 cm², respectively.

The cathodes wires are constructed of 76 μ m diameter gold-plated beryllium-copper alloy. They are maintained at 95g tension, alternately soldered onto separate **ODD** and **EVEN** busses, with the ODD cathode wire being the outermost 'live' cathode on each wire plane. Slight capacitive couplings of the bus to the surrounding aluminum frame induce approximately 10 nsec and 20 nsec signal delays (full length) for the cathode busses on the small and large chambers, respectively.

The anode wires are constructed of 20 μ m diameter gold-plated tungsten wire. Each wire is soldered directly onto the delay-line and maintained at 51g tension. The delay line is constructed from a $\frac{1}{32}$ " thick Teflon laminate with copper coating on both sides. The zig-zag shaped copper signal path provides nominal signal delays of ~ 4 nsec per anode wire-spacing³, and has a characteristic impedance of about 90 Ω . Left and right (or down and up, respectively) ends of

³True 'effective' signal delays depend on the shape of the signal pulses, (and therefore on the length of the delay-line that the signal travels) and on the adjustments of the constant-fraction discriminators used for triggering.



ALL UNITS IN CENTIMETERS

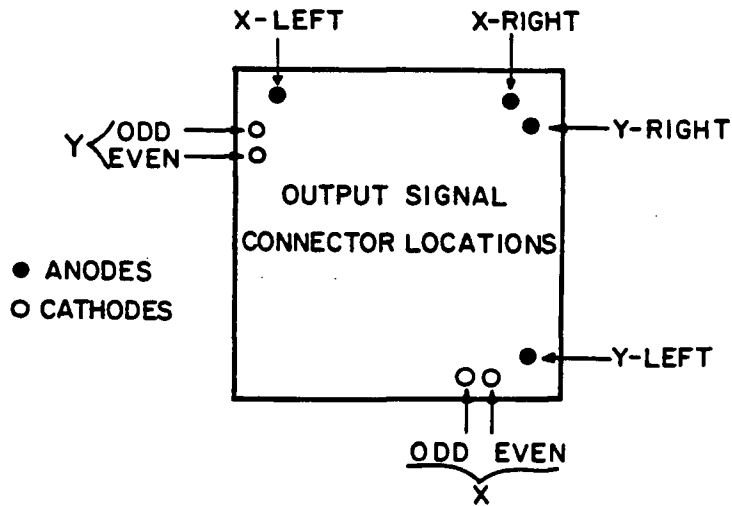


Figure 18: External dimensions of the wire chambers. The values in brackets correspond to dimensions of the small chambers where they differ from the large ones.

Figure 19: Labelling scheme for the wire chamber signals. Note that the anode high voltage enters through one of the anode signal lines. Not shown are additional ODD and EVEN bus outputs which are connected externally to 50Ω terminators.

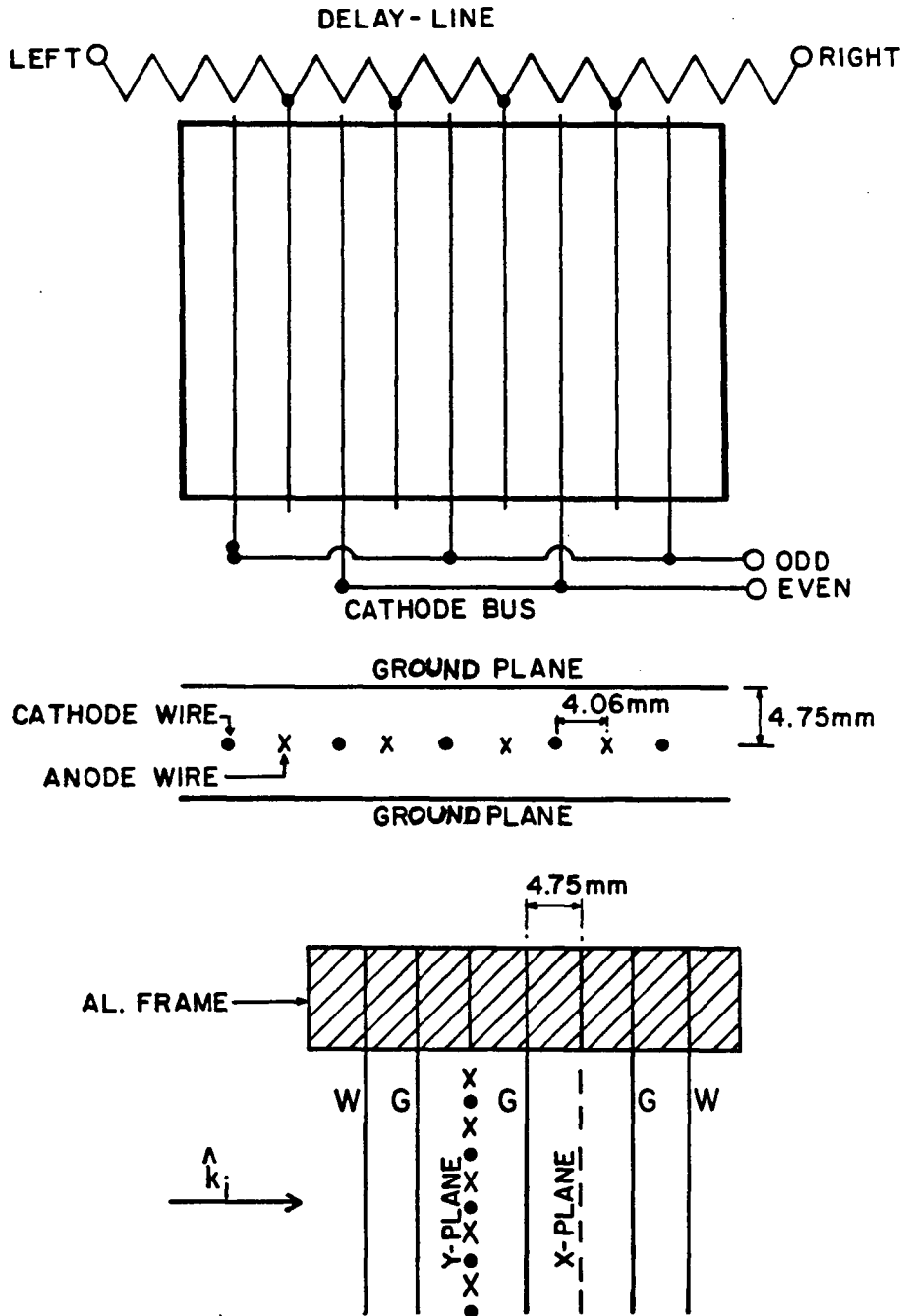


Figure 20: Three orthographic views of one of our wire planes, looking downstream, from the top, and then edge on, showing all important dimensions. Not shown are the outermost anode and cathode wires, which are used to maintain the edge fields.

| | <i>SMALL W.C.</i> | <i>LARGE W.C.</i> |
|-----------------------|---------------------------|--------------------|
| active aperture | 29.3 cm ² | 65 cm ² |
| no. anode wires | 36 | 80 |
| anode-cathode spacing | 4.064 mm | |
| anode delay-line | ~ 4 nsec/anode wire space | |
| cathode bus delay | ~ 10 nsec | ~ 20 nsec |
| operating voltage | + 2150 V | |
| reverse-bias voltage | ~ -1600V | |

Table I: Summary of some important wire chamber data.

the delay-line (looking downstream as in figure 18) connect to the so-called **LEFT** and **RIGHT** anode channels. A schematic diagram of a wire plane is shown in figure 20. Refer to table I for a summary of some important wire chamber data.

Improvements over the MRS FPP chambers

Some of the differences between our chambers and those of the MRS FPP deserve special mention. Firstly, triggering electronics, like constant-fraction discriminators (**CFDs**), perform best when input pulses are constant in shape and amplitude. **CFDs** compensate for varying amplitudes very well, and to some extent can be made insensitive to a range of risetimes [26], such as those encountered in delay-lines due to their dispersive nature. However, it has been pointed out [34] that anode pulses that do not travel appreciable lengths of delay-line are too fast to be triggered adequately with discriminators optimized for ‘average’ pulse shapes occurring in the chamber. This condition exists in the MRS VDCs [34], where some edge anode wires can not be resolved. This effect has been corrected in our chambers by adding a few centimeters of extra delay-line beyond the last anode wire connection on either end in order to slow down the very fastest edge pulses. As a result, all active wires can be resolved on both our large and small chambers.

Secondly, to precisely space the anode and cathode wires, grooves are milled into an epoxy layer recessed into the aluminum frames so that the wires remain

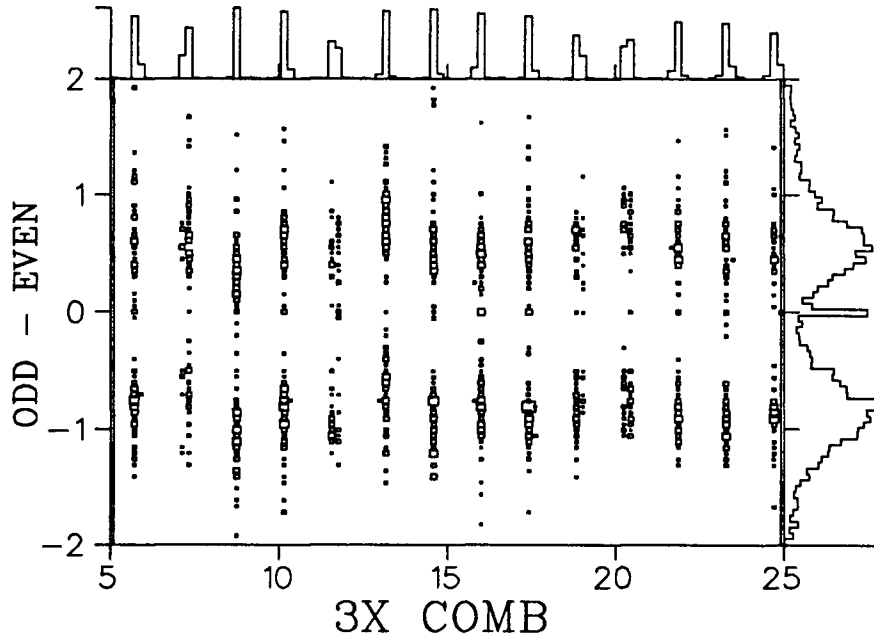


Figure 21: Cathode analog ODD-EVEN difference versus COMB anode wire position. Note the absence of ‘staggered’ combs as observed in Henderson, *et al.* [24]

secure and centered. However, it has been shown in [24] that small ($\sim 50 \mu\text{m}$) anode wire centering errors in the MRS FPP chambers led to pronounced shifts in the magnitudes of the induced pulses on the adjacent cathode wires. If left uncorrected, this in turn lead to poor resolution of the left/right ambiguity. One possible cause of this was their use of ‘flat-bottomed’ grooves, which did not adequately secure the very thin ($25 \mu\text{m}$) anode wires from any movement. Consequently, the grooves in our chambers were cut in ‘V’ shapes in order to minimize any such movement by the anode wires. This more precise wire alignment has significantly reduced the kind of systematic anode wire shifts observed by Henderson, *et al.* [24] (see figure 21).

Chamber Preamplifiers

Pulse signals arriving at each anode delay-line and cathode bus outputs are fed directly into their respective external anode and cathode preamplifiers (‘preamps’)

attached to the chamber frame. Both of these preamps are based on proprietary TRIUMF designs [35]. Their characteristics are summarized in Appendix A. Tests showed that this amplifier worked as effectively for our needs as the EG&G VT110 preamps used by the TRIUMF MRS FPP group [24] at a much lower cost per amplifier.

The cathode preamplifiers are used mainly to amplify the cathode pulse signals for input into the charge-integrating analog-to-digital converters (ADCs). Apart from some minor modifications, our cathode preamps are identical to the TRIUMF-built units used by the MRS FPP group in their drift chambers. The lack of any gas gain from the relatively thick cathode wires (roughly 3X the anode wire diameter) and the small (maximum $\sim 10\%$) differences between the ODD and EVEN cathode pulses require linear, high gain preamplifiers for optimal resolution of the left-right ambiguity (see Section IV.1.3). The cathode pulses have slower (~ 25 nsec) risetimes than the anode signals, and therefore are less suitable for precise drift timing. However, every ODD signal is timed through a CFD to record the drift-time as seen by the cathodes for use in calculating the chamber CHECKSUM (see Section IV.2.4).

Refer to Appendix A for schematic diagrams of our anode preamplifiers.

V.2 DATA ACQUISITION

This section presents details of the computer and nucleonics system used with our polarimeter. Elements specific to a particular experimental arrangement are introduced only where they help explain the operation of the polarimeter system in general. For a presentation on the data acquisition software used by Experiment 331, refer to [10].

V.2.1 Scintillator Signals and Event Trigger

The polarimeter scintillators are mainly used for event triggering. Employing the scintillator labelling shown in figure 16, the coincidence event trigger (**START**) can be described by the following logic equations:

$$S_{xA} = S_{xA1} \cdot S_{xA2}, x \in (1, 2, 3, 4, 5) \quad (36)$$

$$START = (S_{1A} + S_{2A}) \cdot (S_{3A} + S_{4A} + S_{5A}) \quad (37)$$

As indicated in figure 22, the pulses from the top and bottom phototubes on each scintillator are fed through constant-fraction-discriminators to LeCroy 624 **meantimers**. The CFDs use 4 nsec external delays for precise timing. Meantimers are coincidence units whose output pulse timing is independent of the position in the scintillator traversed by the incident particle. These two elements combine to give a virtually ‘jitter-free’ event timing for each scintillator. Refer to figure 16 for a schematic diagram showing scintillator placement on the polarimeter.

In Experiment 331, the front scintillators ($S_{1A}+S_{2A}$) were used to define the timing of the **START** pulse since their proximity to the carbon minimized the timing jitter due to the variable particle energy-loss [10]. However, a problem can arise if these two scintillators are not precisely timed with respect to each other. These signals enter into the trigger via an OR, so the **START** pulse timing is dependent on which of the two front scintillators detected the passing particle. Since each scintillator covers (roughly) half of the incoming trajectories, particles passing through one side of the polarimeter wire chambers can experience a different timing prompt than the other side. This is illustrated in figure 23, where events occurring on the left side of this chamber (and passing through one front scintillator) are observed to start later than events passing through the other side. This can be a significant problem if not taken into account.

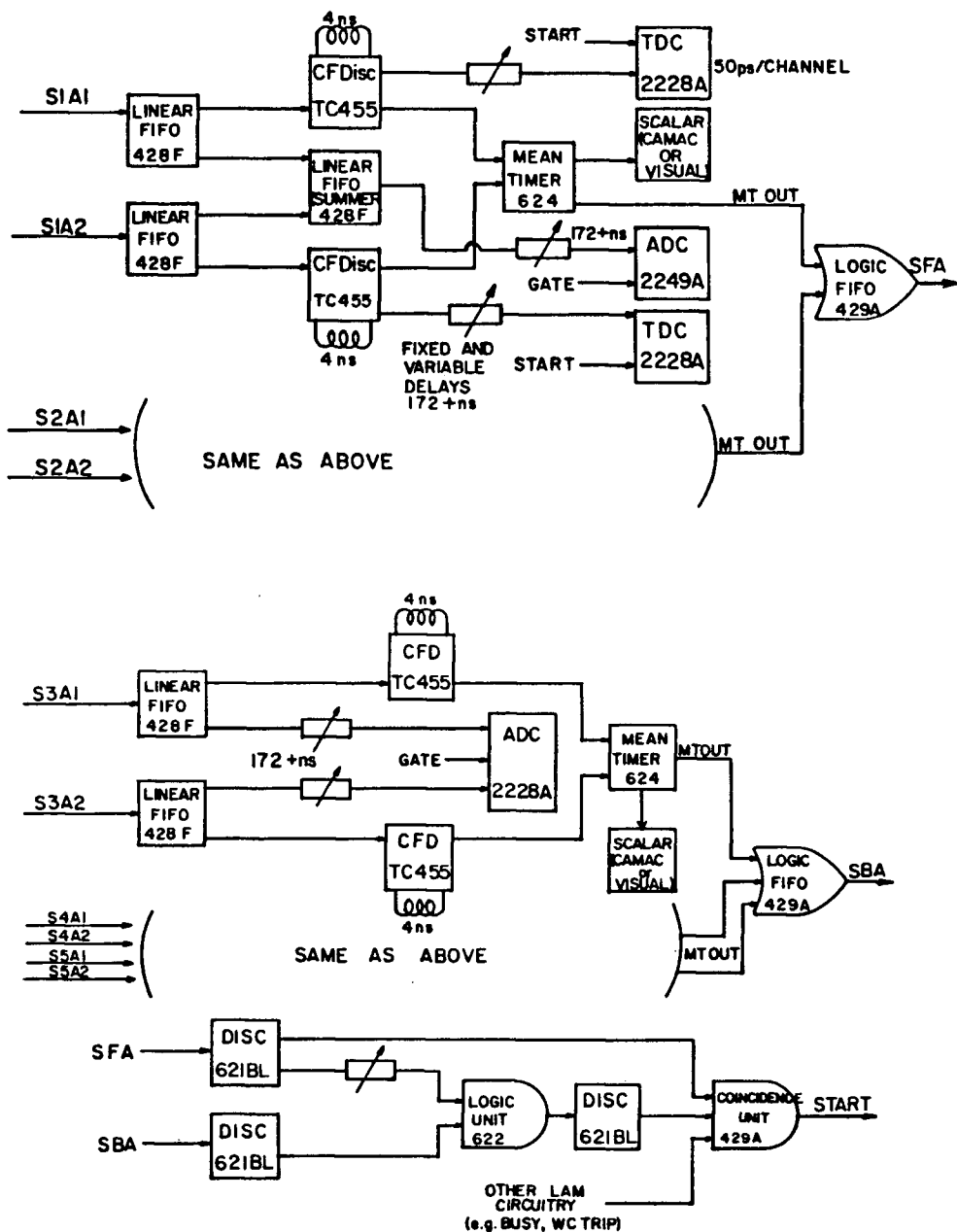


Figure 22: Schematic diagram of event trigger logic. Not shown is the time-of-flight (TOF) counter circuit, which enters this logic at the final coincidence. All unit labels (except the Tennelec TC455 CFD) refer to LeCroy model numbers.

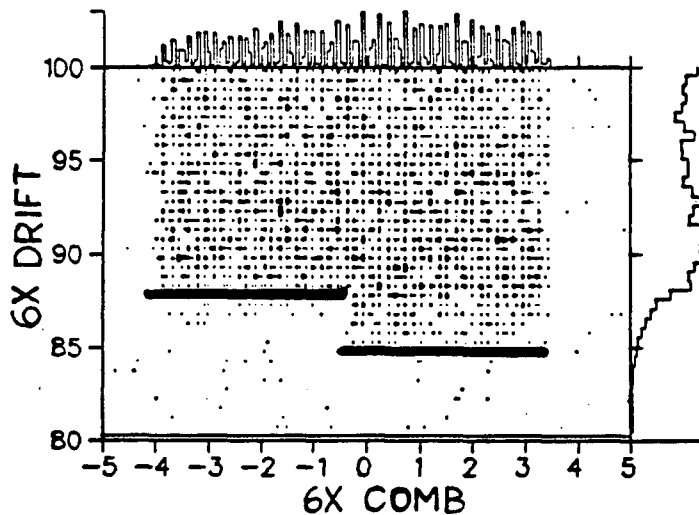


Figure 23: Figure shows how START timing jitter affects the DRIFT timing. The leading edge of the drift-time spectrum differs on one half of the chamber from the other since the two START-defining front scintillators which shadow this chamber are not well timed with respect to each other.

For some applications, one can also include in the timing coincidence a single thin, double-ended counter positioned in front of the polarimeter and close to the target. This scintillator can better define the beginning of the START pulse since its timing is not affected by the carbon scattering and its relatively small size provides for very fast pulses. Also, time-of-flight between this counter and the front scintillators can be used for particle identification purposes. Such an arrangement was employed in Experiment 445 [11].

The scintillators also provide two different levels of (prompt) background subtraction. Setting the CFD thresholds to discriminate against lowly-ionizing particles like pions and muons, and insisting on a coincidence between the front and rear scintillator groups significantly reduces the the background triggering rate in 'noisy' areas like pion channels.

Our second arm event trigger follows basically the same logic as the

polarimeter. In two-arm experiments like E331, the overall event definition involves a coincidence between the second arm prompt (defined by the coincidence of its front and back scintillator groups) and the polarimeter trigger. Logic is arranged so that the overall timing is defined by S1A+S2A. The second arm scintillators have only one phototube, so the more precise timing of the polarimeter is used to define the overall START prompt.

V.2.2 Wire Chamber Electronics

The two experiments that used the polarimeter to date have employed standard NIM-type nuclear electronics (nucleonics) for the hardware signal processing and logic. Two standard CAMAC modules interfaced these signals to the data acquisition computer. Refer to figure 24 for a schematic diagram of a typical wire chamber readout circuit.

The polarimeter event trigger described above defines the Look-at-Me (LAM) pulse for the CAMAC interface, the START pulse for the time-to-digital converters (TDCs), and the gates for the ADCs. In addition to providing a pulse for event timing, each scintillator phototube signal gets fanned-out and passed directly through an attenuator to an integrating analogue-to-digital converter (ADC) for $\frac{dE}{dx}$ particle identification. Recording the pulse sizes from both scintillator photomultiplier tubes allows for offline correction of tube gain and offset mismatches. On the other hand, if the tubes are well matched, the signals can be summed in hardware thus reducing some circuit complexity⁴.

In order to obtain time-of-flight information for better particle identification, the timing of each scintillator can be recorded by fanning-out each logic signal into a TDC. Because of the carbon, this only works adequately with the second arm

⁴In Experiment 331 [10], the signals were hardware summed in the front scintillators to reduce the number of ADC channels and attenuators required. See figure 22.

counters (see Section VI.1) or with the polarimeter front scintillators when a TOF-counter is used before the polarimeter to define the START.

Each wire chamber delivers five signals to the CAMAC system: three TDC STOPS corresponding to the LEFT and RIGHT anode delay-line signals and the one ODD cathode pulse, and two analog signals for ADC input corresponding to the ODD and EVEN cathode bus outputs (see figure 23). The LeCroy 2228A TDCs used were set at 250ps/channel (500 nsec full scale) to accommodate the anode delay-line.⁵ The operation and setup of these circuits along with the critical CFD and ADC components have been studied in some detail and will be discussed in the following sections.

Constant Fraction Discriminators and Wire Chamber Timing

Extensive 'table-top' testing prior to the first data runs showed that constant-fraction-discriminators provided much better timing than either risetime-compensated or threshold discriminators. CFDs are designed to work best with input signals of fixed shape irrespective of the pulse amplitude. The ODD cathode signals used to measure the DRIFT-TIME do not vary significantly in risetime. For all chambers, the CFDs discriminating these signals were found to work best with 8 nsec external delays.

For the anode signals, however, the situation is not so straightforward. Unfortunately, the dispersive anode delay-lines significantly attenuate and slow down signal pulses in proportion to the amount of delay-line traversed. With the properly chosen values of the CFD external delay, this effect on the timing can be minimized. The timing for the small chamber anode signals was found to be optimized using 8 nsec external delay. The COMB peaks show good separation

⁵At 250ps/channel, the TDC has a 0-500 nsec full scale range, whereas only 0-200 nsec is possible with 100ps/channel. Thus, a long 100 nsec drift-time event travelling the full ~ 240 nsec large chamber delay-line can only be accommodated with the TDC set at 250ps/channel.

out to the chamber edges, and the CHECKSUM distribution shows a very narrow spike shape (see figure 25). A 16 nsec external delay was chosen for the large chamber anode signals; however this value represents a compromise solution. Figure 26 shows that the large chamber COMB peaks are better resolved with 16 nsec delay, but the CHECKSUM distribution is far narrower at 8 nsec. The broad tail of the 16 nsec CHECKSUM distribution occurs predominantly for events with very short and very long drift times. This effect is not fully understood. The 16 nsec delay was chosen for the optimal COMB performance. One does not expect drastic increases in chamber inefficiencies to occur simply by changing this delay, so the events in the CHECKSUM tail are included in any analyses.⁶

Constant-fraction-discriminators (like the Tennelec TC455) have a front panel output used to monitor the time-jitter, or 'walk', performance of the unit. It was found that the timing performance as revealed by the COMB and CHECKSUM distributions did not vary significantly for small adjustments about the optimum setting. An additional peak appearing in the CHECKSUM and a total loss of peak resolution in the COMB distribution (effects apparent during online monitoring during a run) are symptoms of gross walk maladjustments. These effects are illustrated in figure 27.

Our Left/Right Resolution System

To resolve the left/right ambiguity, our system calculates the ODD-EVEN cathode signal difference in software instead of using a hardware system like that of the LAMPF [3] and Geneva [2] groups. There are two basic analog-to-digital conversion schemes that can be used to record the ODD and EVEN pulses. One method applied by the MRS FPP group [24] uses the LeCroy 2249SG ADC which

⁶In fact the leading edge to the distribution, where mainly inefficient events are found (see Section IV.2.4) does not change in shape for the various delays.

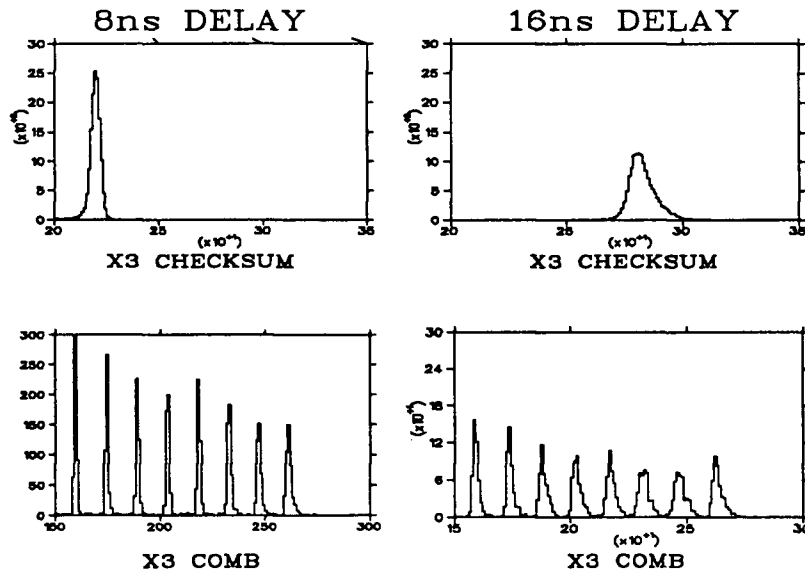


Figure 25: Comparison of small chamber COMB and CHECKSUM distribution for run using optimal 8 nsec CFD external delay on Tennelec TC455 CFD units versus run using 16 nsec external delay.

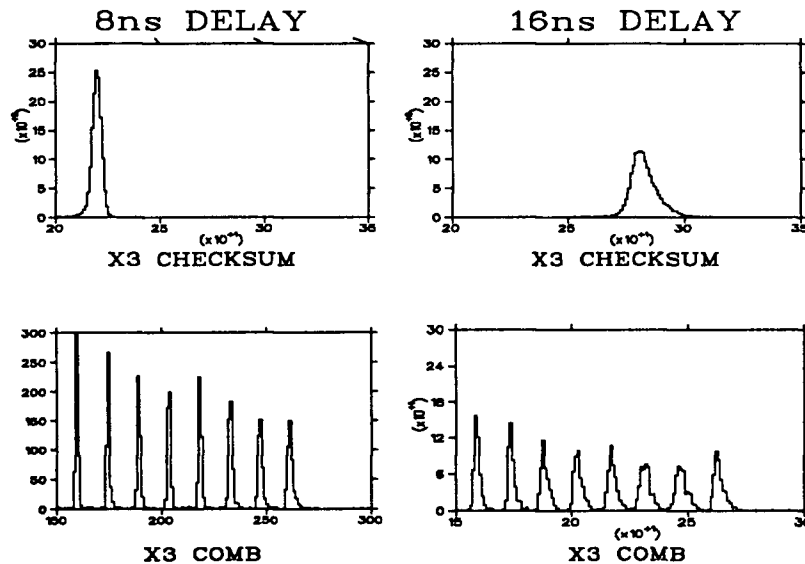


Figure 26: COMB and CHECKSUM distributions for large chambers comparing performance using 8 nsec and 16 nsec CFD external delay. Despite broad CHECKSUM distribution, 16 nsec delay was chosen for use with the large chambers.

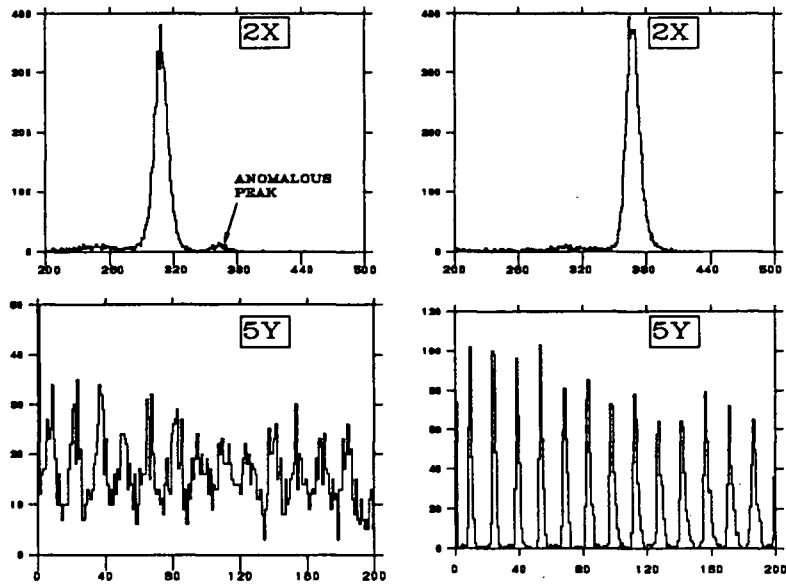


Figure 27: The left column shows (from top) the CHECKSUM and COMB distributions with improper CFD walk adjustment; whereas the right column shows the corresponding results for proper walk adjustment.

can accommodate a separate gate for each input. Gates are generated for *each* ODD/EVEN pair with the timed ODD pulses. Smaller gate widths can be used around the peaks of the cathode pulses since the signals will not jitter within the gate, resulting in good signal-to-noise ratios. One drawback of this approach is the increased circuit complexity over that of a common-gate ADC system. Refer to Henderson, *et al.*, [24] for more information on this individual gate approach.

The runs employing the polarimeter to date involved systems whereby the cathode pulses were attenuated and then passed directly to LeCroy 2249A ADC modules. This strategy minimizes the circuit complexity since all ADC inputs have a common gate generated by the system LAM. A typically 160 nsec wide gate is necessary to accommodate the cathode time jitter due to the variable drift times which range up to ~ 100 ns. However, several tests performed subsequent to the major experiments have shown that systems using a single common ADC gate should use the LeCroy 2249W ADC, which has a 11 bit conversion range, instead

of the 10 bit range in the 2249A. It turns out that the the broad range of cathode pulse sizes cannot be adequately accommodated by the 2249A, resulting in significant overflows which cannot be entirely eliminated without excessive signal attenuation. Unfortunately, ODD-EVEN resolution deteriorates with increased attenuation since the signal-to-quantization noise ratio decreases. The larger dynamic range of the 2249W ADC permits smaller attenuations with fewer overflows, resulting in improved ODD-EVEN resolution and increased efficiency. See Section VII.1.2 for some efficiency and resolution results.

When using the common gate system, one must ensure that leading edges of both cathode pulses are not 'clipped' by the applied gates. Early (short drift time) events are predominantly small pulses since chamber ionizations occurring within the avalanche region around the anode wire will not accumulate as much gas gain as events occurring outside this region. These signals can be 'masked' by the larger pulses in the oscilloscope display when the cathode signals are being timed in and so the leading edge of the pulse might be cut out inadvertently by a poorly set gate. This leads to a complete loss of ODD-EVEN resolution at the short drift time region, as can be seen in figure 28. This figure was generated from data taken during an Experiment 331 run, where it is believed that the above scenario transpired with the ODD signals.

V.2.3 Small-Angle Scattering Event Preprocessing

The CES J11 STARBURST preprocessor was chosen to realize the online small-angle scattering rejection in the carbon. The preprocessor can apply tests to various quantities calculated from CAMAC inputs using user supplied macro-coded routines, and subsequently instruct the host computer to read or discard the CAMAC event buffer based on the test results. Using just the

chamber coordinates provided by the anode COMBs in chambers 1,3,4,and 6, Feltham [10] described how the preprocessor was used to reject events with carbon analyzer scattering less than some specified angle in either of the x or y chamber planes. This results in a ‘square’ cut in a plot of the angular distribution of events in a post-carbon chamber. More recent runs have employed a circular cut where the polar scattering angle is calculated using the small-angle approximation

$$\theta^2 \approx \theta_x^2 + \theta_y^2 \quad (38)$$

where $\theta_{x,y} \approx \tan(\theta_{x,y})$ are the scattering angles in the x or y coordinate planes. Examples of such plots are illustrated in figure 29. A circular cut was implemented since it was realized it eliminates coulomb scattering events more efficiently than a box cut.

V.2.4 Online Diagnostics

During the setup and running of the polarimeter system, a number of online diagnostics were found to be very helpful in monitoring the performance of the chambers. These are listed below:

- **CHECKSUM:** Since the CHECKSUM combines the LEFT, RIGHT, and ODD timing signals in one distribution, one can easily identify a serious problem in any one of these three elements if the distribution does not exhibit its customary tightly peaked shape.
- **COMB:** The COMBS are a sensitive measure of the timing performance of the LEFT and RIGHT circuits. As shown in figures 25, 26, and 27, they can be used to precisely set up the timing CFDs.
- **ODD vs. EVEN:** A plot of the ODD versus the EVEN cathode ADC signals show whether or not this system is functioning properly without the

need for calibrating relative gains and offsets. Good separation between the two bands in these plots indicates proper setup. Poor separation can be a result of excessive ADC attenuation, or improperly set chamber high voltages. (see Section VII.1.2)

- **Small-Angle Cut:** The small-angle cut needs to be monitored to ensure that the cut has been centered properly about 0 degrees. An improperly centered small-angle cut will introduce artificial asymmetries. In such cases, the cut will need to be enlarged into a centered cut during offline analysis, consequently reducing the counting statistics.

Refer to Feltham [10] for an account of the calibrations that need to be carried out online to view these diagnostic spectra.

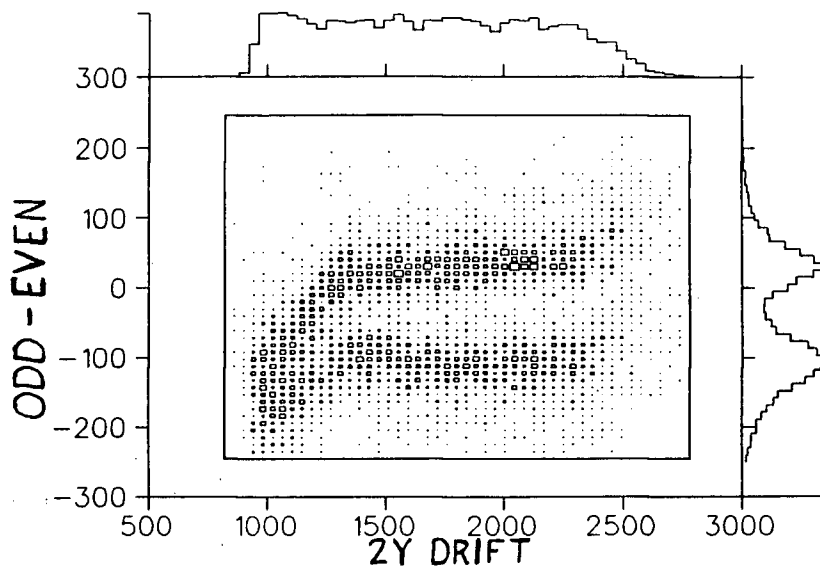


Figure 28: Clipping one cathode signal with the common ADC gate causes a complete breakdown of ODD-EVEN resolution at short drift-times as the dip in the above plot clearly demonstrates.

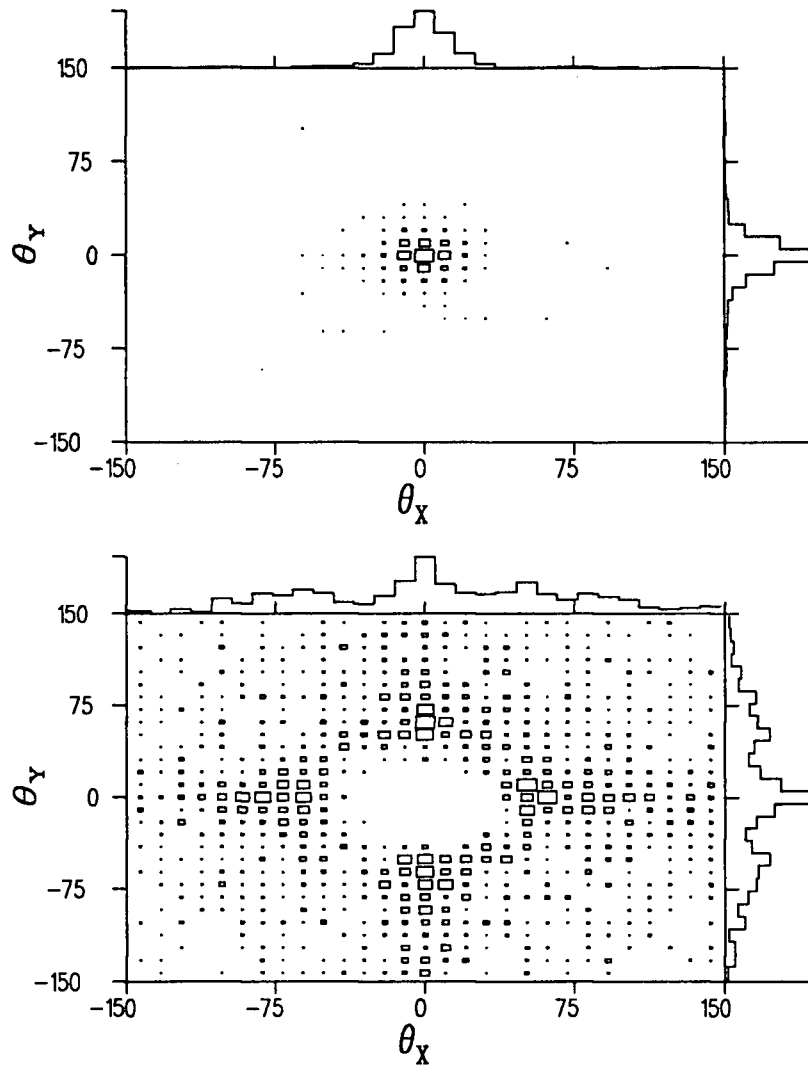


Figure 29: Top figure shows carbon scattering distribution without small-angle pre-processing, whereas the bottom figure shows distribution with circular small-angle rejection using the J11 preprocessor.

Chapter VI

Polarimeter Calibration

This chapter presents briefly the techniques used in the wire chamber position calibrations. The procedures outlined here follow those used during Experiment 331 run calibrations. Where appropriate, alternate methods will also be presented for some the procedures. References will be made to the polarimeter wire chambers, although most of these techniques can be applied directly to the second arm.

VI.1 PARTICLE IDENTIFICATION

The energy-loss information from the scintillator pulse-heights ($\frac{dE}{dX}$) are used to identify candidate proton events in the polarimeter. In pion scattering experiments there will invariably be a large flux of elastically scattered pions incident on the polarimeter. By adjusting the thresholds of the scintillator CFDs to discriminate against these lowly-ionizing pions, background count rates can be significantly reduced, thus allowing for reasonable separation of the pion and proton peaks in the energy-loss spectra as illustrated in figure 30. Cuts (like the example shown in figure 30) on all the polarimeter and second arm scintillator energy-loss spectra were sufficient to identify proton events in Experiment 331¹.

¹Recall from Section V.1.1 that highly ionizing particles, like deuterons, are ranged out by the

In the two arm coincidence setup, one can obtain better background subtraction by using the scintillator timing information in the back arm². Each second arm scintillator employs only a single photomultiplier tube, which results in significant timing jitter dependent on the particle's interaction point in the scintillator. One can correct for the timing jitter by estimating the event position in the paddle using the nearest wire chamber y-plane. Figure 31 shows the correlation between scintillator S3B timing and chamber 9Y (raw) COMB position for the particular case where 2-body correlated protons were detected in coincidence with the polarimeter. Figure 32 shows the scintillator TOF versus $\frac{dE}{dX}$ plots before and after implementing said corrections. Note the resultant improvement in the separation of the 2-body events from the background. The polarimeter scintillators are double-ended and do not require such corrections when using meantimers to define the timing. However, a TOF trigger counter must be used to define the system START if time-of-flight information is desired from the polarimeter scintillators (see Section V.2.1). Refer to [11] for a discussion of how the polarimeter scintillator TOF information is used to determine proton energies in Experiment 445.

VI.2 WIRE CHAMBER POSITION CALIBRATION

The wire chamber position calibrations proceed using the subset of candidate proton events defined by the scintillator cuts. Each of the quantities necessary to determine the chamber positions (see Section IV.2.3) are calibrated in sequence as outlined in the following sections.

carbon analyzer before triggering the front scintillators. *e.g.* 5 cm of carbon can stop 125 MeV deuterons.

²The slower backward protons detected in the second arm provide greater flight times and hence better TOF separation than the forward arm.

VI.2.1 SUMTIME and drift distance

A calibrated SUMTIME distribution is required for the both the position and CHECKSUM definitions, so it must be handled first. The offsets and widths (gains) of all SUMTIME spectra are fixed to some reference value so that only a single cut range and SUMTIME-to-drift distance conversion table is required for all wire chambers. These gain and offset differences arise from imperfectly matched TDCs and signal path lengths. Additional *variable* offset adjustments may be required to compensate for the differences in the velocities of incident protons³. Such adjustments were found to be needed in E445 [37], but not in E331 [31]. (An extreme example these kinds of shifts is illustrated in figure 33 where 390 $\frac{MeV}{c}$ pions and protons directly out of the TRIUMF M11 beam pipe were detected by the polarimeter with the carbon removed). Also, as previously mentioned in Section V.2.1, an additional correction may be necessary if significant timing jitter arises from improperly timed front polarimeter scintillators used to define the START (see figure 23).

Once the corrections have been made to the SUMTIME spectra of each chamber, all the distributions are summed together to realize an ‘average’ overall SUMTIME spectrum. This average spectrum is subsequently integrated and normalized to determine a SUMTIME-to-drift distance relationship appropriate for all the wire chambers (refer to Section IV.1.2), resulting in the spectra shown in figures 34 and 35. The (SUMTIME, drift length) pairs represented by figure 35 are then written to an external file. This file is used as a ‘look-up table’, whereby a program can determine the drift-distance corresponding to a particular SUMTIME simply by looking-up the SUMTIME value in the file.

³Recall from Section IV.1.2 that the SUMTIMES are defined with respect to some system prompt.

VI.2.2 CHECKSUMs

A fitting method is employed to determine the offset and gain constants (g_1 , g_2 , and K_{cs}) used to calculate the CHECKSUMs (refer to Section IV.2.4). Unmatched TDC gain constants for the anode and cathode timing signals will cause the gain constants to vary between chambers. In practise, the chamber raw COMB values are used to correct for cathode bus delay, instead of wire numbers, since this removes the need for a prior discrete COMB calibration (see following section). First, the constants g_1 and K_{cs} are determined by a fit to the ODDTIME versus SUMTIME distribution (see figure 36). With these fitted parameters subsequently fixed, the constant g_2 is then fit to the SUMTIME - $g_1 \cdot \text{ODDTIME}$ versus COMB relationship. Tight box cuts are placed around the distribution bands in the above plots to ensure good fits. ‘Good event’ cuts are then defined for the resulting calibrated CHECKSUMs as shown in figure 37. (Cuts are better determined using logarithmic scales since they exaggerate the detail at the tails where the cuts need to be placed). Calibrated in this way, the resulting constants and cuts have been observed to be insensitive to changes in wire chamber operating conditions (*e.g.* particle energy-loss, chamber voltage).

VI.2.3 COMBs

The COMB calibration takes the (continuous) raw anode RIGHT-LEFT TDC difference distribution (shown in figure 12, Section IV.2.3) and converts it into a spectrum of discrete peak positions corresponding to the anode wire positions. This spectrum is known as the **discrete COMB** spectrum (an example of which appears in figure 38), and is defined by

$$DCOMB = \text{nint} \left(\frac{x}{w} \right) \cdot w \quad (39)$$

where x is the **continuous** COMB spectrum given by

$$x = c_0 + c_1 t_{diff} + c_2 t_{diff}^2 + c_3 t_{diff}^3 \quad (40)$$

calibrated to give a peak every $w = 8.128$ mm, corresponding to the anode wire spacing. The higher order terms in x are included to compensate any delay-line non-linearities that may exist (see Section IV.2.3).

There are two ways that the calibration constants c_i can be determined. One method involves a straightforward fit to the COMB peaks positions [38], whereas the other method involves a more complicated fit that minimizes the difference between the continuous and discrete COMB positions through the χ^2 distribution

$$\chi^2 = \frac{1}{\sigma^2} \sum (x - DCOMB)^2 \quad (41)$$

Here σ represents the half-width of a typical COMB peak. Originally the E331 COMB calibration analysis proceeded via the latter technique; however it has recently been replaced by a peak fitting program written by R. Deary [38] which has proven to be much faster.

Figure 39 shows how the COMB peak positions are fit very well by a straight line, even out to the edges of a large chamber. For this reason, no terms higher than linear have been employed in any of our calibrations.

VI.2.4 Resolving Left/Right Ambiguity

In order to complete the individual chamber calibrations, the left/right ambiguity remains to be resolved (refer to Section IV.2.3). There are two possible ways to determine which of the ODD or EVEN cathodes sensed the largest signal and hence determine which cathode was closer to the primary ionizations. The most straightforward approach merely determines the *sign* of the normalized

ODD-EVEN difference. This method necessitates matching the gains and offsets of the ODD and EVEN ADC spectra. One possible correction scheme is as follows:

$$E_{odd} = E_{odd}^{raw} - K_{odd} \quad (42)$$

$$E_{even} = g \cdot (E_{even}^{raw} - K_{even}) \quad (43)$$

where the normalized difference is defined as (see Section IV.1.3)

$$O - E \equiv \frac{E_{odd} - E_{even}}{E_{odd} + E_{even}} \quad (44)$$

The constant g represents the relative gain between the total ODD and EVEN electronic pathways (preamplifiers, attenuators, ADCs) and the constants $K_{odd,even}$ represent the respective offsets. Individual ADC offset and relative gain corrections are made in software using the approach illustrated in figure 40, where the raw ODD and EVEN ADC spectra are plotted against each other. The relative ODD versus EVEN gain is given by the slope to the bisector of the lines fitting the two bands of points. The projections of the intersection of the two fitted lines onto each axis give the corresponding ODD and EVEN offsets. This has been the technique employed in the E331 analysis [31]. An example of a normalized ODD-EVEN spectrum appears in figure 14 in Section IV.1.3.

Figure 40 also suggests another possible method to determine the sign of the ODD-EVEN difference. Note that an event registering a larger ODD pulse than EVEN pulse will lie in the band of points *above* the bisector line; whereas the converse is true for a larger EVEN pulse. If one determines the equation of the bisector line, say

$$B = a_0 + a_1 * E_{even} \quad (45)$$

one can then determine the sign of ODD-EVEN by calculating whether B is larger or smaller than E_{odd} for a given E_{even} . This method has the advantage that no gain or offset matching is required, thereby simplifying the calibration procedure.

Also, the choice of bisector is not as critical as the proper choices of band line fits needed for the other procedure, where even small changes in the slopes of these lines can cause significant changes in the calculated gains and offsets.

One more problem needs to be overcome before completing individual wire chamber position calibrations. As was mentioned in Section IV.1.3, one still needs to know *absolutely* which anode wire in the chamber registered an event in order to determine whether the drift distance associated with, say, an ‘ODD-side’ signal needs to be added or subtracted to the corresponding discrete anode wire position. In our wire chambers, the ODD cathode wire is the outermost active wire in each plane (see Section V.1.2). With anode wires labelled -18,...,18 (small w.c.) and -40,...,40 (large w.c.), the ODD cathode wire is seen to be on the *left* of the even numbered anode wires (looking downstream). Unfortunately, apart from chamber 3, the wire chambers are not fully illuminated by the incident beam⁴ so one cannot determine the absolute wire numbers using the observed COMB spectra alone. Ransome [14] showed that one can determine the proper cathode/wire number relationships, or **odd/even phases**, by first assuming some phase (*e.g.* ODD wires on the right of even numbered anode wires) for the chambers which were not fully illuminated, and then plotting the resulting x (or y) position of one chamber plane versus another. Figure 41 shows the three possible outcomes of such a plot. Generally the incident protons do not cross the chambers normal to the wire planes, so even if both chambers are out of phase, this plot shows the resulting parallax error as a series of parallel diagonal lines. One can eventually arrive at the correct phases for all the polarimeter chambers by comparing them in this way to chamber 3, which is normally fully illuminated so that its absolute wire numbers can be determined directly from the observed COMBs.

⁴Wire chamber 3 is in front of and smaller than the front polarimeter scintillators, so its active area defines the incident acceptance of the polarimeter.

VI.3 CHAMBER ALIGNMENT

Once all the individual chamber positions have been calibrated, the relative inter-chamber position offsets must be determined so that the origins coincide for some reference particle trajectory defined in the lab frame. Ideally, the data should be from special calibration runs where the polarimeter carbon was removed and a very small 'finger' scintillator positioned in front of the polarimeter is inserted into the system trigger to define a narrow beam of trajectories down the center of the wire chambers at some specified lab angle. The chamber offsets are then defined with respect to chamber 3, since its coordinates are known absolutely with respect to the lab frame from the previous calibrations with fully illuminated active areas. The offsets are determined by again plotting the x (or y) coordinate of each chamber against the x (or y) coordinate of chamber 3, and adjusting the chamber offsets until the diagonal band crosses the origin (see figure 42). This procedure can also be used to determine the absolute calibration of the second arm chambers by using a run where the 2-body correlated protons from the $\pi + d \rightarrow p + p$ reaction are detected in coincidence with the polarimeter. A similar, although broadened band, appears for the chamber 7 versus chamber 3 plots, from which the offset is determined as usual. The other chambers in the second arm are then offset relative to chamber 7 in the same way.

The calibrations can be checked by calculating the difference in the position registered by the middle chamber in each tracking group and the extrapolated position at that chamber using the end chambers in the group as trajectory-defining endpoints. *i.e.*

$$\Delta x = x_2 - \frac{1}{2}(x_3 + x_1) \quad (46)$$

A distribution as illustrated in figure 43 is a sensitive measure of how well the three chambers are calibrated with respect to each other, and will not be centered

on zero if all three chambers are not properly aligned ⁵.

This calibrations implicitly assume that the protons emanate from a point source. This is of course not true for an extended target. After an initial round of calibrations, the chamber positions can be used to define a traceback to the target. (See Feltham [10] for algorithms to calculate target tracebacks). Then the whole calibration process can be repeated for events satisfying some tight cut around the target traceback, thus improving the point-like target approximation. The process is iterated until no further improvement in the calibrations is found.

⁵The width of this distribution is related to the intrinsic positional resolutions of the chambers. See Section VII.1.1

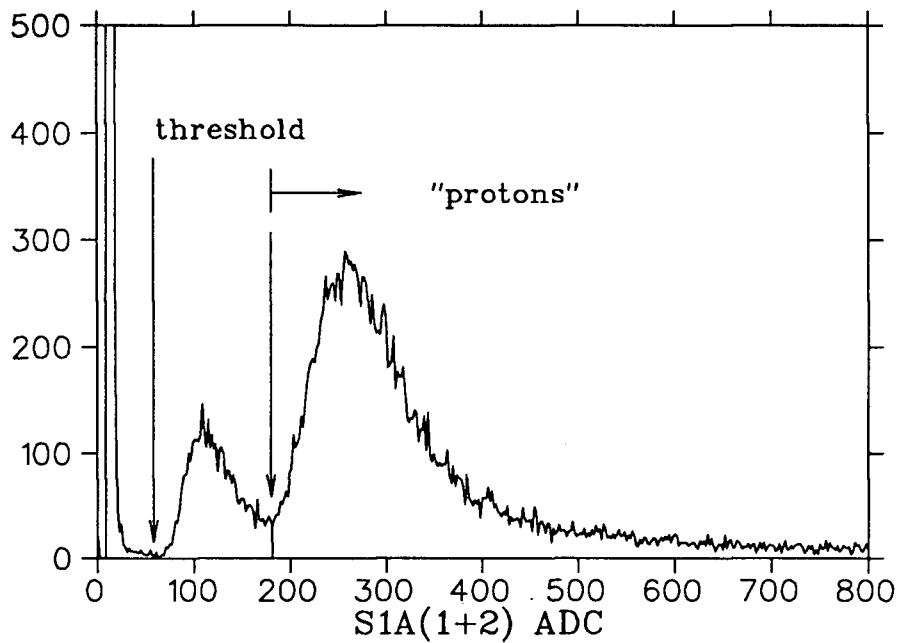


Figure 30: Spectrum of pulse-heights obtained from scintillator ADCs in a typical E331 run showing proton cut. Note that the smaller 'pion' peak has been greatly suppressed by threshold adjustment.

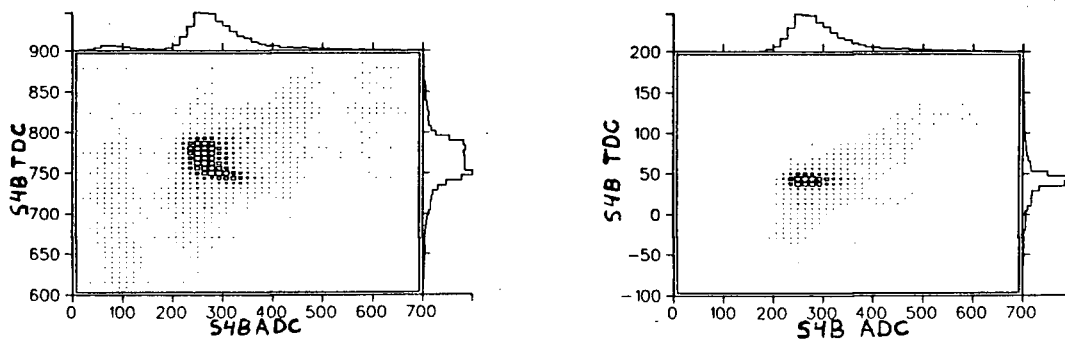
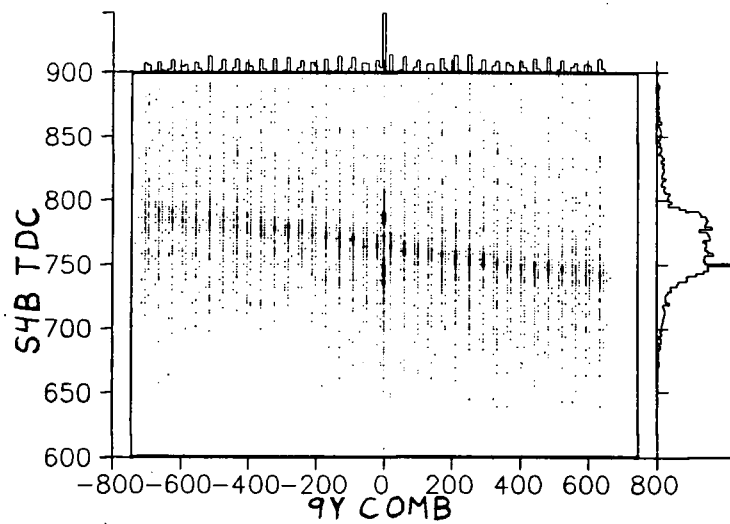


Figure 31: (top) Correlation of the S3B TOF spectrum with chamber 9y comb position.

Figure 32: (bottom) The TOF versus S3B ADC scatterplot used for proton identification, before (left), and after (right), implementing the TOF position corrections. These plots illustrate a particular case where 2-body correlated protons were detected in coincidence with the polarimeter.

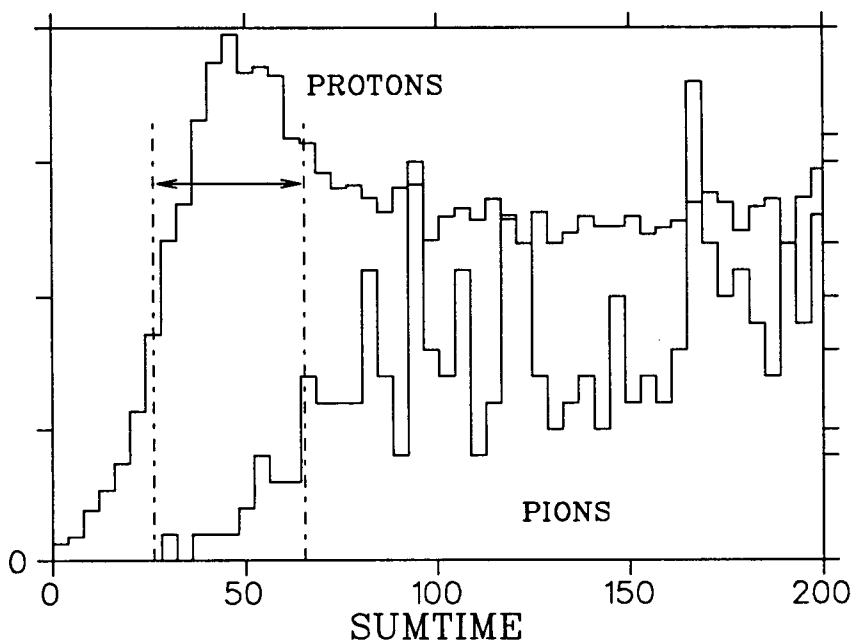


Figure 33: Differences in incident particle velocities cause shifts in the timing of chamber SUMTIMEs. Shown is an extreme example of $390 \frac{MeV}{c}$ pions and protons.

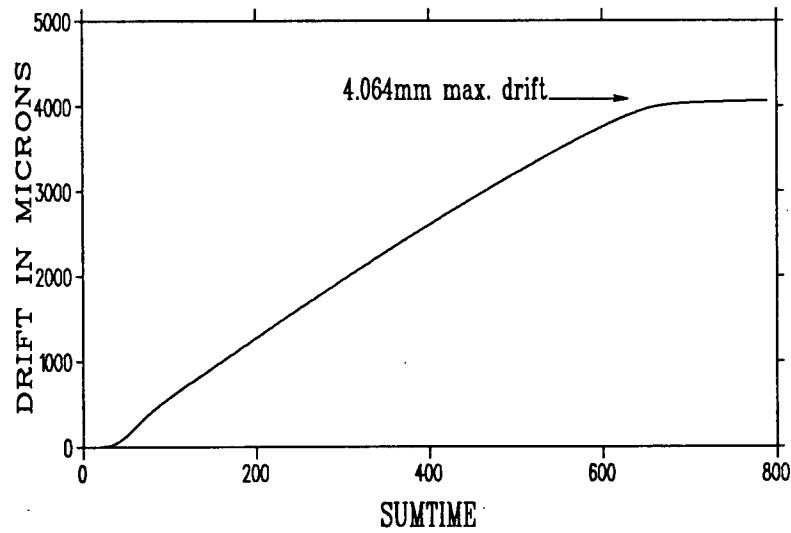
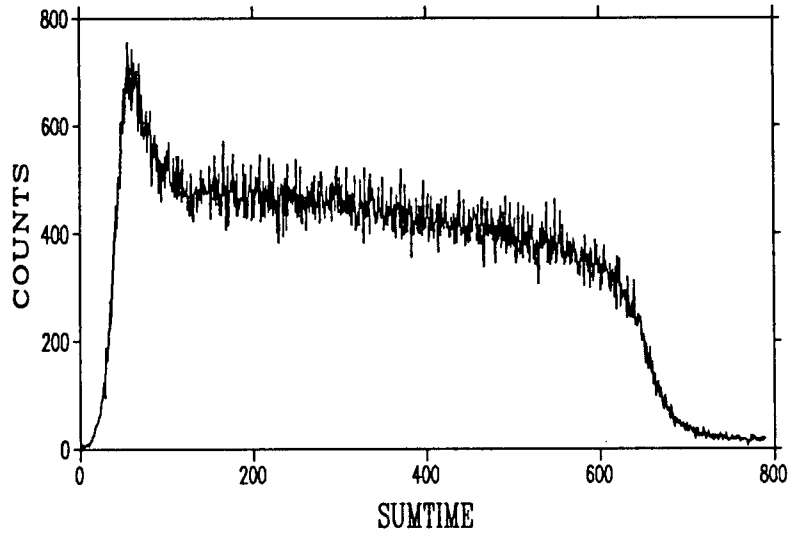


Figure 34: (top) Distribution of sum of all calibrated wire chamber SUMTIMEs.

Figure 35: (bottom) Drift-distance to SUMTIME relationship found by integrating and normalizing the top distribution. (equation 27)

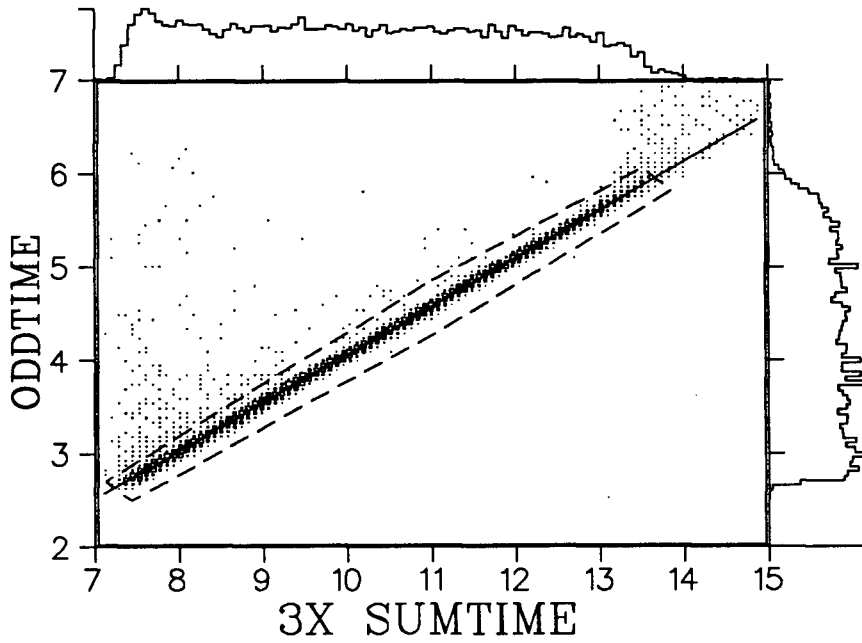


Figure 36: ODDTIME versus SUMTIME distribution used in calculating the CHECKSUM. The box cut drawn around the distribution may be required to filter out events around the main band which can hamper the fitting procedure.

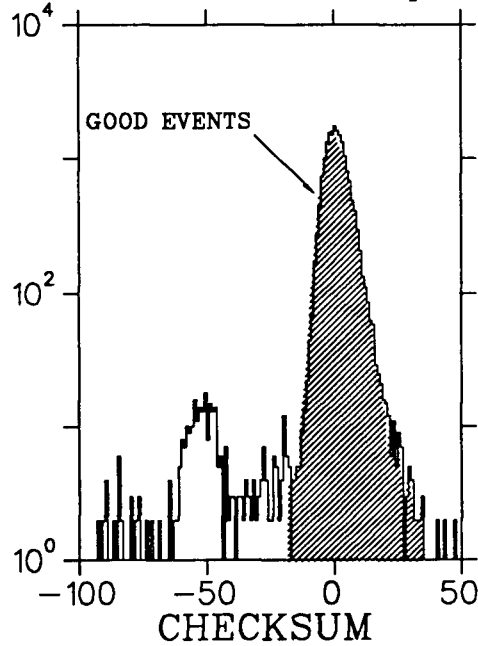


Figure 37: Logarithmic plot of a CHECKSUM distribution enhances features that make it easy to determine the good event cut range.

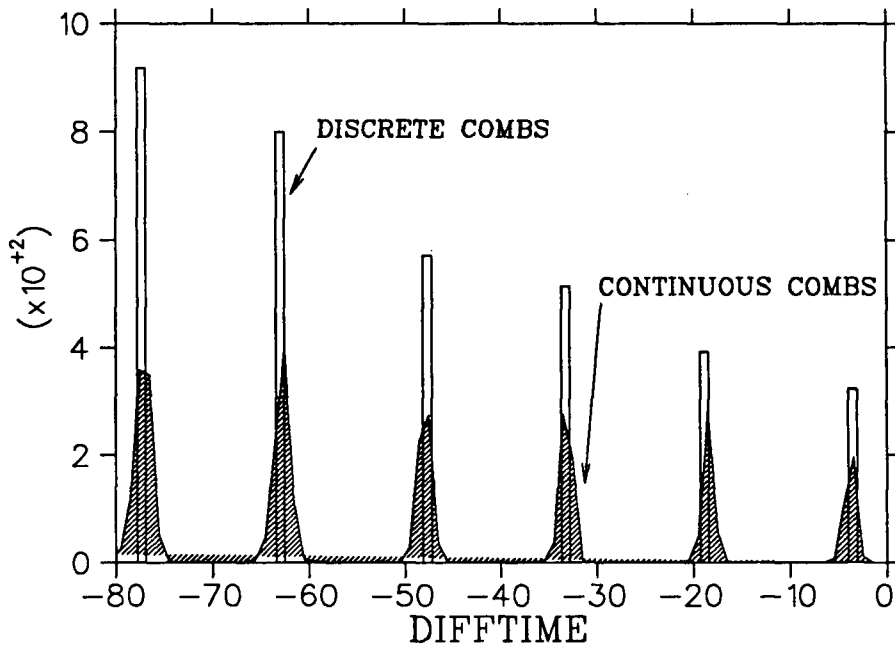


Figure 38: Spectrum shows the discrete COMB spectrum overlapped on the continuous spectrum from which it was derived.

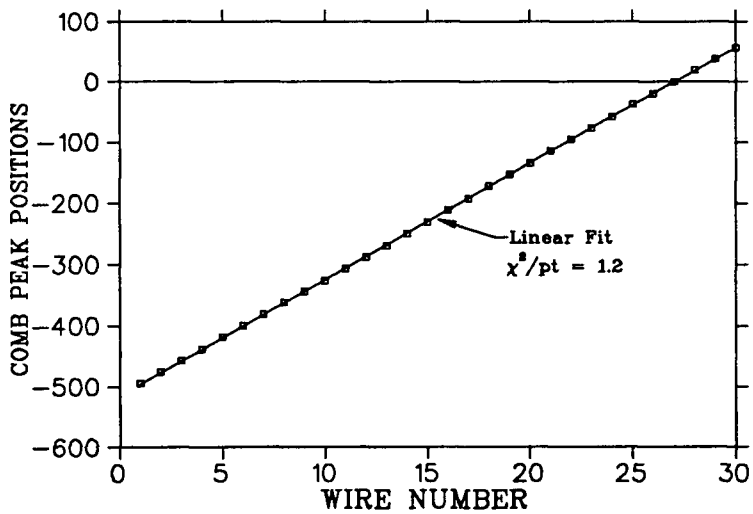


Figure 39: Plot of the COMB peak positions versus DIFFTIME shows the good linearity out to the chamber edge of a large chamber.

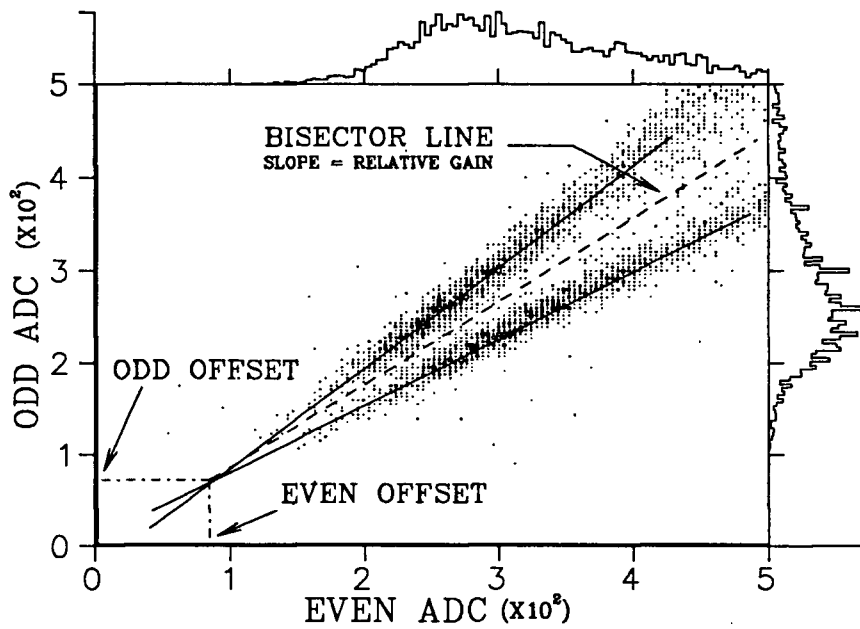


Figure 40: Plot illustrates one method to gain and offset match the ODD and EVEN ADC systems for a wire chamber. Note that one could also determine the sign of the ODD-EVEN difference by noting which side of the bisector line an event registered.

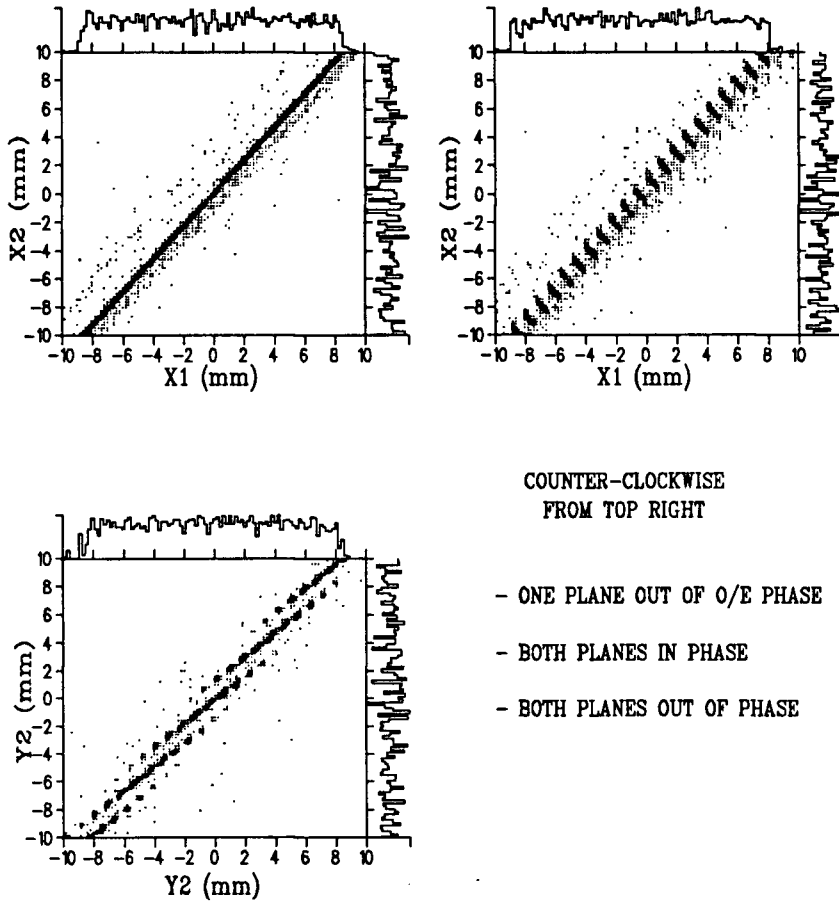


Figure 41: Effect of ODD/EVEN phase on the plots of one chamber coordinate position versus the similar coordinate position in another chamber. By investigating these plots for all chamber combinations, the phase of all polarimeter chambers can be determined.

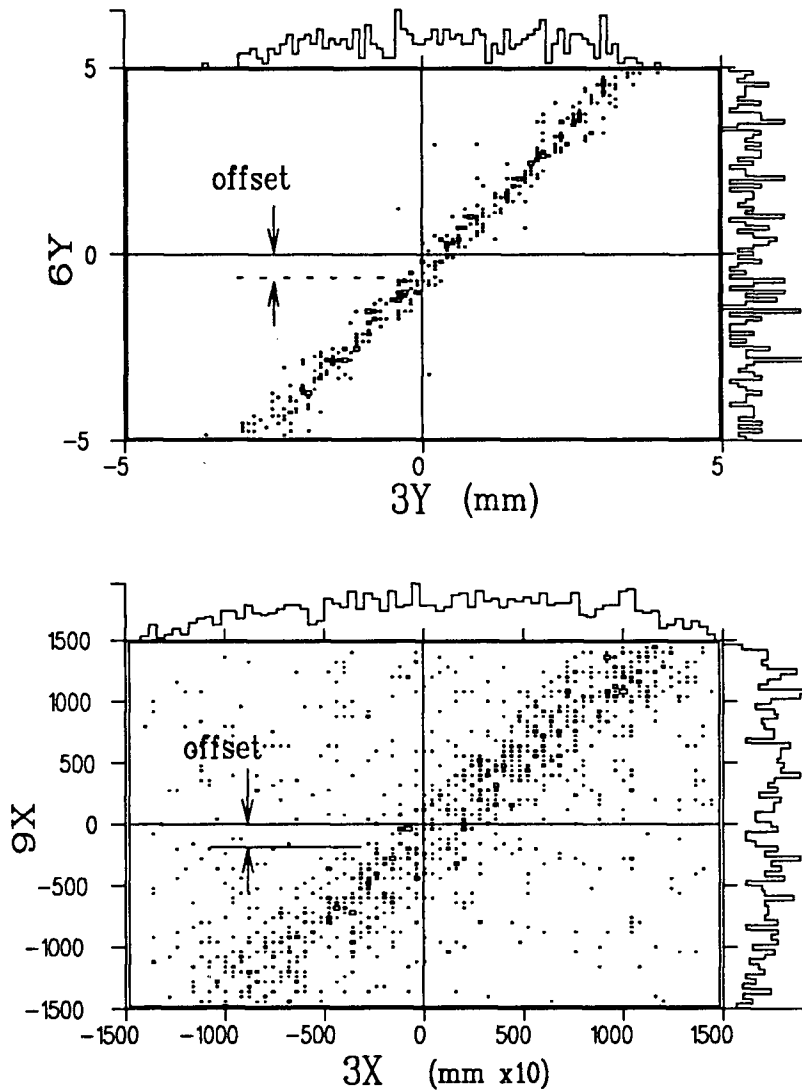


Figure 42: Plots of a polarimeter chamber y-position distribution versus chamber 3y position (left), and a second arm chamber x-coordinate versus chamber 3x position used to align the origins of these chambers with the correlated 2-body proton events from pion absorption on deuterons.

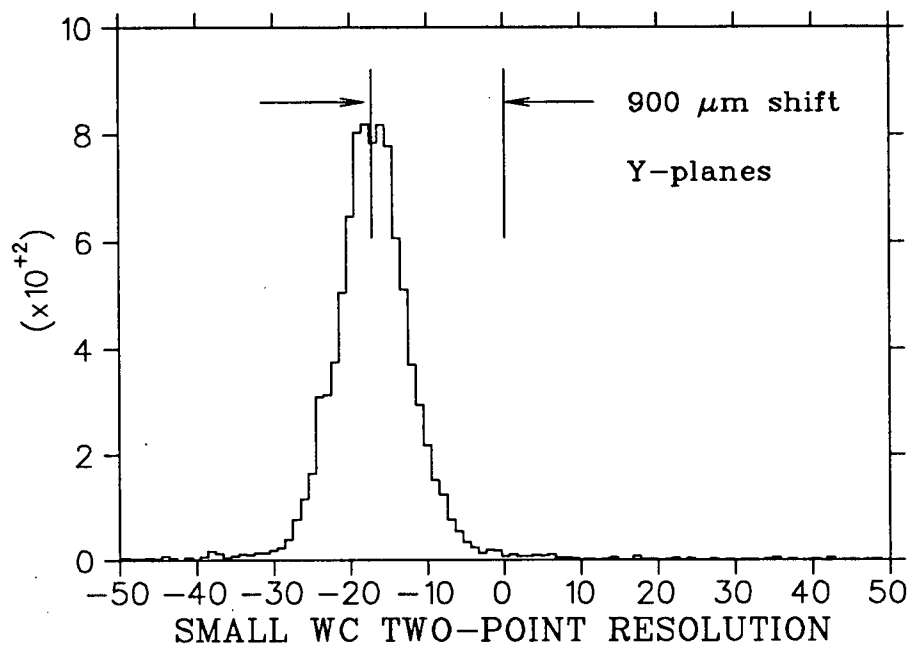


Figure 43: Resolution plot for a misaligned chamber plane group.

Chapter VII

Polarimeter Performance: Results and Conclusions

VII.1 DETECTION EFFICIENCY and RESOLUTION

The efficiency results outlined in the following two sections were obtained during a test run on the TRIUMF M11 pion channel tuned to $390 \frac{\text{MeV}}{c}$, yielding $T_p = 78$ MeV protons for beam rates of 3 to 150 KHz. With the carbon removed, the polarimeter was positioned 190 cm directly at 0° in front of the M11 beam pipe. M11 quadrupole Q4 was defocused to give an elliptical beam spot of about $130 \times 200 \text{ mm}^2$ at the front chamber (1) and about $200 \times 310 \text{ mm}^2$ at the rear chamber (6). This proton test beam has roughly twice the energy-loss as the typically 200 MeV beams detected in experiments 331 and 445, resulting in larger signals and hence larger signal-to-noise ratios, so the conditions under which these tests were carried out can be considered as a 'best case' scenario.

VII.1.1 Chamber Efficiencies

The CHECKSUM distributions are used as a measure of the wire chamber efficiencies (see Section IV.2.4) where 'good event' cuts were placed around the CHECKSUM peaks as shown in figure 37. Efficiencies were investigated as

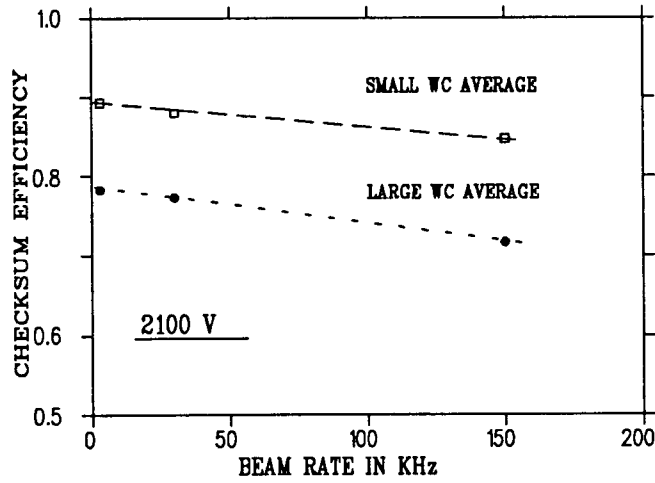
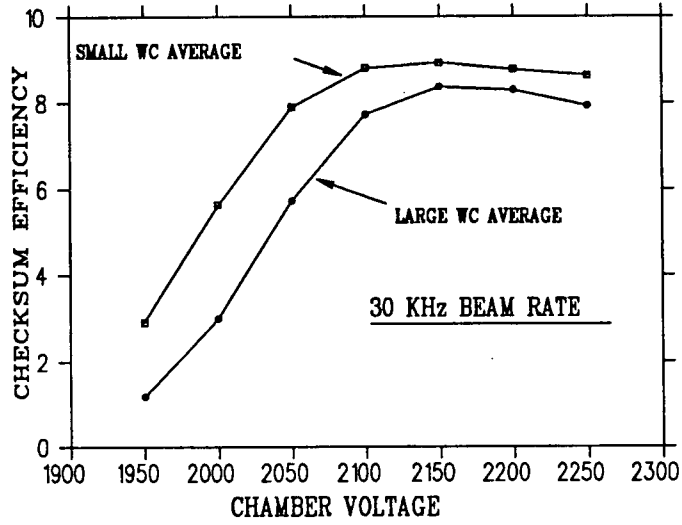


Figure 44: Plots show the dependence of the CHECKSUM efficiency on (top): chamber high voltage for a fixed 30 KHz beam rate, and (bottom): beam rate at a fixed 2100 volts.

functions of chamber high voltage and beam flux. Figure 44 illustrates the results for both the large and small chambers.

Figure 44 (top) shows that, for a 30 KHz beam rate, the CHECKSUM efficiency for detecting a single ‘good’ event reaches a plateau of $\sim 90\%$ at around 2100 volts for both the large and small chambers. The large chambers generally have slightly lower efficiencies since the longer delay-lines increase chamber deadtime and increase the probability of multiple-hit events. Higher voltages are required to counteract space-charge effects in order to maintain efficiencies as incident fluxes increase, as can be seen in figure 44 (bottom) (see Section IV.1.5). Extrapolating linearly to higher rates, it appears that the chambers will reach a kind of practical limit of about 50% efficiency around 1 MHz, a limit expected for delay-line drift chambers as quoted by Atencio [27].

Events that do not pass the CHECKSUM cuts are mainly due to accidental and multiple events, and not due to inefficient LEFT/RIGHT or ODD timing. For voltages in the plateau region, $>97\%$ of events were observed to lie within the SUMTIME and ODDTIME distributions for both the large and small chambers. From this we can conclude that our *triggering* efficiencies for the anode and cathode timing systems are very good.

Since the above tests were run under a relatively *clean* experimental environment, one might question their validity when applied to a ‘real’ runtime situation. In Experiment 331, checksum efficiencies were typically only 10 to 15% lower than these test results over a wide variety of experimental conditions and where single chamber rates were observed to be as high as 250 KHz. Thus our delay-line chambers behave admirably even under the comparatively ‘noisy’ experimental conditions in a pion channel area.

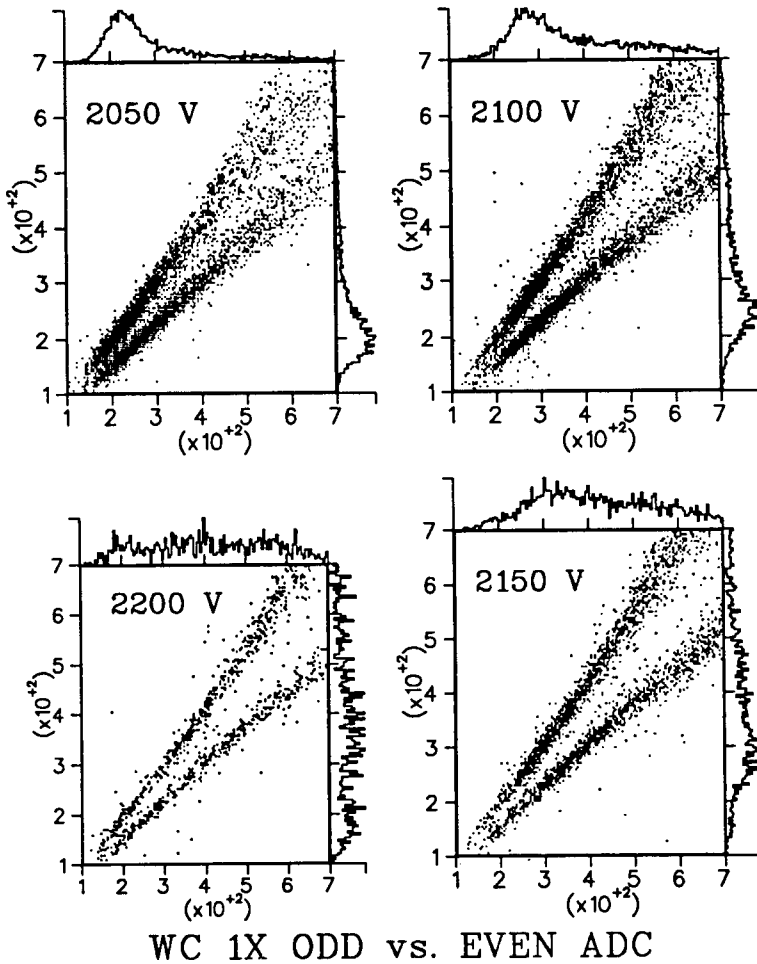
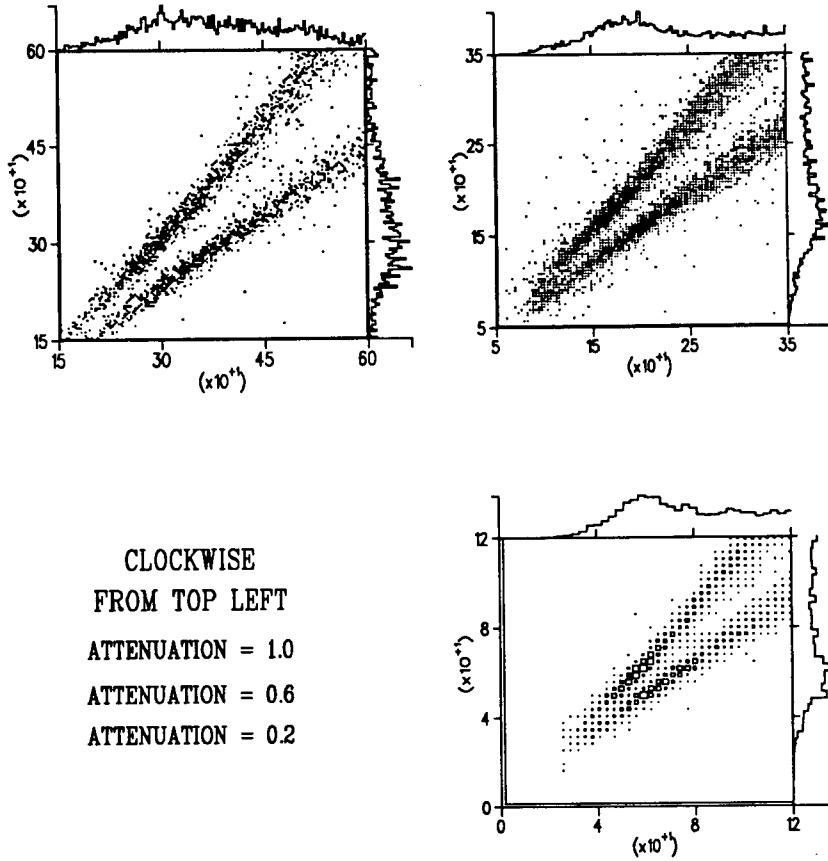


Figure 45: The effect of chamber high voltage on the left/right discrimination. These plots are for a small chamber using an 10-bit 2249A ADC with no attenuation applied to the cathode signals.



WC X1 ODD vs. EVEN ADC

Figure 46: The three scatterplots show the effects of attenuator gain settings of 1.0, 0.6, and 0.2 on a chamber at 2150 volts using a 2249A ADC.

VII.1.2 ODD-EVEN Resolution

The ODD-EVEN resolutions and efficiencies were evaluated under the same test conditions as described above. Chambers were tested employing either the 10-bit LeCroy 2249A or the 11-bit 2249W ADC units for voltages varying from 2000 to 2200 volts. The cathode signals were not attenuated in the voltage tests. Instead, signal attenuation effects were investigated for settings of 1.0, 0.6, and 0.2, at a constant 2150 volts for the 2249A ADCs.

Figure 45 shows that the results of the ODD-EVEN resolution (or left/right discrimination) as a function of voltage from 2050 volts up to 2200 volts for a small chamber utilizing the 2249A ADC. Contrary to what was expected, the resolutions continue to improve up to 2200 volts. Unfortunately, the 2249A cannot accommodate the dynamic range of cathode pulse sizes at the large voltages, as is illustrated in figure 47. Attenuation can be applied to the cathode signals to reduce the amount of ADC overflow, but the resulting lower signal-to-quantization noise ratio decreases the ODD/EVEN separation for pulses in the peak at low values (see figure 46). The plots in figures 46 and 47 clearly demonstrate the reasons for our choice of the LeCroy 2249W for the common gate cathode ADC system. Higher signal-to-quantization noise ratios result in better left/right discrimination regardless whether the 2249A or 2249W ADC is used. However, the dynamic range of the analog cathode signals do not saturate the 11-bit 2249W to anywhere near the extent of the 10-bit 2249A, resulting in much better efficiency. Significant ADC saturation can translate into either poor detection efficiencies if these events are discarded altogether, or reduced tracking resolutions if these events are kept but only the anode wire position information is utilized. Clearly, the 2249W unit avoids both of these compromises.

A new gas gain mode begins above 2150 volts, causing a second broad peak

to appear in the ADC spectra (see figure 47). However, this new mode is also a function of energy-loss. Thus the double-peaking is suppressed under normal operating conditions at 2150 volts using ~ 200 MeV protons. Nonetheless, it appears that chamber voltages cannot be raised much above 2150 volts without overflows appearing even for the 2249W ADCs. Attenuating the cathode signals at higher voltages will cause the ODD-EVEN separation to suffer at small ADC values, thus negating any benefit in raising the voltage in the first place. Therefore it appears that 2150 volts is the best voltage with which to operate the chambers using the 2249W ADC.

VII.1.3 Trajectory Resolution

The **intrinsic position resolution** of a chamber can be found by the procedure outlined in Section VI.3 for aligning the chamber coordinates using the ‘resolution plots’. These distributions show the difference between the position recorded by a middle chamber and the value calculated for that middle chamber using the recorded positions at the adjacent chambers as trajectory endpoints. The width of this distribution arises from the positional uncertainties in *all three* chambers. *i.e.* if

$$\Delta x = x_{mid} + \frac{1}{2}(x_{back} - x_{front}) \quad (47)$$

and assuming that each chamber has a similar gaussian positional resolution profile with error σ ,

$$\sigma_{\Delta x}^2 = \sigma^2 \cdot \left(\left(\frac{\partial dx}{\partial x_{fr}} \right)^2 + \left(\frac{\partial dx}{\partial x_{mid}} \right)^2 + \left(\frac{\partial dx}{\partial x_{bck}} \right)^2 \right) \quad (48)$$

then the variance of the **two-point** resolution plot is $\frac{3}{2}$ that of each chamber.

Figure 48 shows a typical two-point resolution plot calculated for a small chamber group running at 2150 volts and detecting approximately 155 MeV protons during an Experiment 331 run. The solid curve is a gaussian fit to the

histogram having a $\sigma = 300 \mu\text{m}$ standard deviation. This implies single-chamber resolutions of $\pm 240 \mu\text{m}$. Similar plots have been generated for a variety of conditions (voltage, proton energy, beam rate) and the resulting chamber resolutions were found to be quite consistent, with an observed low of $\pm 140 \mu\text{m}$ and high of $\pm 250 \mu\text{m}$. Using $\sigma = \pm 200 \mu\text{m}$ as an estimate of the average chamber resolution, this implies that adjacent wire planes provide

$$\pm \tan^{-1}\left(\frac{\sqrt{2} \cdot 200 \cdot 10^{-3}}{210}\right) = \pm 0.08^\circ \text{ angular resolution.}$$

Effective single-chamber resolutions can be improved if one *fits* a best line to the three positions in a chamber group, lowering the angular limit that each chamber group can resolve. However, the angular resolution using only two chambers is already better than is required for the usual experiments involving a polarimeter of this type. The improvement in spatial and angular resolution when employing best fit trajectories comes at a considerable cost in reduced tracking efficiency. This is due to the fact that all three chambers in a group must fire to allow a fit, instead of only 2/3 for the two-point trajectory definition method. *e.g.* considering an 80% CHECKSUM efficiency for each chamber, a fitted trajectory can be defined in a three chamber group for only $\sim 51\%$ of the incident events, but a two-point trajectory can be defined $\sim 90\%$ of the time. The overall polarimeter efficiency drops even lower when insisting on good trajectories in both the front *and* back systems of chambers.

VII.1.4 J11 Small-Angle Rejection Efficiency

As was mentioned in Section III.1.2, one expects a properly operating small-angle rejection system to filter out over 90% of the proton-carbon scattering events. However, it was observed [10] that the E331 system (as described in Section V.2.3) had a somewhat poorer rejection ratio of $\sim 70\%$. This is a result of the fact that the J11 program accepts events characterized by CHECKSUM inefficiencies in any

of the chambers 1,3,4, and 6, since the other chambers could still be used offline for tracking. If one of these chambers was particularly inefficient for some reason, a large number of small-angle coulomb-scattered events will find their way through the preprocessing filter, thereby reducing the useful event fraction written to tape. The J11 program should be modified in future runs to allow for different chamber combinations to be used in pre- and post-carbon ray tracing in case of chamber inefficiencies. Additional computation time should be negligible compared to the typical computer readout dead-time. Simple Boolean masking of TDC signals to check for time-out values are all that is required to direct the program to the subroutine which does the scattering-angle calculations using the appropriate efficient chambers.

VII.2 ARTIFICIAL ASYMMETRY RESULTS

Parasitic asymmetries were studied for a particular Experiment 331 test run using an unpolarized deuterated-butanol target. The magnetic holding field was turned off to remove the complication of spin precession for protons exiting the target (see Feltham [10]). The proton beam energies (from the $\pi + d \rightarrow p + p$ reaction) incident on the polarimeter varied from 230 to 240 MeV across the 7cm carbon analyzer. (The central beam trajectory energy of 235 MeV is used for this analysis). Background protons from the quasi-free absorption on other nuclei in the target were discriminated against by placing cuts on the 2-body kinematical correlations (opening angle and coplanarity). A $\sim 10\%$ background contribution remains, but will be neglected for the purposes of this test. The kinematical correlations and other cuts (carbon traceback, etc.) were implemented as described by Feltham [10].

The proton beams detected by the polarimeter are 100% polarized *normal* to

the scattering plane since the normal polarization component is the only one allowed by parity invariance for protons produced by pion absorption on an unpolarized deuteron target. Therefore, measurement of any transverse polarization component in the carbon scattering implies the existence of systematic errors causing such parasitic asymmetries.

The proton polarizations for this analysis were extracted by both the Fourier χ^2 fitting technique requiring 2π acceptance symmetry (described in Section III.2.2), and the Bessel weighted-sums technique [19] requiring $\phi + \pi$ acceptance symmetry, as implemented by Feltham [10]. Results from the fitting method are used as a check of the weighted sums technique, which has been adopted for use in Experiment 331 [10]. Sideways scattering asymmetries were also extracted by the fitting technique to demonstrate its use in determining the efficiency acceptance function $D(\theta, \phi)$ (see Section III.2.2).

For the Fourier fits, the observed angular distributions were binned into 10^θ bins for $\theta \in [7, 19]$ degrees and 10^ϕ bins for $\phi \in (-180, 180]$ degrees. The lower angular limit corresponds to a value safely beyond the proton multiple scattering cone in the carbon, while the upper limit corresponds to the largest angle for which p-C inclusive analyzing powers are quoted in the literature [1,2]. The polarization results from both techniques were determined using the 213 MeV inclusive analyzing powers from the McNaughton parameterization [1], corresponding to the kinetic energy of the ‘average’ (235 MeV) beam at the center of the 7 cm carbon analyzer. At this level no corrections were made for different energy losses or for the different incident energies across the analyzer. This is a reasonable approximation since the angle-averaged analyzing power changes little in this energy region (see figure 9 on page 29).

Figure 49 illustrates the sideways asymmetry and polarization results determined using the the Fourier fitting technique, while the sideways polarization

result using the weighted-sums method appears in figure 50. (The Fourier fitted results are shown only up to $\theta = 17^\circ$ since there was not enough statistics in the last two angular bins to allow reliable fits). There is reasonable agreement between the average polarizations calculated by the two techniques, $P_s^{FF} = 0.11 \pm .03$ and $P_s^{WS} = 0.08 \pm .03$, which represent the weighted average of the polarizations extracted for each θ bin, $P_s(\theta_{carbon})$. The resulting angular distributions correspond well in the overall shape, showing reasonable agreement at each point. From these results, one can see any parasitic (systematic) asymmetries are small for the up/down scattering over most of the scattering region ¹.

Any statistically significant ‘bumps’ in the sideways asymmetry distributions may qualify as correction terms for any subsequent sideways polarization analyses. This is due to the fact that these deviations are associated with the first order terms $\frac{b_1(\theta)}{a_0}$ in the detection efficiency function $D(\theta, \phi)$, which can be identified as parasitic errors (refer to Section III.2). Referring to the Fourier fitted result in figure 49, the sideways asymmetry value at 12° , and also possibly the results at 15° and 17° , may be evidence for the need of such corrections. Of course, one would want to ensure that these bumps persist over many more runs before qualifying them as ‘real’ parasitic asymmetries.

VII.2.1 Asymmetry Corrections from Angular Displacements

One can check to see if the slight deviation from zero in the calculated average sideways polarizations are a result of angular displacements arising from wire chamber misalignments. The angular displacements are found using equations 14 and 17 outlined in Section III.2.3. Note that the required logarithmic derivative

¹In these runs, the normal to the pion-deuteron reaction plane was limited to about $\pm 10^\circ$ with respect to the lab normal, so left/right and up/down scattering in the carbon also corresponded to the left/right and up/down regions of the rear chambers.

of the observed cross-section simply represents the *fractional change* in the distribution

$$\frac{d}{d\theta}(\log I_0(\theta)) \equiv \frac{\frac{dI_0(\theta)}{d\theta}}{I_0(\theta)} \quad (49)$$

and therefore the absolute normalization of the cross-section does not need to be known. These unnormalized cross-sections are determined by the constant terms in the Fourier series expansion in ϕ of each θ bin, so the results presented here can only be applied to the asymmetries extracted with the Fourier fits. Here the errors in the projected scattering angles, $\Delta\theta_x$ and $\Delta\theta_y$ are calculated using coulomb-scattered events ('straight throughs') for which $\theta \leq 3^\circ$. The resulting distributions for the logarithmic derivative of the observed cross-section and the projected coulomb-scattering angles are shown in figure 51.

The angular displacements seen in figure 51, $\Delta\theta_x = 0.002$ and $\Delta\theta_y = 0.007$ (in radians), are small and contribute negligibly to the observed scattering asymmetries in the nuclear scattering region. The logarithmic derivative of the observed distribution ($\frac{dI(\theta)}{I}$) is no greater than 0.5 in magnitude, corresponding to a maximum correction to the normal asymmetry of $\Delta\epsilon_N < (.007) \cdot (-.5) = -0.0035$, which is completely negligible compared to the current statistical errors. The small corrections are no doubt due to the the careful chamber alignment made possible by the fine resolution in our chambers.

VII.3 SCATTERING EFFICIENCY and FIGURE-OF-MERIT for 200 MeV PROTONS

Presented here are the polarimeter scattering efficiency and figure-of-merit parameters for ~ 235 MeV protons scattered from a 7cm carbon analyzer. The values of these parameters depend on the form of the carbon scattering acceptance

employed; consequently, they will be calculated separately for each of the full, 2π , and ' $\phi + \pi$ ' acceptance conditions. Refer to Sections III.3 and III.2.2 for definitions and relevant equations.

These investigations use data from the same runs analyzed in the prior artificial asymmetry, except that *all* incident protons were accepted, including those from the quasi-free absorption in addition to the two-body correlated events from pion absorption on deuterons. The figures-of-merit \mathcal{F} quoted refer to $T_p^{center} = 210$ Mev, corresponding to the 'average' kinetic energy of the incident proton beam at the *center* of the carbon². (Recall that the incident proton beam energy varied from 230 to 240 MeV across the carbon analyzer in these runs). These results will be insensitive to the spread of energies about the 'average' since the angle-averaged analyzing power peaks broadly here (see figure 9 on page 29), and the inclusive cross-section can be reasonably assumed to change little over this energy range. Events corresponding to scattering into the angular range $\theta \in [7, 19]$ degrees which pass the good event tests, including the appropriate acceptance test, qualify as 'useful' scattering data. Unlike the POMME analysis [15], no corrections were made for chamber efficiencies; consequently these figure-of-merit results are strictly applicable only for use with our system. The angular distributions of the differential and integral figure-of-merit results are illustrated in figures 52 for the full, 2π , and ' $\phi + \pi$ ' acceptance provisions, respectively. Similarly, the differential and integral scattering efficiencies are presented in figure 53. The corresponding global scattering efficiency and figure-of-merit results are summarized in table II.

The polarization statistical error predictions listed in table II are calculated using the global figures-of-merit listed in the table and equation 22 in Section III.3, for $N_{inc} \sim 1.25 \cdot 10^6$ incident protons. These predictions are appropriate to the

²Recall from Section III.2.1 that inclusive p-C analyzing powers have been calculated and tabulated in terms of proton kinetic energies at the center of the carbon.

| ACCEPTANCE | α | \mathcal{F} | ΔP |
|--------------|----------|---------------|------------|
| full | 1.1% | 0.059 | 0.021 |
| $\phi + \pi$ | 0.74% | 0.049 | 0.026 |
| 2π | 0.43% | 0.038 | 0.033 |

Table II: Global scattering efficiency and figure-of-merit results for 235 MeV protons incident on a 7 cm carbon analyzer for each of the polarimeter acceptances. These values have an estimated $\sim 10\%$ uncertainty. The statistical error estimates are calculated for $1.25 \cdot 10^6$ incident protons, corresponding to the number in the data set used in the sideways polarization analyses of Section VII.2.

sideways polarization results from the previous section, where those results were obtained from approximately those many $\pi + d \rightarrow p + p$ incident proton events. The predicted errors show good agreement with the actual errors quoted with the 2π and $\phi + \pi$ sideways polarizations illustrated in figures 49 and 50.

A few interesting points arise upon closer inspection of the figure-of merit angular distributions $\mathcal{F}^2(\theta)$ shown in figure 52 (bottom), and the statistical error predictions in table II. One can see that the largest scattering angles contribute relatively little to the figure-of-merit integrals in the $\phi + \pi$ and 2π acceptance cases. This implies that these events can be safely ignored without seriously compromising polarization errors *e.g.* if significant parasitic asymmetries are found at these extreme angles. Also, even though the global scattering efficiency for full acceptance is $\sim 50\%$ larger than for the $\phi + \pi$ acceptance symmetry, there is only a corresponding 19% decrease in polarization statistical error. The difference is even greater going from the 2π acceptance to the $\phi + \pi$ acceptance symmetry: a 72% increase in global efficiency results in only a 21% decrease in statistical error. This is due to the fact that there is relatively little contribution to the figure-of-merit at large angles since the figure-of-merit involves the *square* of the analyzing power, and at large angles both the analyzing power and the scattering efficiency are small in the energy range considered here. The differential figure-of-merit distributions illustrate this effect in figure 52 (top).

VII.4 CONCLUSIONS and RECOMMENDATIONS

Our multi-wire delay-line drift chambers have proven to be very satisfactory for tracking particles in the polarimeter developed for use in the meson hall at TRIUMF. The inherent rate limitation of large delay-line chambers is not a problem under typical experimental conditions in that environment. Good spatial resolutions of $\sim \pm 200\mu\text{m}$ provide adequate angular resolution to enable the chambers to be closely spaced for good solid angle coverage. The inclusion of a redundant third chamber in each tracking group is considered a significant reason for the success of the system. The almost two-fold improvement in detection efficiency of the polarimeter, (from $\sim 50\%$ to $\sim 90\%$ for typical 85% chamber efficiency) is very important when operating with the low reaction rates experienced in pion experiments.

Except for the limited dynamic range of the particular ADC employed (LeCroy 2249A), the common-gate ADC system developed to resolve the left/right ambiguity works very satisfactorily under a variety of experimental conditions. However, future use of this system should use employ the LeCroy 2249W extended-range wide-gate ADC instead. The two-fold increase in dynamic range compared to the 2249A unit enables the cathode signals to be digitized without need for attenuation, thus improving signal-to-noise and therefore allowing for the greatest possible ODD-EVEN separation.

The polarization of a ~ 230 MeV protons arising from pion absorption on an unpolarized deuteron was measured, yielding very small sideways polarizations consistent with zero as expected for such a reaction. Normal polarizations are also known for this reaction from the \mathcal{A}_{N0} analyzing power in the time-reversed $p + p \rightarrow d + \pi$ reaction, where time-reversal symmetry stipulates that for the

normal proton polarizations in the absorption reaction, $\mathcal{P}_N = \mathcal{A}_{N0}$. Feltham [10] has reported good agreement between normal polarizations measured and those expected from \mathcal{A}_{N0} for other measurements made with unpolarized deuteron targets. Unfortunately, similar analyses of the runs considered here show large positive normal polarizations several standard deviations above that expected, thereby indicating large systematic errors for these runs affecting only the normal asymmetries. Additional investigations into the possible origins of this problem are continuing.

Proton beams without normal polarization cannot be easily obtained in a pion area, so future experiments employing our polarimeter should consider test runs similar to the runs considered here, but with all the polarimeter chambers rotated 90° in their mounts. This procedure should decouple the wire chamber and scintillator contributions to any observed systematic asymmetries, enabling one to treat both the normal and the sideways components separately.

No figure-of-merit results have been published so far in the proton kinetic energy region analyzed here, although the $\sim 1.0\%$ global scattering efficiency results for ~ 200 MeV protons incident on a 7cm carbon target are consistent with a value given by Hausser [39] in a TRIUMF MRS FPP design note. The figure-of-merit results given here have been proven to be valuable parameters for reliably predicting the statistical error in measured proton polarizations for given numbers of protons incident on the polarimeter. In this regard, these results have also shown that, at this energy, the Besset weighted-sums polarization extraction technique [19] employing $\phi + \pi$ carbon scattering acceptance symmetry provides comparable performance to the brute-force Fourier fitting technique using the full polarimeter acceptance. For the runs analyzed here, the weighted-sums method can provides polarizations with only 19% more statistical error than could be obtained using the brute-force fitting method, but without the need to explicitly

determine the polarimeter acceptance function $D(\theta, \phi)$ as required by the latter technique. In addition, the considerable savings in computational effort afforded by the weighted-sums technique in replacing χ^2 minimization with simple matrix operations suggests this as the preferred method for calculating polarizations with our system.

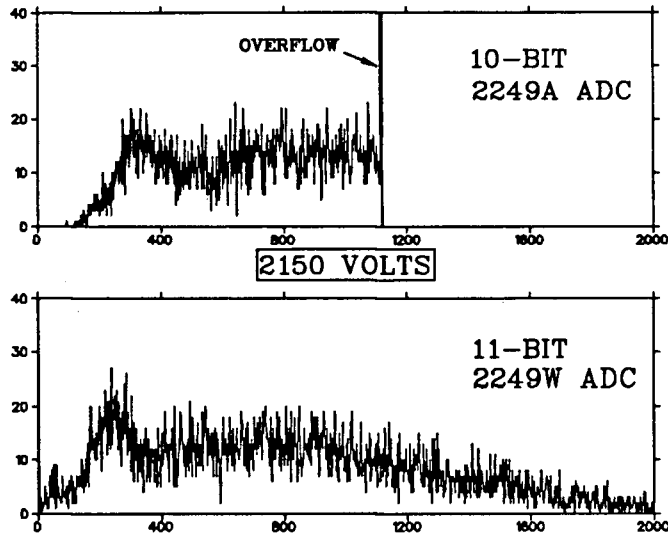


Figure 47: Extent of ADC overflow for two large chambers at 2150 volts using the 2249A and 2249W ADCs with no attenuation. Note that the left/right discrimination using the 2249A unit is the same as the 2249W for events that do not overflow.

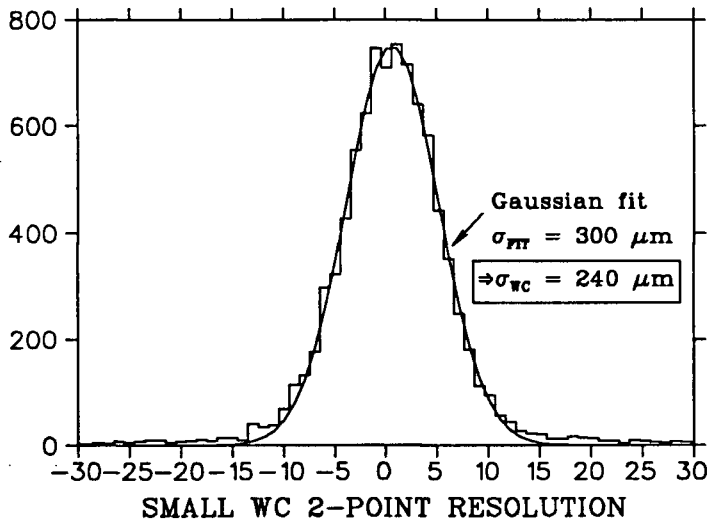


Figure 48: Two-point resolution plot for the polarimeter small chamber group. The curve represents the best-fit of a Gaussian lineshape to the distribution, implying single-chamber spatial resolutions of $240 \mu\text{m}$.

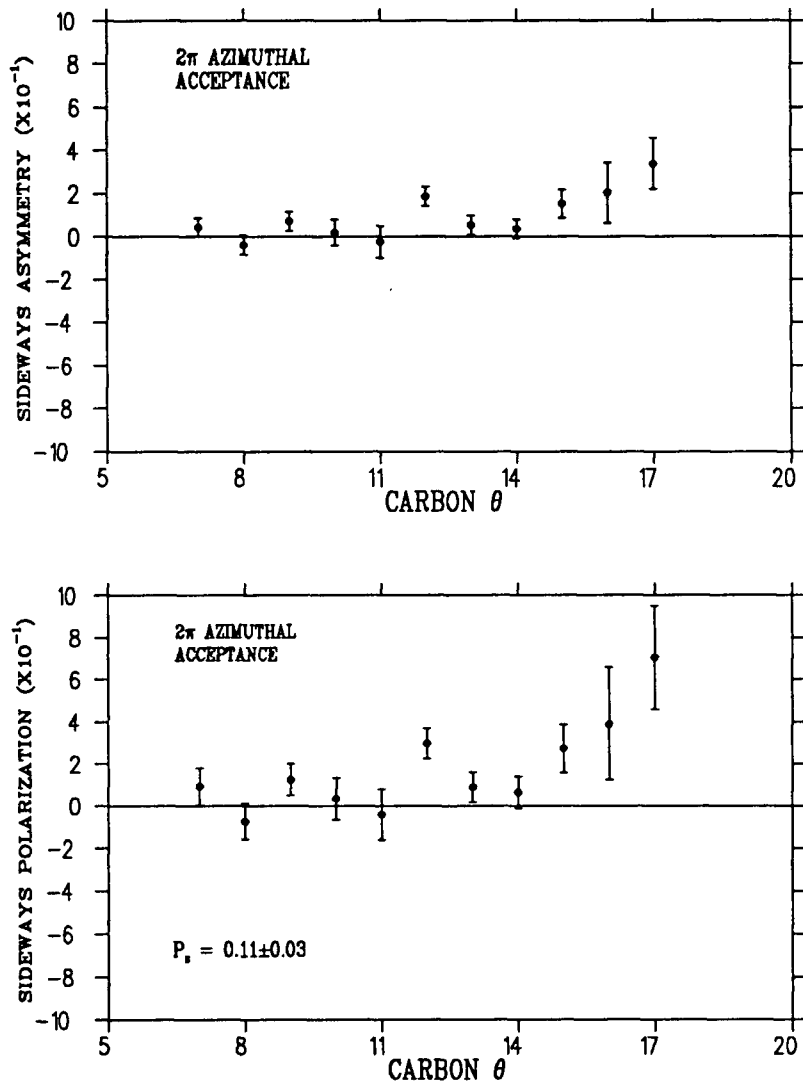


Figure 49: Sideways asymmetries and polarization as a function of carbon scattering angle for a run with no sideways proton polarization. The asymmetries were extracted with the Fourier fitting technique.

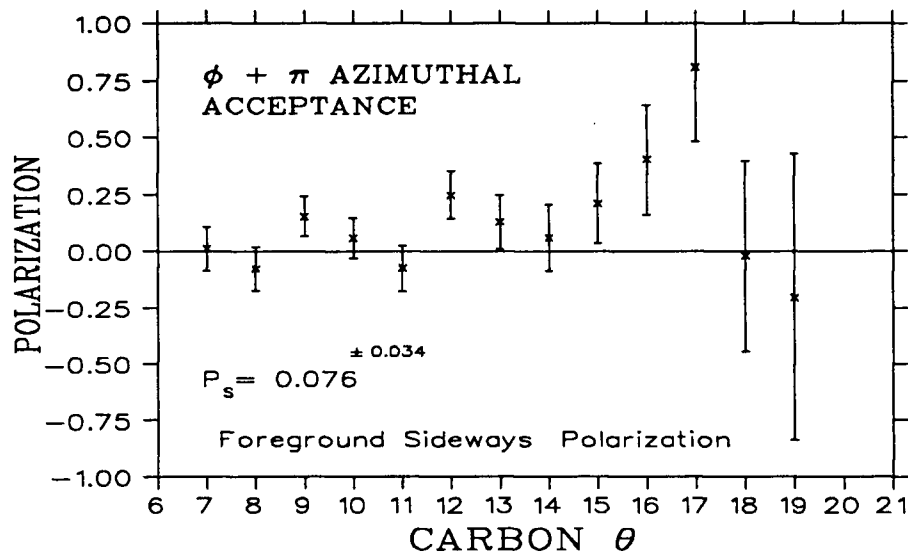


Figure 50: Sideways polarization as a function of carbon scattering angle for a run with no sideways proton polarization. This data was analyzed by the weighted-sums asymmetry extraction technique.

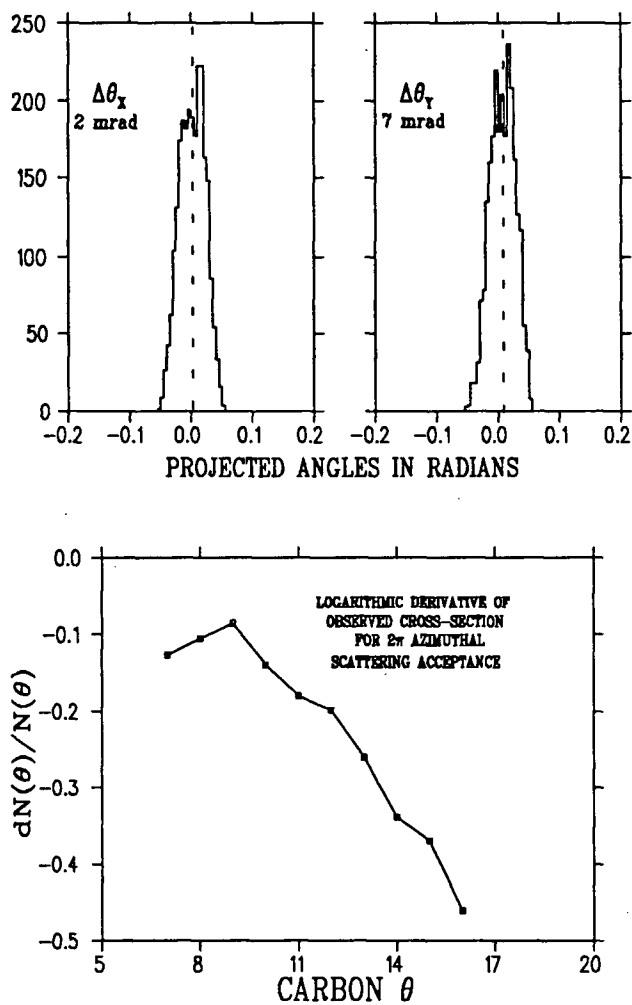


Figure 51: Diagrams showing the distributions in the projected angles (top) and the logarithmic derivative of the observed angular distribution for 2π acceptance symmetry. Note that the small angular displacements imply corrections to the polarizations an order of magnitude smaller than the measured sideways polarizations shown in figure 49.

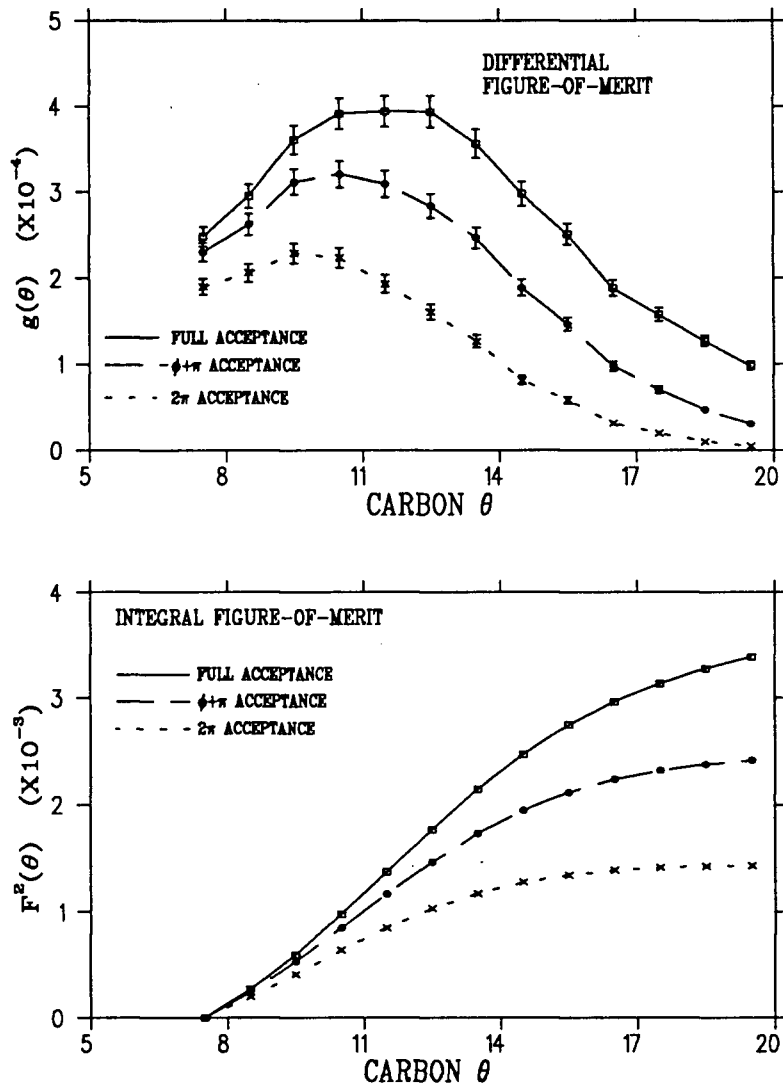


Figure 52: Differential and integral figure-of-merit angular distributions corresponding to 235 MeV protons incident on a 7 cm carbon analyzer, for full, $\phi + \pi$, and 2π polarimeter scattering acceptances.

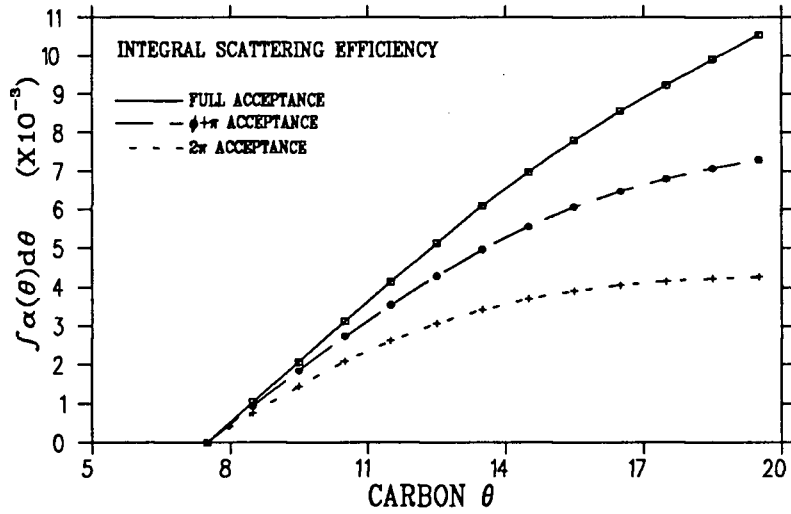
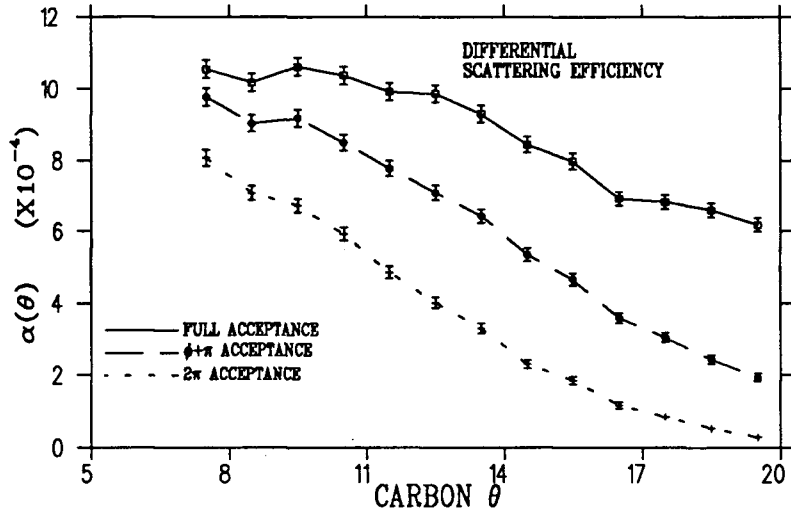


Figure 53: Differential and integral scattering efficiency angular distributions corresponding to 235 MeV protons incident on a 7 cm carbon analyzer, for full, $\phi + \pi$, and 2π polarimeter scattering acceptances.

Bibliography

- [1] M.W. McNaughton, et al., *Nucl. Instr. Meth.* **A241**:435, 1985.
- [2] E. Aprile-Giboni, et al., *Nucl. Instr. Meth.* **215**:147, 1983.
- [3] R.D. Ransome, et al., *Nucl. Instr. Meth.* **201**:309 1982.
- [4] O. Häusser, et al., *Nucl. Instr. Meth.* **A254**:67, 1987.
- [5] D. Besset, et al., *Nucl. Instr. Meth.* **166**:379, 1979.
- [6] G. Waters, et al., *Nucl. Instr. Meth.* **153**:401, 1978.
- [7] G. Jones, Private Communication.
- [8] G.D. Wait and D.C. Healey *Summary of Deuteron target Polarization Analysis for Experiment 331* TRIUMF Technical Report, 1987, unpublished.
- [9] G. Jones (spokesperson) *Spin Transfer in the $\pi\vec{d} \rightarrow \vec{p}p$ Reaction*. TRIUMF Proposal 331, 1985.
- [10] A. Feltham, *A Polarimeter for Spin Transfer Measurements of the $\pi d \rightarrow pp$ Reaction*. M.Sc. Thesis, University of British Columbia, 1988. unpublished.
- [11] M. Moinester and P. Trelle (spokespersons) *Polarization in Pion Absorption on ^3He* . TRIUMF Proposal 445, 1986.
- [12] *Polarization Phenomena in Nuclear Physics*, 3rd International Symposium, Univ. Wisconsin, Madison, 1970.

- [13] R.G. Sachs, *'The Physics of Time Reversal'*, University of Chicago Press, Chicago, London, 1987.
- [14] R. D. Ransome *Measurement of the Free Neutron-Proton Analyzing Power and Spin Transfer Parameters in the Charge Exchange Region at 790 MeV*. Ph.D. Thesis, University of Texas, 1981, unpublished.
- [15] B. Bonin, et al., *Nucl. Instr. Meth.* **A288**:379, 1990.
- [16] HRS Polarimeter, Los Alamos preprint, 1983.
- [17] D. Besset, et al., *Nucl. Instr. Meth.* **184**:365, 1981.
- [18] D. Aebischer, et al., *Nucl. Instr. Meth.* **124**:49, 1975.
- [19] D. Besset, et al., *Nucl. Instr. Meth.* **166**:515, 1979.
- [20] R.D. Ransome, et al., *Nucl. Instr. Meth.* **201**:315, 1982.
- [21] A.H. Walenta, *Nucl. Instr. Meth.* **151**:461, 1978.
- [22] F. Sauli, *Principles of Operation of Multi-Wire Proportional and Drift Chambers*, CERN REPORT, 77-09, May 1977.
- [23] A. Breskin, et al., *Nucl. Instr. Meth.* **119**:9, 1974.
- [24] R.S. Henderson, et al., *Nucl. Instr. Meth.* **A254**:61, 1987.
- [25] A.H. Walenta, *Nucl. Instr. Meth.* **217**:65, 1983.
- [26] W.R. Leo, *'Techniques in Nuclear and Particle Physics'*, Springer Verlag, Berlin Heidelberg, 1987, chapter 6.
- [27] L.G. Atencio, *Nucl. Instr. Meth.* **187**:381, 1981.
- [28] R. Oppenshaw, Private Communication, 1987.

- [29] C.L. Morris, H.A. Theissen, G.W. Hoffman *IEEE Trans. Nucl. Sci.* NS-25 (1) (1978) 141.
- [30] TRIUMF Users' Handbook, 1987.
- [31] A. Feltham, Private Communication, 1989.
- [32] D. Ashery, Private Communication, 1989.
- [33] W. Faszer, Private Communication, 1988.
- [34] R. Henderson, Private Communication, 1988.
- [35] Both amplifiers are based on designs of J. Cresswell of TRIUMF; however the anode and (to a lesser extent) the cathode preamplifiers were modified by Doug Maas of U.B.C.
- [36] The fits were done using the TRIUMF PLOTDATA plotting and analysis package written by Joseph Chuma and Cory Kost.
- [37] D. Ashery, Private Communication, 1989.
- [38] An elegant program which determines the peak positions of an arbitrary COMB spectrum and determines the best fit parameters has been developed for our group by summer student Rob Deary.
- [39] O. Häusser, TRIUMF Design Note, 1981.

The anode preamplifiers used with our multi-wire delay-line drift chambers employ Plessey SL560C wideband preamplifier chips in a two-stage feedback configuration. This design provides relatively low noise ($< 5 mV_{pp}$ output), moderate gain ($\sim 40X$), and large bandwidth (< 10 nsec risetime) necessary for proper anode pulse amplification and timing. The positive high voltage connection to the delay line is incorporated into one of the two anode preamplifiers. $1.0\mu F$ capacitances block this large D.C. offset at the inputs of both amplifiers.

Unlike the MRS chambers [24], where a small $1\mu H$ inductance was introduced at the preamp inputs to realize a low-pass filter, extensive tests showed that no form of risetime compensation was required in our circuit in order to provide good CFD triggering. In fact, the preamplifiers tended to oscillate whenever any inductance at all was connected at the 90Ω preamp input. Anode pulses of ~ 15 nsec risetime were observed at the preamp outputs on 'average' from chamber pulses at the input.